12-20-2006

Reconstructing Spectral Scenes using Statistical Estimation to Enhance Space Situational Awareness

Travis F. Blake

Reconstructing Spectral Scenes Using Statistical Estimation to Enhance Space Situational Awareness

DISSERTATION

Travis F. Blake, Major, USAF

AFIT/DS/ENG/06-05

DEPARTMENT OF THE AIR FORCE
AIR UNIVERSITY

AIR FORCE INSTITUTE OF TECHNOLOGY

Wright-Patterson Air Force Base, Ohio

The views expressed in this dissertation are those of the author and do not reflect the official policy or position of the United States Air Force, Department of Defense, or the United States Government.

AFIT/DS/ENG/06-05

Reconstructing Spectral Scenes Using Statistical Estimation to Enhance Space Situational Awareness

DISSERTATION

Presented to the Faculty

Graduate School of Engineering and Management

Air Force Institute of Technology

Air University

Air Education and Training Command

In Partial Fulfillment of the Requirements for the

Degree of Doctor of Philosophy

Travis F. Blake, B.CmpE., M.S.E.E.

Major, USAF

December 2006

AFIT/DS/ENG/06-05

Reconstructing Spectral Scenes Using Statistical Estimation to Enhance Space Situational Awareness

Travis F. Blake, B.CmpE., M.S.E.E.
Major, USAF

Approved:

/signed/	1 Sep 2006
Lt Col Matthew E. Goda (Chairman)	Date
/signed/	1 Sep 2006
Dr. Richard F. Deckro (Dean's Representative)	Date
/signed/	1 Sep 2006
Dr. Stephen C. Cain (Member)	Date
/signed/	1 Sep 2006
Dr. Victor L. Gamiz (Member)	Date
/signed/	1 Sep 2006
Dr. Ronald F. Tuttle (Member)	Date

Accepted:

/signed/	1 Sep 2006
M. U. Thomas Dean, Graduate School of Engineering and Management	Date

Abstract

Space is an integral part of not only US military power, but also of US civil and economic interests. As the US reliance on space increases, the protection of the important satellites in space is becoming more critical. This protection can only occur when all of the objects in space, as well as the space environment, are characterized and understood. The information needed to characterize and understand these objects and the space environment fall into a broad category known as Space Situational Awareness (SSA).

Many different sources of information are currently used in SSA, but these alone are not enough to provide all the answers to this complex problem. New methods need to be developed to fill in gaps and provide additional SSA information. One such area is spectral imagery. Spectral images of satellites will provide critical information regarding the satellite's physical characteristics, as well as performance and capabilities assessments, needed for SSA.

A new sensor, the Advanced Electro-Optical System (AEOS) Spectral Imaging Sensor (ASIS) has been developed at the Maui Space Surveillance Complex (MSSC). ASIS is capable of collecting spatially resolved imagery of satellite and other space objects in up to 100's of spectral bands. However, the stringent requirements of collecting ground-based images of satellites required a sensor that induces more spectral blurring than desired. The spectral blurring is due to the large spectral bandwidths needed for the proper signal level for imaging. Post-processing algorithms to remove this blurring are needed to fully exploit these spectral images.

This research focuses on developing the reconstruction algorithms to simultaneously spatially and spectrally deblur the images collected from ASIS. The algorithms are based on proven estimation theories and do not require *a priori* knowledge of the scene. While the algorithms developed in this research are targeted for use with

ASIS, they can be used on data collected with any system using a filtering technology known as Electronic Tunable Filters (ETFs).

Previous methods to deblur spectral images collected with ETFs have meet with some success. However, the reconstruction algorithm developed in this research provides a lower root mean square error for spectrally deblurring then the previously investigated methods. This algorithm expands on a method used for increasing the spectral resolution in gamma-ray spectroscopy. However, in addition to the spectral reconstruction, the reconstruction of the spatial scene is also included. The algorithm is able to reconstruct the spatial scene without any loss of the spectral reconstruction capability.

The research also calculates the Cramér-Rao lower bounds on two key performance parameters of the reconstruction algorithm. The spectral resolution and accuracy lower bounds give the best theoretical performance any algorithm can achieve on ASIS data. Thus the bound provides a quantitative assessment of how well the algorithm is performing. The bounds can also be used to determine the optimal sensor parameters needed to collect a spectral image. Additionally, the bounds can be used to determine a performance metric. This metric can be used to compare the ability of the algorithm to work on different spectral sensors and help select critical image collections parameters.

Acknowledgements

There are many people I need to thank for helping me through this. First and foremost is my family; without their encouragement and help I'm sure I never would have made it this far. I hope that I was able to balance my requirements at school with your needs. I've certainly enjoyed the past years and look forward to the many wonderful times to come.

I'd like to thank my advisor, Lt Col Goda for his tireless aid and encouragement. I really appreciate the all of his effort at the end of this research so I could complete all of the degree requirements early. I also appreciate the advice and consultation of the rest of my committee, especially Dr. Cain. Dr. Cain not only provided the initial thoughts for this research, but was instrumental in providing direction and insight that kept me on track throughout this process.

I'd like to thank the sponsors of this research for their continued support and funding.

A special thanks goes out to the other students who shared in this journey. George, Marcus, the younger and elder, Flash, Calvin, Pete and the others of the BARF and penthouse provided the much needed venting and comic relief every graduate student requires.

I'd also like to thank the AFIT Physics lab technicians Mike and Greg for their aid in setting up and using the equipment in their labs. Without their help, I never would have been able to finish this research.

Finally, I'd need to thank Ken for all of his help and insight in the design and operation of the sensor.

Travis F. Blake

Table of Contents

List of Figures

List of Tables

List of Symbols

Symbol		Page
$i(x, y, \lambda)$	Spectral Image Cube	24
$h_1(u, v, \gamma)$	Spatial Blurring Function	24
$h_2(\lambda, \gamma)$	Spectral Blurring Function	24
$o(u, v, \gamma)$	True spectral scene	24
(u, v)	Spatial Coordinates of the Spectral Scene	24
(γ)	Spectral Coordinate of the Spectral Scene	24
(x, y)	Spatial Coordinates of the Spectra Image Cube	24
(λ)	Spectral Coordinate of the Spectral Image	24
$h(u, v, \gamma)$	Invariant Blurring Function	25
$d(x, y, \lambda)$	Spectral Data Cube	26
$n(x, y, \lambda)$	Noise associated with spectral image collection	26
$D(x, y, \lambda)$	One collection of the Spectral Data Cube	26
$OTF(x, y, \lambda)$	Optical Transfer Function	38
$\oplus$	Autocorrelation	38
$P(x, y, \lambda)$	Pupil Function	38
b_w	Bandwidth	62
$\hat{a}_i(R)$	Estimated value for CRLB	98
A_i	True value for CRLB	98
$F_{i,j}$	Fisher Information matrix	98
I_1	Spectral Resolution CRLB first feature intensity	98
I_2	Spectral Resolution CRLB second feature intensity	98
$\Delta\gamma$	Spectral Resolution CRLB feature distance	98
γ_o	Spectral Accuracy CRLB feature location	106
I_o	Spectral Accuracy CRLB feature intensity	106
$h_3(\pi, \phi)$	Linear Polarimetric Blurring Function	120

Symbol		Page
(ϕ)	Polarization Angle of the True Scene	120
(π)	Polarization Angle of the Image	120
$i(x, y, \lambda, \pi)$	Spectral-polarimetric image cube	120
$o(u, v, \gamma, \phi)$	True spatial, spectral and linear polarimetric scene	120
$h(u, v, \gamma, \phi)$	Invariant spectral-polarimetric transfer function	121
$D(x, y, \lambda, \pi)$	One collection of the Spectral-Polarimetric Data Multi-Cube	121
$d(x, y, \lambda, \pi)$	Spectral-polarimetric data cube	121

List of Abbreviations

Abbreviation		Page
SSA	Space Situational Awareness	1
AEOS	Advanced Electro-Optical System	1
MSSC	Maui Space Surveillance Complex	1
LEO	Low Earth Orbit	1
GEO	Geosynchronous Earth Orbit	1
ISR	Intelligence, Surveillance and Reconnaissance	2
DCS	Defensive Counterspace	2
OCS	Offensive Counterspace	2
SSN	Space Surveillance Network	2
LDEF	Long Duration Exposure Facility	3
ASIS	AEOS Spectral Imaging Sensor	4
ASIR-TB	AFIT Spectral Image Reconstruction Test Bench	5
ETFs	Electronically Tunable Filters	5
LCTFs	Liquid Crystal Tunable Filters	5
SOR	Starfire Optical Range	8
AO	Adaptive Optics	8
SILC	Space Object Identification In Living Color	9
AFRL	Air Force Research Laboratory	9
TASAT	Time-domain Analysis and Simulation for Advanced Tracking	10
VIS	Visible, 400nm-720nm	12
NIR	Near Infrared, 720nm-1μm	12
SWIR	Short-wave Infrared, 1μm-2.5μm	12
UV	Ultraviolet, $<$ 300nm	12
MWIR	Mid-wave Infrared, 2.5μm-10μm	12
LWIR	Long-wave Infrared, $>$ 10μm	12

Abbreviation		Page
HYDICE	Hyperspectral Digital Image Collection Experiment	12
AVIRIS	Advanced Visible/Infrared Imaging Spectrometer	12
FOV	Field of View	13
CTIS	Chromotomographic Imaging System	14
SNR	Signal-to-Noise	14
PSF	Point Spread Function	15
AOTFs	Acousto-Optical Tunable Filters	16
RF	Radio Frequency	17
SVD	Singular Value Decomposition	19
PE	Principle Eigenvalue	20
ML	Maximum Likelihood	20
PET	Emission Tomography	20
RMS	Root Mean Square	21
MBSIR	Model-based Spectral Reconstruction	23
SMF	Spectral Mixing Function	24
PMF	Probability Mass Function	25
CCD	Charge Coupled Detector	25
WFS	Wave-Front Sensor	32
RTR	Real-Time Reconstructor	32
DM	Deformable Mirror	32
PBS	Polarization Beam Splitting	35
QE	Quantum Efficiency	36
OTF	Optical Transfer Function	38
HELEEOS	High Energy Laser End-to-End Operational Simulator	46
IS	Integrating Sphere	46
CMOS	Complementary Metal Oxide Semiconductor	53
Hg(Ar)	Mercury Argon	56
Ne	Neon	56

Abbreviation		Page
HR	Harvard Reserve	89
CRLB	Cramér-Rao Lower Bound	93
SRCM	Spectral Reconstruction Capability Metric	113
MBSPIR	Model-based Spectral-Polarimetric Image Reconstruction	119
LPMF	Linear Polarimetric Mixing Function	120

Alphabetical List of Abbreviations

Abbreviation		Page
LPMF	Linear Polarimetric Mixing Function	118
LWIR	Long-wave Infrared, $> 10\mu$m	12
MBSIR	Model-based Spectral Reconstruction	23
MBSPIR	Model-based Spectral-Polarimetric Image Reconstruction	117
ML	Maximum Likelihood	20
MSSC	Maui Space Surveillance Complex	1
MWIR	Mid-wave Infrared, 2.5μm-10μm	12
Ne	Neon	55
NIR	Near Infrared, 720nm-1μm	12
OCS	Offensive Counterspace	2
OTF	Optical Transfer Function	38
PBS	Polarization Beam Splitting	35
PET	Emission Tomography	20
PE	Principle Eigenvalue	20
PMF	Probability Mass Function	25
PSF	Point Spread Function	15
QE	Quantum Efficiency	36
RF	Radio Frequency	17
RMS	Root Mean Square	21
RTR	Real-Time Reconstructor	32
SILC	Space Object Identification In Living Color	9
SMF	Spectral Mixing Function	24
SNR	Signal-to-Noise	14
SOR	Starfire Optical Range	8
SRCM	Spectral Reconstruction Capability Metric	111
SSA	Space Situational Awareness	1
SSN	Space Surveillance Network	2
SVD	Singular Value Decomposition	19

Abbreviation		Page
SWIR	Short-wave Infrared, 1μm-2.5μm	12
TASAT	Time-domain Analysis and Simulation for Advanced Tracking	10
UV	Ultraviolet, $<$ 300nm	12
VIS	Visible, 400nm-720nm	12

Reconstructing Spectral Scenes Using Statistical Estimation to Enhance Space Situational Awareness

I. Introduction

The characterization of objects in space is essential for US space superiority and its enabling mission area, Space Situational Awareness (SSA). An in-depth understanding of objects in orbit is also needed for increased utilization of space by civil and commercial entities [4]. While the majority of the objects of interest are man-made satellites, the characterization of some natural space objects is also needed to analyze the space environment. The Advanced Electro-Optical System (AEOS) and the Spica spectrometer, both located at the Maui Space Surveillance Complex (MSSC), have been used to characterize satellites and other space objects to enhance SSA.

AEOS collects panchromatic images of satellites in Low Earth Orbit (LEO) to determine the satellite's geometric characteristics, such as size, shape and general features [10]. Spica measures the spectra of satellites in both LEO and Geosynchronous Earth Orbit (GEO) to determine the satellites more specific physical characteristics such as predominant material type. [27, 32]. While the images collected with AEOS, and the spectra captured with Spica, provide useful information for SSA, the combination of these two sensing modalities would be even more valuable. This synergy would provide a powerful way to understand detailed physical characteristics of satellites, such as material mapping, the identification of hidden payloads, as well as anomaly detection and resolution.

1.1 Space Situational Awareness

The spectral imaging of satellites is a subset of the broad area known as remote sensing. While general remote sensing is "the attempt to measure something at

a distance," spectral imaging of a satellite is an attempt to measure the spatially resolved spectra of an object in space from a ground-based sensor [44]. By measuring the resolved spectra of the satellite, increased knowledge of the satellite's physical characteristics can be determined. This enhanced satellite characterization is vital for current and future US space superiority and continued advancements in space technologies [1,4]. The conduct of Intelligence, Surveillance and Reconnaissance (ISR) to increase the understanding of satellites and other space objects is included in an area known as Space Situational Awareness and contribute to the areas of Defensive Counterspace (DCS) and Offensive Counterspace (OCS) [4].

From the Air Force Space Command Strategic Master Plan, "SSA is the permanent crucial enabler for DCS and OCS [4]." SSA describes what capabilities are in space, as well as what has happened and is happening in space. SSA considers not only the numerous satellites in orbit, but also the space environment. While this sounds simple enough, knowing everything that is in, is happening or has happened in space is difficult to achieve.

SSA begins with the tracking of all space objects. Many years of research and effort have gone into increasing the capability of the Space Surveillance Network (SSN) and won't be discussed further [48]. While SSA begins with space-track, the power of SSA is the characterization of the satellite. Characterizing a satellite includes understanding the satellite's physical properties, as well as its performance and capabilities.

Different sensors are used to characterize satellites and other space objects. While these sensors provide valuable information, they sometimes fall short in determining many of the satellite's basic physical features. One new source that shows promise in helping fill in these shortfalls is spectral imaging.

1.2 Benefit of Spectral Imaging for SSA

Spectral imaging will provide valuable information on satellites in four areas. These areas are 1) material classification, 2) trending material degradation, 3) iden-

tifying hidden payloads, and 4) anomaly detection and resolution. While current SSA sources provide some information in these areas, spectral imaging may give more complete answers. Each of these areas is important for achieving the goals of SSA and are critical in fulfilling OCS and DCS mission requirements.

1.2.1 Material Classification. The classification of materials on a satellite is needed for a variety of reasons. Much of the analysis done to support SSA relies on accurate models of satellites, where the materials in these models are critical. While spectral imaging cannot determine the materials inside a satellite, it can help determine the external materials. Classifying the materials on a satellite is a start to better meeting these material knowledge requirements.

The classification of the material will be done by comparing the collected spectra to a database of known material spectra. Since the spatial scene is also collected as part of the spectral image, spectra for different areas of the image can be compared to the material database. The comparison of the spectra from the entire scene allows for the material classification of the different parts of the satellite.

1.2.2 Trending Material Degradation. An offshoot of material classification is trending the change or degradation of the satellite's materials while the satellite is on orbit. The degradation of the satellite's materials, such as the glass covering the solar panels, could translate into a reduced capability. The reduction in the satellite's capability is important knowledge for SSA.

Understanding how a material changes while on-orbit is not only important for SSA, but also for satellite designers and operators. To date, different missions, such as the Long Duration Exposure Facility (LDEF), have flown a wide variety of materials in space and then returned them to Earth for spectral analysis [28].

With a spectral imaging sensor, the spectral analysis can be done while the spacecraft is on-orbit, providing a time-dependent analysis. The time-dependent analysis can be done by measuring the spectra of the materials before launch, or just after

the satellite arrives on orbit. Spectral images of the satellite can be taken periodically to determine the changes in the materials spectra as the materials are effected by the space environment.

1.2.3 Identifying Hidden Payloads. A major concern, especially in the DCS community, is the use of hidden payloads or piggy-back satellites to provide an undisclosed satellite capability [5]. Since these hidden payloads and sub-satellites could have different materials than the surrounding host spacecraft, spectrally imaging a satellite has the potential for identifying areas of interest where these hidden objects may be located. These areas of interest can be detected by searching for locations of material discontinuities, seen as changes in the spectra of the satellite. A discontinuity in the satellite's material located in an unexpected place could be a tip-off for a hidden payload.

1.2.4 Anomaly Detection and Resolution. Spectral imagery will also help determine and resolve on-orbit anomalies, when the anomalies are detectable on the exterior of a satellite. A spectral image will be able to help determine the nature and extent of the anomaly by measuring the differences in material spectra around the anomaly. This could provide a detection capability even when the anomaly is too small or lacks sufficient contrast to be detected in traditional panchromatic images. This type of data could prove to be extremely valuable in determining the location and magnitude of the anomaly.

1.3 AEOS Spectral Imaging Sensor

The development of the AEOS Spectral Imaging Sensor (ASIS) was started in March 2003. The purpose of the project is 1) design, build and install a spectral imaging sensor as part of AEOS, 2) collect and analyze data, and 3) develop algorithms to support SSA. By combining a set of highly tunable filter/camera combinations with the large aperture and atmospheric compensation of AEOS, ASIS is able to collect images of space objects that have both high spatial and spectral resolution. While

the exact spatial and spectral resolution depends on the parameters of the sensor and the geometry of the collection, ASIS is able to differentiate spatial features on a satellite and spectral features in the satellite's spectra. ASIS uses commercially available optics and is scalable for increased sensor performance.

1.4 AFIT Spectral Image Reconstruction Test Bench

While ASIS is the primary sensor used for this research, a second sensor was constructed to test the post-processing algorithms designed for ASIS data. The AFIT Spectral Image Reconstruction Test Bench (ASIR-TB) is much less complex then ASIS, but contains similar elements. ASIR-TB provides the ability to spectrally image a wide variety of sources without having to compete for limited AEOS mount time.

1.5 Contributed Research

There are three main areas of research presented in this dissertation. The first two develop new algorithms to post-process data from spectral imaging sensors that have overlapping spectral sampling, such as ASIS. These algorithms allow for better exploitation of the data and meet the third goal of the ASIS project discussed in section 1.3. The third area is a methodology to quantify how well the algorithms can perform.

1.5.1 Spatial-Spectral Image Reconstruction. This research provides the first statistical approach for simultaneously improving the spatial and spectral resolution of spectral images collected with Electronically Tunable Filters (ETFs), such as the Liquid Crystal Tunable Filters (LCTFs) used in ASIS. The statistical approach is different from other methods, such as Singular Value Decomposition or Principal Eigenvalue, because it requires no *a priori* knowledge and reduces both the spatial and spectral blurring. While the method is targeted for data collected with ASIS, it is applicable to any systems using an ETF with typical detector noise.

1.5.2 Spectral-Polarimetric Image Reconstruction. The research also develops the first spectral-polarimetric reconstruction algorithm for data collected with LCTFs. The LCTFs used in ASIS require the creation of separate linear polarimetric images to capture all of the photons from the object. These linear polarimetric images can then be summed and used with the spectral reconstruction algorithm, or can be kept separate for a spectral-polarimetric reconstruction. As with the spectral reconstruction algorithm, the purpose of the spectral-polarimetric algorithm is to reduce the effects of sensor blurring on the data. However, for this case a spectral-polarimetric scene is reconstructed.

1.5.3 Performance Bounds and Metrics. The research provides the first quantitative measure of the theoretical best performance of any reconstruction algorithm for images collected with an ETF. The quantitative measure is performed by calculating the performance bounds of the algorithm. For this research, the performance bound for the spectral resolution and accuracy will be determined.

The bounds can be used as a way to predict the performance of the post-processing reconstruction algorithm for different sensor parameters. By comparing the performance metrics, a set of system parameters can be determined that lead to improved joint algorithm/sensor performance given different operational constraints.

1.6 Outline

The dissertation is divided into ten chapters. Chapter 2 provides a brief background on the spectral imaging of satellites, with an emphasis on current non-spectral imaging and non-imaging spectral sensors. The second chapter concludes with a brief discussion of other spectral reconstruction methods and introduces the statistical method used in this research. Chapter 3 provides a derivation of the spectral image reconstruction algorithm, while the Chapter 4 introduces ASIS and ASIR-TB and develops a model for each sensor. Chapter 5 presents the simulated reconstruction of several different sources collected with ASIS and ASIR-TB. Chapter 6 shows the

performance of the spectral image reconstruction algorithm on data collected with the sensors. Chapter 7 derives two different Cramér-Rao Lower Bounds on the performance of the spectral reconstruction algorithm used on ASIS and ASIR-TB data. From these lower bounds, Chapter 8 develops a metric that can be used to compare performance of different ASIS sensor parameters. Chapter 9 briefly describes how the spectral image reconstruction algorithm can be extended to estimate the linear polarization components in the spectral-polarimetric image. The last chapter discusses the potential for future research areas and summarizes the research presented in the dissertation.

II. Background

Different imaging and non-imaging techniques have been developed to characterize satellites. This chapter will review two of the current techniques that relate to spectral imaging and describe how ASIS will advance these techniques. The chapter then gives a general description of spectral imaging, the different methods to produce spectral images and introduces the versatile filters used for ASIS. The chapter concludes with the focus of this research, a discussion of the processing required to reduce the spectral blurring when using these filters.

2.1 Current Techniques for SSA

Two techniques related to spectral imaging are currently used to provide information for SSA. The first is the imaging of a satellite using a ground-based telescope. This technique provides the information on physical aspects of the satellite, such as size, shape, and component location. The second technique is the measurement of the spectra of the satellite.

2.1.1 Ground-based Imaging of Satellites. Images of space objects have been available since the advent of the first telescope. Currently, the DoD has two facilities capable of collecting high-quality images of satellites: Starfire Optical Range (SOR) and the MSSC. Both sites have multiple telescopes offering different aperture sizes that can image satellites with varying spatial resolutions. Some of the sensors use an adaptive optics (AO) system to improve the image's resolution, while other images are post-processed [8, 39] Both SOR and the MSSC have been successfully used to determine the size and shape of both small and large satellites, as well as satellite component locations and orientations [22]. High resolution images have also been used to aid in the anomaly investigation of satellites on-orbit [14]. One of the many advantages of using SOR and MSSC for imaging is the ability of the sensor to track the object as it transverses across the sky. By watching the object over time, features can sometimes be seen that are not noticeable in an image from a single orientation. In addition, the natural rotation of the object as it crosses the sky leads to numerous

viewing angles that further increases the value of the images [45]. This knowledge can then be used to build accurate models of space objects used for SSA analysis.

Valuable information has been gained from panchromatic images. However, other data needed for satellite characterization, such as the type of material used to construct the satellite and the function of satellite components, cannot be determined from these images. New methods that enhance the value of the imagery are required. Collecting the spectra of the satellite, along with the image, is one such method to more fully, but not completely, characterize the satellite.

2.1.2 Spectra Measurements. Two spectral sensors have been used to demonstrate the potential for spectral exploitation of satellites. The Space Object Identification In Living Color (SILC) program and the Spica sensor have measured the spectra of numerous space objects.

2.1.2.1 SILC. SILC is an Air Force Research Laboratory (AFRL) program investigating non-imaging techniques to determine GEO satellite identity and location. The satellites of interest for SILC are in GEO and the spectra of the satellites is sampled with different broadband spectral filters without resolving any supporting spatial information. The program looked at two different sets of four astronomical filters in a 24" telescope [41]. By looking at a color-magnitude plot of a geosynchronous object, SILC has shown it is possible to identify different satellites from the spectral signature. This is possible because each satellites has different materials leading to a unique spectral signature. These signatures do not vary because the satellite, being in GEO, offers the same perspective to the sensor over time. Therefore, the spectral signatures observed will remain constant from measurement to measurement. The location of the satellites can be determined by tracking these unique signatures [40].

2.1.2.2 Spica. The Spica spectrometer mounted on the 1.6m telescope at MSSC has been used in support of SILC and for other non-imaging spectral research

[32]. Experiments with the Spica spectrometer are similar to those conducted in the SILC program, except the spectral resolution of Spica is much greater due to the use of a grating spectrometer. As with SILC, the spectra of the satellite is measured without resolving any spatial information.

Research with Spica is attempting to go beyond conventional non-imaging techniques that only determine satellite identity and location. The Spica spectra measurements are being used in a model-based algorithm for estimating the size and shape of satellite features, as well as material types [32]. This is done in a model-based approach. Using an estimated model of a satellite, complete with materials, the Time-domain Analysis and Simulation for Advanced Tracking (TASAT) software is used to simulate the spectral return from the satellite. A match is then attempted between the TASAT simulation and data collected with Spica. Algorithms can then be used to determine the changes necessary to the size, shape, and materials on the model to better match the observed data, with continued iterations until the best fit is achieved [32]. Spica has also been used to attempt to discriminate between different LEO rocket bodies and satellites and was successfully used to discriminate between spacecraft with different sized solar panels [23].

Blind deconvolution methods are also being explored in the analysis of Spica data. Since the spectra of each satellite is collected without any spatial information, the spectra of the different materials is mixed. An iterative algorithm is being investigated to jointly estimate the spectra and fractional abundance of the different materials on the spacecraft [34].

In this research, another method of returning the spectra and abundance of different materials will be explored. By collecting the spatial scene and the spectra simultaneously, the blind deconvolution is not needed. Instead, the spectra and material properties are measured directly from the post-processed spectral image cube. An additional benefit is that the locations of the spectra on the satellite can also be determined.

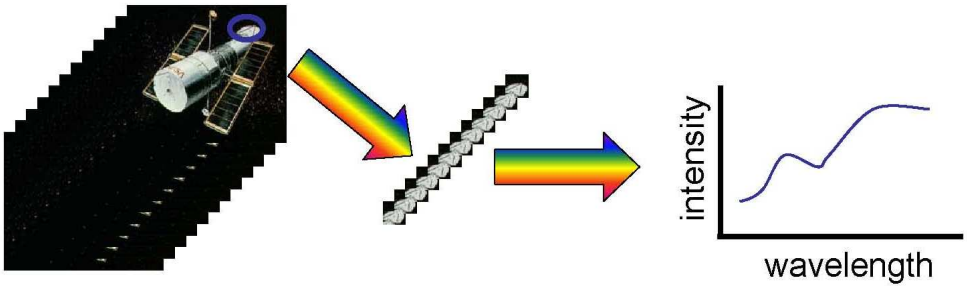

Figure 2.1: A representative spectral image cube [44].

2.2 Spectral Imaging

Spectral imaging is the collecting of photons emitted or reflected from an object into specific wavelength-dependent bins [44]. While the mechanics of the photon collection are similar to panchromatic imaging, the division of the photons into well-specified bins makes spectral imaging a more powerful tool for characterizing the imaged scene. A spectral image cube is created by stacking the individual spectral scenes in each spectral bin on top of each other as shown in Figure 2.1. From this image cube, a vector of pixels extending through the image can then be extracted to give the spectra of the scene at one spatial location [30]. Spectral imaging is similar to non-imaging spectral analysis, except the spectra of the individual elements of the object can be recovered [7].

Figure 2.2 gives the general concept of spectral imaging as applied to ASIS. Sunlight is reflected off of the satellite according to the spectral reflectance of the satellite's materials to create the true spectral scene, $o(u, v, \gamma)$. The scene is then propagated through the atmosphere where it is subject to spectral losses and spatial blurring. The scene is collected by the optics, passed through a filter and imaged onto the imaging array. The data, $D(x, y, \lambda)$, is the spectral image collected by the imaging array.

2.2.1 Spectral Bands. For this research, spectral imaging will be defined as using light from 400nm to 2.5μm in the electromagnetic spectrum. This spectrum will

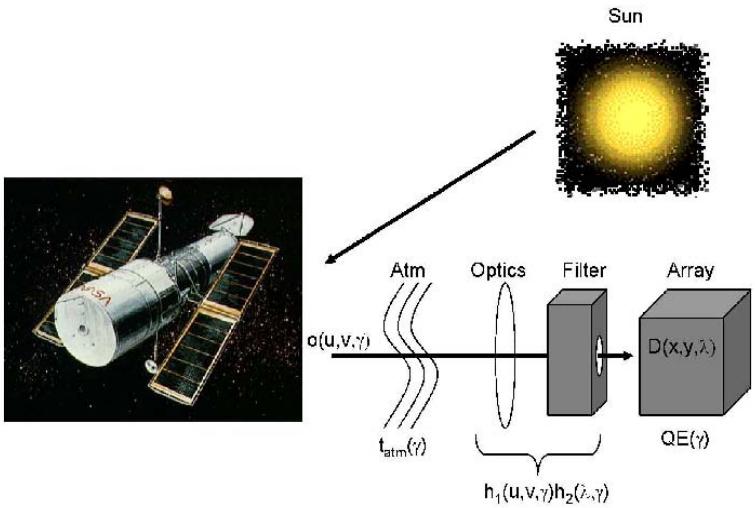

Figure 2.2: General concept of spectral imaging [24]. The illuminating spectra of the sun is spectrally reflected off of the satellite and collected by the sensor after propagating through the atmosphere.

be divided into distinct subranges that extend from the visible (VIS, 400nm-720nm), through the near infrared (NIR, 720nm-1μm), to the short-wave infrared (SWIR, 1μm-2.5μm), Spectral images can also be collected in the ultraviolet (UV), starting at about 300nm, the mid-wave infrared (MWIR, 2.5μm-10μm) and the long-wave infrared (LWIR, beyond 10μm), but these bands are not used in this research.

2.2.2 Spectral Selectors. Different spectral imaging systems have been developed and used to image terrestrial objects and scenes for many purposes [44]. These systems come in a wide variety, from ground-based sensors for both lab and outdoor imaging, to airborne systems such as the Hyperspectral Digital Image Collection Experiment (HYDICE) and the Advanced Visible/Infrared Imaging Spectrometer (AVIRIS), to even a few satellites such as LANDSAT and the SPOT HRV [44]. The systems range from multispectral (a few to dozens of spectral bands collected per image) to hyperspectral (hundreds of bands per image) to ultraspectral (several

hundreds of bands per image) and are used for classifying materials, differentiating between natural and man-made substances, and monitoring the environment [30]. The systems employ a variety of spectral selectors to separate light for the creation of a spectral image. The four more prevalent types of spectral selectors include prisms and gratings, Fourier interferometry, chromotomography, and filters.

2.2.2.1 Prisms and Gratings. Prisms and gratings represent existing ways of splitting light into its spectral components. With a prism, light is split into its components due to the wavelength dependence of the prism's index of refraction according to Snell's Law [25]. The grating uses a periodic structure of diffracting elements to scatter the light into a spectrum [25]. The spectrally separated light is collected by different pixels in the imaging array.

When only a few spectral bands are collected, multiple 2-D imaging arrays can be used to collect the spatial and spectral components of the scene simultaneously [30]. For this case, each 2-D array collects the 2-D scene in a different spectral band. When more than 4-10 bands spectral bands are required, using a 2-D imaging array to collect the different spectral scenes is usually not possible due to practical space limitations in the sensor. When many bands are required, a push-broom sensor is usually employed.In a pushbroom sensor, images are created one line at a time as the thin sensor field of view (FOV) is scanned along the object of interest [30]. In this case, a 2-D imaging array is not used to collected the 2-D scene. Instead, one axis is for the 1-D spatial extent of the scene and the other axis captures the spectra at these locations. The image cube is obtained by scanning across the scene and combining the collected data.

The 1-D entrance slit limits the utility of the sensor when imaging non-stationary objects. The 1-D slit is ideally suited for imaging the ground with a sensor flying or orbiting above. The inherent motion of the sensor as it sweeps across the ground provides the natural linear motion needed to collect the vertical spacing in the imaged scene. However, if the scene changes during collection, the changes in the scene will not

be well represented in the spectral image cube because of the linear scan. Additionally, if used to image a satellite from the ground, scanning a 1-D slit across the orbiting satellite requires precise synchronization of the satellite tracking and the scanning of the entrance slit. If the tracking of the satellite has any jitter, as is always the case, this synchronization is difficult.

2.2.2.2 Fourier Spectroscopy. Fourier spectroscopy utilizes an interferometric approach to analyzing the different wavelengths. An interferometer, such as a Michelson, can be used to stare at a scene while one of the two mirrors in the interferometer is moved to create a interferogram for the entire image [20]. While very high spectral resolution is possible with Fourier spectroscopy, the scene must be stationary or the motion in the scene must be known [30]. This method is of limited use when imaging satellites due to the unknowns in the motion of the satellite as it is being imaged.

2.2.2.3 Chromotomography. Chromotomographic imaging systems (CTIS) use a rotating grating or prism to image a dispersed view of a scene over all spectral bands [38]. The advantage of a chromotomographic system is that the entire spectral image is observed with little or no transmission loss. This allows for spectrally imaging an entire scene in a short time when the scene provides sufficient signal-to-noise (SNR). However, as the SNR is reduced, the rotation of the prism must be slowed, increasing the image collection time.

One drawback of a CTIS is the cone of missing information [38]. The cone of missing information is the portion of the collected data that cannot be reconstructed for analysis. Of particular concern is that the cone of missing information makes recovering the radiometry of the scene very difficult. This is because the missing information is around the DC region in the spatial frequency domain. Without knowing the DC level, it is not possible to recover radiometrically accurate spectral cubes.

Another drawback of chromotomographic systems is that the data must be reconstructed to be analyzed [16]. The reconstruction is required because the spectral images are actually overlapped both spatially and spectrally on the array and must be processed to be sorted back into a spectral image cube. CTIS systems must reconstruct the spatial and spectral portions of the image simultaneously, since all of the spatial and spectral information is captured simultaneously on the imaging array. Because of this, a CTIS imaging system must know the Point Spread Function (PSF) used to collect the image for every wavelength within the spectral image cube. If the PSF is not known, then no spectral information can be obtained from the CTIS. This proves to be a problem since the PSF of the optics is difficult to calculate in CTIS systems. In situations where a complete spatial reconstruction is not required, a 1-D CTIS reconstruction can be done [21]. With the 1-D reconstruction, the spectra is fully captured, but the reconstruction only captures part of the spatial information.

2.2.2.4 Filters. Instead of refracting or diffracting light into its spectral components, filters selectively transmit only a certain portion of the light. Imaging a scene is easier when using filters since the entire 2-D scene can be collected in one image, but the collected scene is only for the wavelengths transmitted by the filter. For a full spectral image cube, multiple filtered images must be combined and aligned so that all pixels represent the same location in the scene. When multiple filters are used to collect the scene, any differences between the filters must be taken into account [44]. Since each image of the cube must be collected separately, it may take longer to collect the spectral image of a scene using filters then other methods. The limiting factor in the time it takes to collect the spectral image cube is the cycling time of the filters. For a non-stationary object, the cycling time of the filters must be less than the time it takes for the object to substantially change its orientation to the sensor.

2.2.2.5 Electronically Tunable Filters. ASIS requires a spectral selection scheme that allows for spectrally imaging non-stationary objects in many spectral

bands. This requirement eliminates the use of a prism or grating system, as well as Fourier Spectroscopy, because of the difficulties involved with using these systems that were discussed in the previous sections. A CTIS sensor is not a viable option because of the radiometric problems due to the cone of missing information.

Filters were the preferred option for ASIS given the sensor requirements, as well as other consideration such as cost and schedule. However, the filters must 1) have variable spectral passbands to collect the spectra across a spectral range and 2) be able to switch rapidly between these passbands. Electronically tunable filters met both of these criteria. ETFs allowed ASIS to collect a full spectral image cube of a satellite without any significant change in orientation.

ASIS uses an ETF technology known as LCTF. The LCTFs are an electronically controllable filter, with one filter providing 100's of selectable passbands. Selectable passbands are produced by using multiple phase retarders to destructively interfere light outside of a narrow bandwidth. The cycling or switching time of LCTFs is approximately 50ms, which is fast enough to image a satellite in 50-100 spectral bands without a significant orientation change. One of the drawbacks of using LCTFs are the low transmission levels, as low as 5% in some cases. To reduce the effect of the low transmissions, the bandwidth of the filter is kept larger than desired for some spectral imaging applications. The larger bandwidth, up to 20nm, provides more light transmission for a greater signal-to-noise which results in better images. However, the large bandwidth adversely affects the spectral resolution. For some applications, the reduced spectral resolution will not be critical. For others, it will degrade the usefulness of the spectral image. While post-processing of ASIS data is not required, some processing of the images to improve the quality may be beneficial.

Other ETFs, such as Acousto-Optical Tunable Filters (AOTFs), are another option for ASIS. While AOTFs do have higher transmissions, they provide a smaller field-of-view, which would limit the utility of ASIS. Additionally, controlling the wavelength selection in an AOTF is more difficult then in a LCTF. The transmission band

of the AOTF is varied by varying the frequency of a radio frequency (RF) source applied to the AOTF crystal. The RF applied to the crystal creates an acoustic wave that causes the crystal lattice to be alternatively compressed and relaxed [18]. The compression and relaxation cycle produces a density change that ultimately varies the crystals index of refraction. This in-turn produces two narrow bandwidth beams of light that can be used to create a spectral image [17].

While LCTFs are currently used in ASIS, AOTFs or another ETF could be used in the future. As with the LCTFs, other ETFs can have a bandwidth large enough to allow for spectral blurring within the spectral image. The same processing that will reduce the spectral blurring in the LCTF spectral images, will also work with other ETF technologies.

2.3 Spectral Image Processing

Most spectral images need some basic post-processing. These calibration oriented post-processing steps include: 1) ensuring all the pixels in the image are properly aligned (also known as registering), 2) correcting for radiometric loses within the sensor, and 3) correcting for external affects, such as atmospheric losses and geometric considerations.

In addition to the items listed above, many systems using ETFs require methods to reduce the spectral blurring in the image. By reducing the spectral blurring, the spectral resolution and spectral accuracy of the image can be increased over an image with no post-processing. The spectral blurring in ASIS is introduced by the large bandwidth of the LCTFs. These large bandwidths integrate light from wavelengths adjacent to the center wavelength when forming the image. The integration of the wavelengths has the effect of blurring the spectra such that the spectra has been altered and can no longer be directly retrieved from the data. Figures 2.3 and 2.4 gives an example of spectral blurring. In Figure 2.3, the spectral features shown as the dashed lines are blurred when collected with the large bandwidth ETFs. An

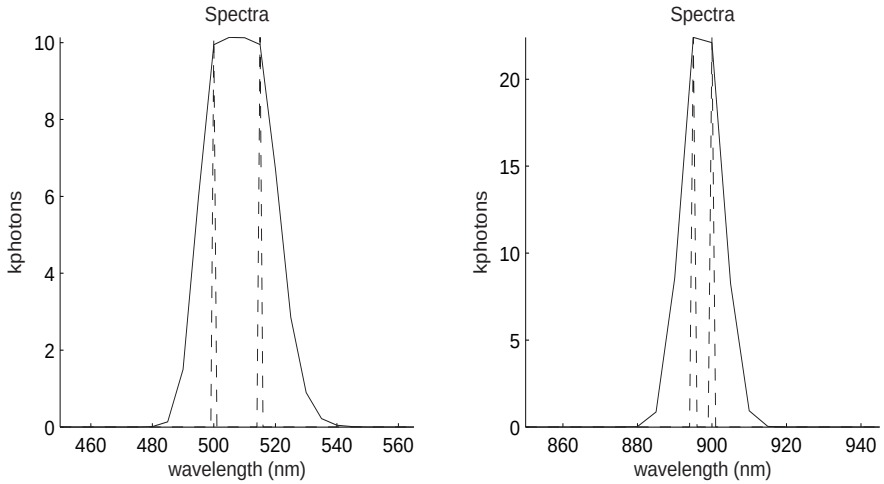

Figure 2.3: Simulated spectral output of an ETF system showing the spectral blurring that can occur due to the large bandwidths used in the filters. Two spectral feature, shown in the dashed lines, at 500nm and 515nm in the VIS and 895nm and 900nm in the NIR are collected with a ETF having a 20nm bandwidth in the visible and a 10nm bandwidth in the near-IR. The collected spectra, shown in the solid lines, show the spectral features are not resolvable.

algorithm that reduces the spectral blurring will reconstruct the spectral features, as shown in Figure 2.4.

There are four techniques that have been investigated to reduce the spectral blurring to restore the original collected spectra when using a LCTF. All of these techniques attempt to develop a method to invert the spectral blurring function. However, the first three techniques are not applicable to data from a remote sensing system such as ASIS. A variation on the fourth technique used for gamma-ray spectroscopy and chromotomographic system shows much more promise to reduce the blurring from images collected with an ETF. This technique has the additional advantage of being able to reduce the spatial blurring at the same time as the spectral blurring.

2.3.1 Direct Inverse. The simplest method to remove the spectral blurring from the image is to directly invert the blurring function. The image of a scene

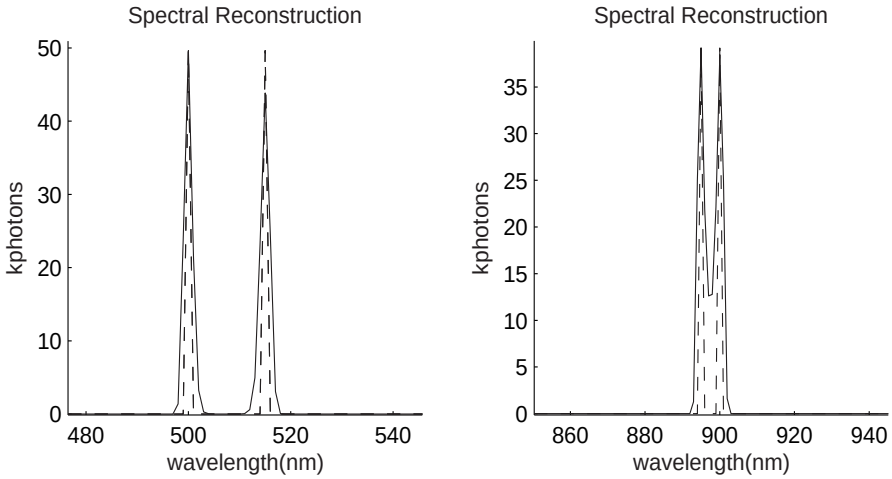

Figure 2.4: Simulation of the spectral reconstruction of the previously unresolvable spectral features. The spectral features, shown in the dashed lines, are at 500nm and 515nm in the VIS and 895nm and 900nm in the NIR. A reconstruction algorithm that improves spectral resolution will be able to process the spectra so the features are resolvable. The reconstructed spectra is shown in the solid lines.

collected by the sensor can be viewed as,

$$i(x, y, \lambda) = o(x, y, \gamma) \otimes h_2(\lambda, \gamma) \tag{2.1}$$

which states that the image, $i(x, y, \lambda)$, is the true scene, $o(x, y, \gamma)$ convolved with the spectral blurring function, $h_2(\lambda, \gamma)$ [18]. While it might seem straight forward to invert the spectral blurring function to retrieve the true scene according to,

$$o(x, y, \gamma) = i(x, y, \lambda) \otimes h_2^{-1}(\lambda, \gamma), \tag{2.2}$$

it is actually impractical to implement. The spectral mixing function can be viewed as a matrix of transmission values. The sparseness in this matrix prevents the function from being invertible. Without an invertible function, this method cannot be used.

2.3.2 Singular Value Decomposition. Since the spectral blurring function is not directly invertible, a Singular Value Decomposition (SVD) of $h_2(\lambda, \gamma)$ has been attempted to provide a pseudo-inverse [18]. With the calculated pseudo-inverse, a

method can be developed that uses the collected spectra of a known spectral reference standard, as well as a bright field and dark cube to restore the measured spectra [18]. Without using the reference standard and other calibration measurements, the pseudo-inverse has shown poor results on collected data due to the noise in the images [24]. Collecting the required calibration measurements would be difficult with a remote sensing instrument such as ASIS. It is not practical to either image a bright field or reference standard given the size of the ASIS aperture.

2.3.3 Principal Eigenvalue. A Principle Eigenvalue (PE) method has been shown to be useful in retrieving the true spectral scene when the spectra of the scene is known. In this case, an inverse is developed that uses the "statistical spectral information of the imaged objects." The PEs of this object-dependent inverse are used to create and pseudo-inverse [24]. The PE reduces the noise sensitivity of an inverse to the spectral response by taking only the vectors corresponding to the n most significant singular values, where n is a number specified by the user. However, this technique has only been shown to be successful when the spectrum of the scene was measured and used in the spectra restoration algorithm. While this is useful for some applications such as calibrating cameras, it is impractical for any remote sensing application, since the spectra of the scene is not known.

2.3.4 Statistical Methods. A statistical method based on a maximum likelihood (ML) estimator has been used to improve the resolution of the spectra in gamma-ray spectroscopy and of an image from a CTIS [35]. The ML estimator was able to double the spectral resolution of the energy-loss spectra from the gamma-ray spectroscopy. Maximum likelihood estimators have also been shown to be able to deconvolve the images from a CTIS [21]. These methods are derived from an older algorithm developed to reconstruct the data for Emission Tomography (PET) [47].

2.4 Expected Results

In this research, another method has been taken to invert the spectral blurring in ETF systems such as ASIS. The new method is based on the same ET algorithm, but includes the specific functionality required when dealing with ETFs. The new method is similar to the ML estimator used for improving the spectral resolution of gamma-ray spectroscopy, but expands the estimator to include a three-dimensional (two spatial dimension and one spectral dimension) image, instead of a one-dimensional spectra. Despite the inclusion of the spatial reconstruction, the spectral resolution will continued to be doubled. Therefore, the algorithm will increase the overall capability of the ML estimator developed for the gamma-ray spectroscopy.

The new algorithm also has better performance then the SVD and PE methods discussed in the previous section. The algorithm will be able to reduce the root mean square (RMS) error for the reconstruction of a continuous spectra by half. In addition to improving the RMS error, the algorithm will improve the reconstruction without using any *a priori* knowledge of the images scene.

2.5 Summary

Spectral imaging will provide valuable information to advance SSA. SSA is required to protect our space assets and to guarantee that those assets will be available when the nation needs them. While there are no current sensors dedicated to spectral imaging for space objects, two systems at the MSSC have been successfully used to collect spatially resolved images and non-resolved spectra. The synergy of these two technologies will provide the resolved spectral information needed to advance space awareness.

The requirement for ASIS to image non-stationary objects in space limits the choice of spectral separators. ETFs provide the only viable option. The ETF technology chosen for ASIS is the LCTF.

While most spectral sensors need some post-processing for calibration, information from some sensors can be improved through additional post-processing. By reducing the spectral blurring introduced in the sensor, the spectral resolution can be increased. The increase in this resolution may not be critical for some applications, but for others, the increased resolution may prove to be valuable.

There are no methods currently available to improve the spectral resolution of data from ASIS. Direct inversion techniques are unreliable do to noise and other pseudo-inverse methods rely on knowing the spectra of the true scene. A statistical approach has been useful in other application and promises better results. However, the algorithms for the statistical approach must be derived for the case of an ETF.

III. Model Based Spectral Image Reconstruction

Most spectral imaging systems that use ETFs have limited spectral resolution due to the ETFs non-trivial bandwidths. In such systems, the bandwidth allows a range of wavelengths to be integrated together when the spectral image is collected. The integration of the wavelengths reduces the sensor's spectral resolution. For some applications, the reduction in the spectral resolution is not critical. For other applications, the reduced spectral resolution will lower the value of the collected data. By understanding the way in which the sensor blurs the wavelengths to create the spectral image cube, it is possible to use estimation theory to reconstruct the spectral scene with less spectral blurring. The estimator requires two key elements: 1) the statistics of the noise in the image and 2) an in-depth knowledge of the spectral imaging sensor, with an emphasis on understanding the spectral blurring within the sensor. With knowledge of these two elements, a Model-based Spectral Image Reconstruction (MBSIR) algorithm can be developed to reduce the spectral blurring in systems that use ETFs.

In addition to improving the spectral resolution of the images, the MBSIR algorithm simultaneously increases the spatial resolution. The only additional requirement is to understand the spatial blurring in the sensor.

This chapter steps through the development of the MBSIR algorithm. It starts with defining a basic underlying assumption for how an image is created and then moves into deriving the noise statics for the image collection. The MBSIR algorithm is then developed, followed by a spectral only MBSIR algorithm that is useful in certain applications. Finally, the stopping criteria for the algorithm is discussed.

3.1 MBSIR Background

The underlying assumption for MBSIR is that the image created by the spectral imaging sensor can be mathematically described by [11],

$$i(x, y, \lambda) = \int_{-\infty}^{\infty} \int o(u, v, \gamma) h_1(x - u, y - v, \gamma) h_2(\lambda, \gamma) du dv d\gamma \tag{3.1}$$

or in discrete terms,

$$i(x, y, \lambda) = \sum_{u,v,\gamma} o(u, v, \gamma) h_1(x - u, y - v, \gamma) h_2(\lambda, \gamma) \tag{3.2}$$

where $i(x, y, \lambda)$ is the set of noise-free spectral images calculated when the blurring functions, $h_1(u, v, \gamma)$ and $h_2(\lambda, \gamma)$, are applied to the true spectral scene, $o(u, v, \gamma)$, at the selected wavelengths (often referred to as the spectral image cube). This image cube is the result of the inherent blurring, both spatially and spectrally, of the sensor. The spatial blurring, h_1, is described by the sensor's PSF. The spectral blurring, h_2, is described by the Spectral Mixing Function (SMF) which includes both the effects of spectral blurring and amplitude attenuation. In Equations (3.1) and (3.2), (u, v, γ) represents the spatial (u, v) and spectral (γ) coordinates of the spectral scene, and (x, y, λ) represents the spatial (x, y) and spectral (λ) coordinates of the spectral image cube. The blurring functions h_1 and h_2 are separate because the spectral blurring in ETFs is spectrally variant. As section 4.1.4 will show, the transmission and bandwidth of the ETFs used in ASIS will vary with the selected center wavelength. For a system that is spectrally invariant, Equations (3.1) and (3.2) could be written as,

$$i(x, y, \lambda) = \int_{-\infty}^{\infty} \int o(u, v, \gamma) h(x - u, y - v, \lambda - \gamma) du dv d\gamma, \tag{3.3}$$

or in discrete terms,

$$i(x, y, \lambda) = \sum_{u,v,\gamma} o(u, v, \gamma) h(x - u, y - v, \lambda - \gamma). \tag{3.4}$$

where $h(u, v, \gamma)$, represents the invariant spatial and spectral transfer function. Although the MBSIR algorithm is derived for the spectral variant sensor, it will also be applicable to a sensor that is spectrally invariant, since the spectrally invariant case is subset of the variant case.

3.2 Image Statistics

The first step in deriving the MBSIR algorithm is to understand the noise statistics within the imaging system. These statistics form the foundation of the estimator developed for MBSIR. The estimator is developed by maximizing the probability mass function (PMF) of the measured image. The imaging arrays used for ASIS are low read noise charge coupled detector (CCD). Additionally, ASIS uses 12-bit imaging arrays so there will be little quantization noise. The imaging arrays will also be calibrated for signal to photon conversion. Therefore, for ASIS, the noise statistics will be dominated by the uncertainty in photon arrival.

ASIS uses polarizers within its spectral filters, so it is an imaging systems that collects polarized light, also referred to as polarized thermal light [20]. For polarized light, the statistics of the photon arrival is determined by the count degeneracy parameter [20]. The imaging time used for ASIS, on the order of milliseconds, will be much greater than the temporal coherence of the collected incoherent light. The count degeneracy parameter, physically described as the average number of counts which occur in a single coherence interval, will therefore approach zero [20]. Therefore, the noise associated with creating an ASIS spectral image will follow a Poisson distribution. While the statistics are discussed for ASIS, the image reconstruction will apply to any spectral imaging systems where the noise follows a Poisson distribution.

The data collected by an ETF system dominated by Poisson distributed noise, $d(x, y, \lambda)$, is related to the image, $i(x, y, \lambda)$, given in Equation (3.2) by the addition of Poisson distributed noise, $n(x, y, \lambda)$ according to,

$$d(x, y, \lambda) = i(x, y, \lambda) + n(x, y, \lambda). \tag{3.5}$$

Since the noise in Equation (3.5) is a random variable, and the image is deterministic, the data will be a random variable with a Poisson distribution.

3.3 Spectral Image Reconstruction

With the Poisson distribution established, a maximum likelihood estimator can be developed by maximizing the *a priori* PMF [49]. By maximizing the PMF, the estimator will provide an estimate of noiseless scene from which the collected image was created [46]. This ML estimator will be the foundation of the MBSIR algorithm and is based on an algorithm to reconstruct PET data [47]. The algorithm is similar to those successfully used for other spectral imaging sensors and image estimation problems [12,21,35]. However, this estimator is the first developed for reconstructing both the spatial and spectral elements of a spectral image captured with an ETF.

Using a Poisson distribution and looking at one specific point (x_o, y_o, λ_o), the PMF is given by,

$$P[d(x_o, y_o, \lambda_o) = D(x_o, y_o, \lambda_o)] = \frac{i(x_o, y_o, \lambda_o)^{D(x_o, y_o, \lambda_o)}}{D(x_o, y_o, \lambda_o)!} e^{-i(x_o, y_o, \lambda_o)}, \tag{3.6}$$

where $D(x_o, y_o, \lambda_o)$ is a particular realization of random variable $d(x_o, y_o, \lambda_o)$ and $i(x_o, y_o, \lambda_o)$ is the noise free image at one point. Then for all points (x, y, λ), the PMF is,

$$P[d(x, y, \lambda) = D(x, y, \lambda) \forall (x, y, \lambda)] = \prod_{x,y,\lambda} \frac{i(x, y, \lambda)^{D(x,y,\lambda)}}{D(x, y, \lambda)!} e^{-i(x,y,\lambda)}, \tag{3.7}$$

where $D(x, y, \lambda)$ is the collected spectral data cube. A maximum likelihood estimator can be developed by maximizing the PMF with respect to $o(u_o, v_o, \gamma_o)$. The natural

log of the PMF is computed yielding the log likelihood function [49],

$$\ln(P[d(x,y,\lambda) = D(x,y,\lambda)]) = \ln(\prod_{x,y,\lambda} \frac{i(x,y,\lambda)^{D(x,y,\lambda)}}{D(x,y,\lambda)!} e^{-i(x,y,\lambda)}), \tag{3.8}$$

which can be reduced to,

$$\ln(P[d(x,y,\lambda) = D(x,y,\lambda)]) = \sum_{x,y,\lambda} D(x,y,\lambda)\ln(i(x,y,\lambda)) - i(x,y,\lambda) - \ln(D(x,y,\lambda)!). \tag{3.9}$$

Next, the derivative is taken with respect to the true spectral scene at a specific point $(o(u_o, v_o, \gamma_o))$ and is set equal to zero to maximize the log likelihood function. This maximization will also maximize the PMF and an iterative algorithm can be developed [42]. So Equation (3.9) becomes,

$$\sum_{x,y,\lambda} \frac{D(x,y,\lambda)}{i(x,y,\lambda)} \frac{\partial}{\partial o(u_o, v_o, \gamma_o)} i(x,y,\lambda) - \frac{\partial}{\partial o(u_o, v_o, \gamma_o)} i(x,y,\lambda) = 0. \tag{3.10}$$

Using Equation (3.2),

$$\frac{\partial}{\partial o(u_o, v_o, \gamma_o)} i(x,y,\lambda) = h_1(x-u, y-v, \gamma) h_2(\lambda, \gamma), \tag{3.11}$$

Equation (3.10) then becomes,

$$\sum_{x,y,\lambda} \left[\frac{D(x,y,\lambda)}{i(x,y,\lambda)} h_1(x-u, y-v, \gamma) h_2(\lambda, \gamma) - h_1(x-u, y-v, \gamma) h_2(\lambda, \gamma) \right] = 0. \tag{3.12}$$

Finally, some algebraic manipulations are accomplished. First, the second term is moved to the right hand side of the equation,

$$\sum_{x,y,\lambda} \left[\frac{D(x,y,\lambda)}{i(x,y,\lambda)} h_1(x-u, y-v, \gamma) h_2(\lambda, \gamma) \right] = \sum_{x,y,\lambda} \left[h_1(x-u, y-v, \gamma) h_2(\lambda, \gamma) \right]. \tag{3.13}$$

This term is then divided into both sides to yield,

$$\frac{1}{\sum_{x,y,\lambda} h_1(x-u,y-v,\gamma)h_2(\lambda,\gamma)} \sum_{x,y,\lambda} \frac{D(x,y,\lambda)}{i(x,y,\lambda)} h_1(x-u,y-v,\gamma)h_2(\lambda,\gamma) = 1. \quad (3.14)$$

Finally, both sides of the equation are multiplied by the spectral scene at one point. The iteration relation can then be defined as,

$$o^{new}(u_o,v_o,\gamma_o) = \frac{o^{old}(u_o,v_o,\gamma_o)}{\sum_{x,y,\lambda} h_1(x-u,y-v,\gamma)h_2(\lambda,\gamma)} \sum_{x,y,\lambda} \frac{D(x,y,\lambda)}{i^{old}(x,y,\lambda)} h_1(x-u,y-v,\gamma)h_2(\lambda,\gamma). \quad (3.15)$$

where,

$$i^{old}(x,y,\lambda) = \sum_{u,v,\gamma} o^{old}(u,v,\gamma)h_1(x-u,y-v,\gamma)h_2(\lambda,\gamma). \quad (3.16)$$

In Equation (3.15), the new estimate is the old estimate, scaled by the sum of the blurring functions, and multiplied by the image created from the ratio of the data to the old image. After given an initial estimate, the likelihood increases with each step and converges to a maximum likelihood [47].

3.4 Spectral Reconstruction

It will also be useful to have a MBSIR algorithm that only includes the spectral reconstruction part of Equation (3.15), namely the spectral blurring function, h_2. The MBSIR algorithm in Equation (3.15) can be modified to include on the spectral blurring by setting the h_1 transfer function to a delta function. This essentially removes the spatial blurring effects given by h_1 and leads to the spectral reconstruction algorithm,

$$o^{new}(u_o,v_o,\gamma_o) = \frac{o^{old}(u_o,v_o,\gamma_o)}{\sum_{\lambda} h_2(\lambda,\gamma_o)} \sum_{\lambda} \frac{D(x,y,\lambda)}{i^{old}(x,y,\lambda)} h_2(\lambda,\gamma_o), \quad (3.17)$$

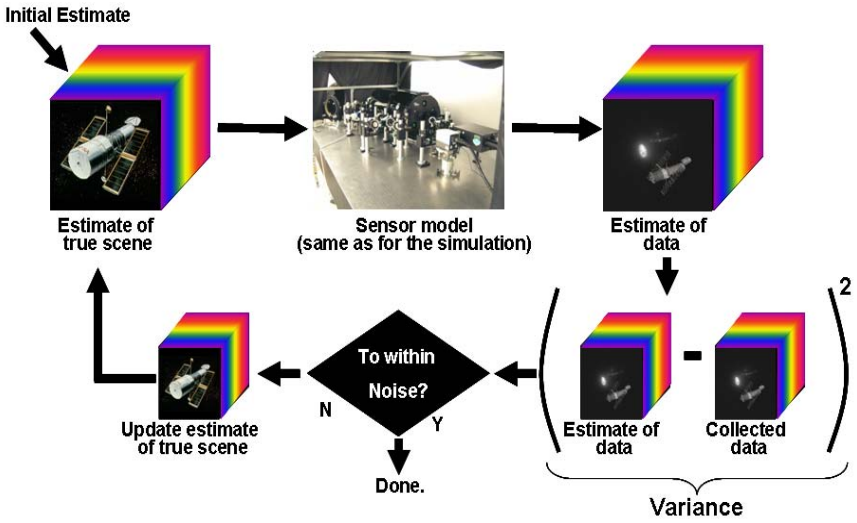

Figure 3.1: Pictorial representation of the MBSIR algorithm.

where,

$$i^{old}(x, y, \lambda) = \sum_{\gamma} o^{old}(u, v, \gamma) h_2(\lambda, \gamma). \tag{3.18}$$

3.5 Reconstructing Spectral Images

Given a model of the sensor defined by the functions h_1 and h_2, and a spectral data cube, the estimator in Equation (3.15) can be used to reduce the spatial and spectral blurring in the data. The initial reconstruction estimate for Equation (3.15) can be a cube of any non-zero values, but is typically a cube of uniform unit value. With this initial guess, the iterations continue until the stopping criteria discussed below is reached. At this point, a balance between the blurring removed and noise amplification is achieved. If more iterations are performed after this point, the noise is further amplified with only minimal blur reduction. Figure 3.1 gives a pictorial description of the algorithm.

3.6 Stopping Criteria

Once given an initial estimate, the MBSIR algorithm iterates until the stopping criteria is met. The stopping criteria occurs when the variance of the reconstruction

noise is the same or lower as the mean of the collected data, or

$$(i(x, y, \lambda) - d(x, y, \lambda))^2 \leq d(x, y, \lambda), \tag{3.19}$$

where the reconstruction noise is the difference between the current estimate of the data and the collected data.

Although not an issue with ASIS, the imaging arrays in ASIR-TB has quantization noise that must be taken into account for the stopping criteria. The ASIR-TB detectors are only 8-bit detectors, allowing only 256 levels for the photons-to-signal conversion. Without this adjustment, the iterations within the algorithm will stop prematurely. This is because the data is perceived to have a lower SNR then it actually has. The detectors for ASIR were measured to determine the effect of the quantization and a factor was derived to correct the stopping criteria for the ASIR-TB data.

3.7 Summary

This chapter develops the MBSIR algorithm to reduce the blurring in spectral images collected by ETF systems. The algorithm is based on other statistical reconstruction algorithms and starts with an understanding of the noise statistics of the sensor. The MBSIR algorithm is the first method developed to reduce both the spatial and spectral blurring in ETF spectral imaging systems.

The algorithm starts with a guess for the true spectral scene, and then iterates until a balance between the blurring removed and noise amplification is achieved. While the MBSIR algorithm is applicable to any ETF system, it will be used with data collected with ASIS and the test sensor, ASIR-TB.

IV. Models

As Figure 3.1 shows, the critical component to the MBSIR algorithm is the model of the spectral imaging sensor. Based on experience working with the MBSIR algorithm, the algorithm will not improve the resolution without an accurate model. While the algorithm is derived for any ETF system, a specific system must be modeled to demonstrate the performance of the algorithm.

This chapter will describe the models for two different sensors used in this research, ASIS and ASIR-TB. Both of these sensors use a LCTF type of ETF. For ASIS, two versions of the sensor have been modeled. A first order model was developed based on an initial design to simulate the performance of the sensor and the MBSIR algorithm. As the sensor was further refined, a second order model was developed. This chapter will begin by describing the components of ASIS and then will develop of the first order model. The second order model will be developed next and is followed by a discussion of the model differences. The ASIR-TB sensor is then described and modeled. The chapter concludes with a discussion of the connection between the filter sampling and the reconstruction sampling when using the MBSIR algorithm.

4.1 AEOS Spectral Imaging Sensor

ASIS is composed of five distinct sub-systems. These sub-systems include the AEOS telescope, adaptive optics for wavefront correction, sensor optics needed for creating an image, LCTFs for wavelength selection and finally a detector for converting photons to signal. Each of these areas is discussed in the following sections and are combined together to form the sensor models needed for the MBSIR algorithm.

4.1.1 AEOS. The AEOS telescope, shown in Figure 4.1, is the entrance aperture to ASIS. The telescope has a large 3.6m primary mirror partially obscured by a 72cm central obscuration. The optics of the AEOS telescope create a f/200 ray bundle that follows a Coude path around the telescope mount to a Coude room containing the adaptive optics bench. A pupil relay demagnifies the telescope entrance

pupil to present a 4" ray bundle to the experiment room containing the bench optics for ASIS [26].

4.1.2 Adaptive Optics. The AO system consists of a tracker, a wave-front sensor (WFS), real-time reconstructor (RTR) hardware, servo loop compensation, and a deformable mirror (DM) [9]. While using the AO system leads to higher spatial resolution imagery, it comes at a cost. Approximately half of the light in the visible wavelengths is split off for the WFS and tracker in the AO system. This reduces the amount of light available for imaging. However, using AO substantially increases the peak irradiance at the detector, typically resulting in a higher SNR and a fainter visual magnitude capability [26].

4.1.3 Sensor Optics. The AEOS telescope directs light to an experiment room via a rotating flat mirror. A 16"commercially available Ritchey-Chretien input telescope is utilized in an off-axis configuration in conjunction with a third concave mirror to yield a 5X all-reflective pupil reduction with approximately a 20mm diameter exit pupil. The collimated ray bundle is then folded and de-rotated by a custom designed 3-mirror K-mirror rotation assembly. After de-rotation, the beam path is separated into two channels using a dichroic beam splitter that reflects 400nm to 950 nm light and transmits light 950 nm and above. The reflected visible to near-IR light (400-950nm) is passed through a pair of counter rotating dispersion prisms that provide compensation for the differential bending of light at different wavelengths that results from the atmosphere. Finally, the visible to near-IR path is split into two channels using a dichroic beam splitter. [26]. Figure 4.2 is a picture of ASIS showing the optical elements.

4.1.4 LCTF. Due to stringent imaging requirements, LCTFs are used in ASIS for the spectral wavelength selection. The CRI VariSpec^{TM} LCTFs were chosen because of the filters have no mechanical parts, fast switching times, and are easily integrated into the optics of the sensor.

Figure 4.1: The Advanced Electro-Optical System (AEOS). AEOS is the entrance aperture for ASIS.

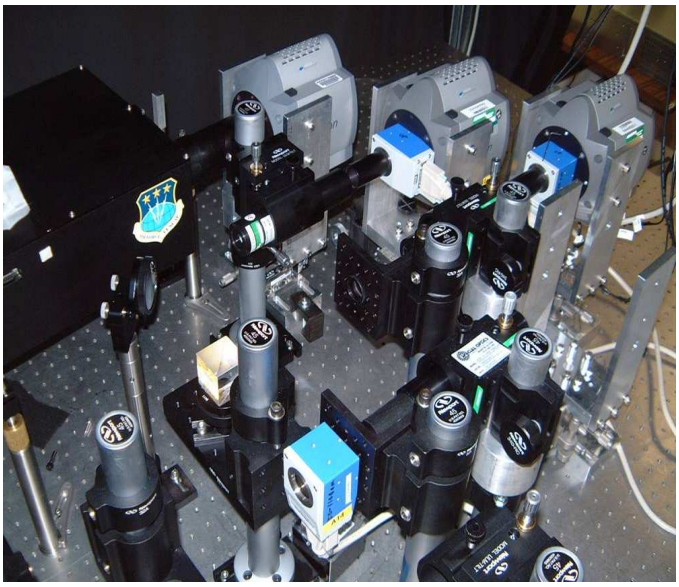

Figure 4.2: Picture of the ASIS optics after the AO bench. The two cameras to the right of the picture are the ASIS visible imaging channels. The blue cubes attached to the cameras are the visible LCTFs. The additional LCTF at the bottom of the picture is the NIR LCTF.

Two types of LCTFs are currently used for wavelength selection for ASIS and a third will be added in the future. These filters have been shown in many circumstances to provide good quality spectral images [24, 36, 37]. The first is a VIS filter, operating between 400nm and 720nm with a center wavelength selectable to an accuracy of <1nm and a 20nm bandwidth measured at 550nm. The second is a NIR filter, operating from 650nm to 1100nm with a center wavelength selectable to <1nm accuracy and a 10nm bandwidth measured at 850nm. The third filter is a SWIR filter that is not currently installed. The SWIR filter is planned to operate between 1μm and 2.3μm with a 20nm bandwidth.

As seen in Fig 4.3, the transmission levels through the filters are relatively low and vary with the selected center wavelength. The very low transmission in the blue spectrum (400nm - 450nm) may prove this portion unusable for dim to moderately illuminated objects. As with the transmission, the bandwidth of the filter is proportional to the selected center wavelength, being narrower at shorter wavelengths and wider at longer wavelengths.

The LCTFs are several stages of similar Lyot cells. Each cell consists of a linear polarizer, a liquid crystal sheet used to introduce a variable retardance, and a fixed retarder, where the thickness of the fixed retarders of successive cells increases in size [36]. The filter's passband is tuned by applying a set retardance to each cell which introduces a phase delay that destructively interferes light outside a small bandwidth. Multiple cells are needed in each filter to achieve the range of wavelength selection and bandwidth desired [18].

One of the challenges in using a LCTF is overcoming the filter's inherent polarization. The LCTFs have a series of aligned linear polarizers within the filter that linearly polarizes the incoming light. This presents a spectral radiometry problem when the LCTFs are used to spectrally image a satellite. The materials on a satellite will polarize the randomly polarized sunlight. The optical elements of ASIS will alter the polarization of polarized light, making it difficult to determine the light's original linear polarization. Using only a single LCTF, an unknown number of photons of the orthogonal polarization will be lost. Without an precise photon count, it is not possible to accurately determine the spectra of the object.

A sensor design can overcome this problem. A second filter in the same band was placed so that the polarizers are orthogonal to the polarizers in the original filer. The filters were placed in separate optical paths behind a polarization beam splitting (PBS) cube [36]. A custom PBS cube was designed to precisely match the optical thickness and dispersion characteristic of the LCTF for which the intermediate imaging lens had been originally optimized [26]. The two LCTFs are rotated so the orthogonal linear polarizations match the PBS cube output states and are mounted between the final relay and the sensor detector. By precisely synchronizing the integration time of the two sensors, the contributions of the two orthogonal polarization states can be imaged. All photons reflected from the satellite can now be accounted for by summing the images.

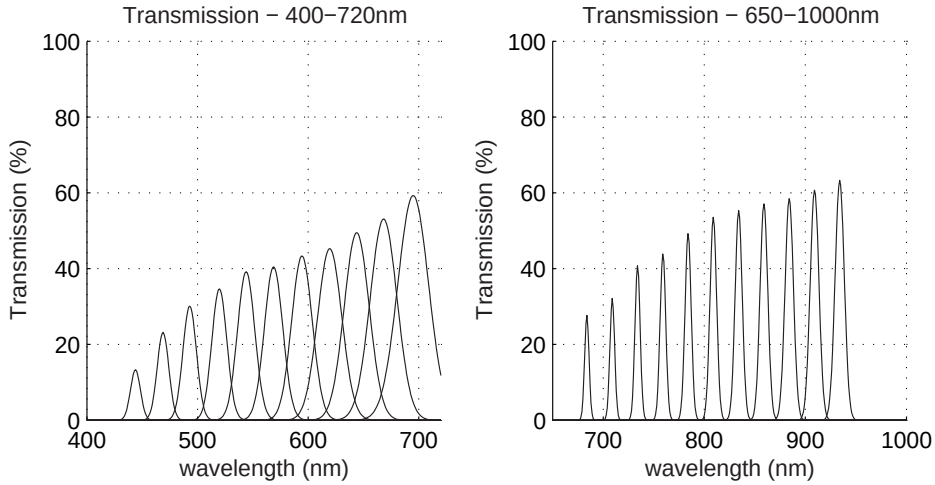

Figure 4.3: Samples of typical transmission vs. wavelength (nm) output of the VIS and NIR ASIS LCTFs. The passbands shown represent a tenth of the possible filters passbands.

Table 4.1: Andor iXon DV887 Parameters. [6]

Parameter	Value
Active Pixels	512x512
Pixel Width (WxH; μm)	16x16
Image Area (mm)	8.2x8.2
Active Area pixel well depth (e^-; typical)	220,000
Gain Register pixel well depth (e^-; typical)	800,000
Max Readout Rate (MHz)	10
Frame Rate (frames per second)	32 to several 100's
Read Noise (e^-)	<1 to 62 at 10MHz

4.1.5 Imaging System. The imaging system for each channel consists of an Andor Technology iXon DV887 camera operating at -60^oC. This advanced camera has a back illuminated electron multiplying charge coupled device (EMCCD) for single photon counting capability. The camera achieves a maximum Quantum Efficiency (QE) of 92.5% at 0.575μm and has maximum flexibility in the readout of the 512x512, 16μm pixels in the CCD array through both binning and multiple read-out rates. The camera also can operate with extremely low noise, from $\leq 1e^-$ to $62e^-$ of read noise [6]. The high QEs and the low read noise in this camera make it a good choice to mitigate the low transmission rates of the LCTFs. Table 4.1 gives the key parameters of the cameras used for ASIS and Fig 4.4 gives the QE for the camera.

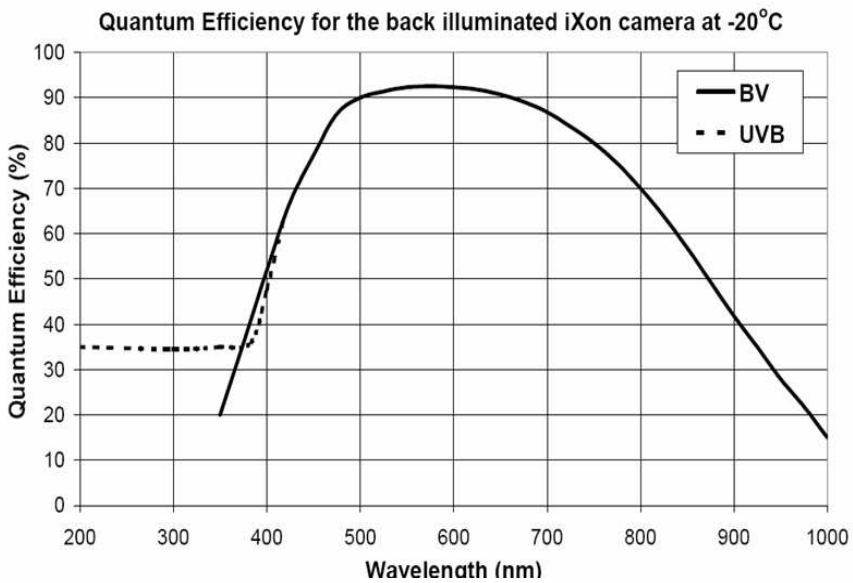

Figure 4.4: QE of the iXon DV887 camera. The BV curve is the QE for the standard back-illuminated device. The UVB is the QE for the back-illuminated device with a UV coating [6].

4.2 First-Order ASIS Model for MBSIR

All of the five components described in the previous section and the atmosphere were used to create the first-order model of ASIS. This early model was created while ASIS was still being constructed and uses a summation of predicted models of the ASIS's individual components. The second-order model replaces some of the individual component models with a measured sensor spectral response.

Both the first and second order models for the sensor are broken down into three sub-models: 1) a sub-model that describes the spatial blurring in the sensor, 2) one describing the spectral blurring and 3) one that describes the spectral radiometry (the spectral photon losses). The first sub-model is described in the h_1 function, while the second and third sub-models are given by the h_2 function in Equation (3.15). In both of the models, only the diffraction caused by the AEOS aperture causes any spatial blurring (although other affects can be added, such as known sensor abberations or estimated atmospheric blurring) and spectral blurring is caused only by the LCTFs. However, all of the elements in ASIS contribute to the spectral radiometry sub-model.

For some of the optical elements, such as the dichroics, there are different spectral transmissions for the orthogonal polarizations.

The first-order model for ASIS is designed to be as flexible as possible. While much of the data used to derive the model is given for specific wavelengths, the model is designed to interpolate values for wavelengths where no truth data is provided. This is done in one of three ways. The first is the derivation of analytic equations for the response of the element, or collection of elements, for any given wavelength. The second is the creation of a high-degree polynomial fit to known spectral response data. The final way is a high resolution look-up table of transmission values. Each is done to minimize the overall error in the model.

4.2.1 Atmosphere. The first-order model will assume that all spatial blurring due to atmospheric turbulence will be corrected for with the AO system. Also, the first-order ASIS model will assume the spectral transmission of the atmosphere is 100%.

4.2.2 AEOS. The AEOS system contributes to both the spatial blurring and the spectral radiometry of ASIS. The spatial blurring is based on the optical transfer function (OTF) of the AEOS aperture. The OTF can be computed from the aperture based on the well known relation [19],

$$OTF(f_x, f_y, \lambda) = P(x, y, \lambda) \oplus P(x, y, \lambda) \mid_{f_x = \lambda z_i x, f_y = \lambda z_i y}, \tag{4.1}$$

which states the $OTF(x, y, \lambda)$ is the autocorrelation ($\oplus$) of the pupil, $P(x, y, \lambda)$. Since the scaling for the OTF is dependent on the wavelength, there will be a different OTF for each wavelength. For ASIS, the pupil is the AEOS entrance aperture and consists of a primary mirror with the obscuration. The cross-section of the OTF at 500nm is shown in Figure 4.5.

In addition to the spatial blurring described by the OTF, the AEOS mirrors and Coude window effect the spectral radiometry. The primary mirror is coated

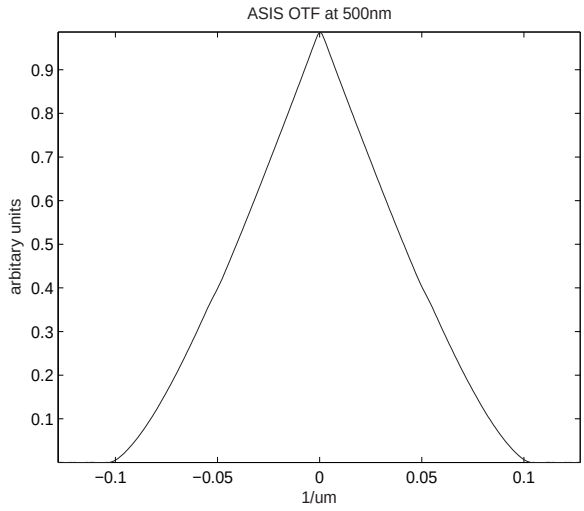

Figure 4.5: The Optical Transfer Function of ASIS at 500nm.

with aluminum and the secondary, tertiary, and four additional Coude mirrors are coated with protected silver. The Coude window has a flat spectral transmission of approximately 97% for 400-2300nm. Figure 4.6 shows the modeled spectral reflectance versus the given data for the aluminum and protected silver mirrors.

4.2.3 Adaptive Optics. The adaptive optics is an extremely complex system and is not modeled component by component. However, if the AO system is performing well, it effectively cancels out most atmospheric blurring. The components of the AO system do substantially contribute to the spectral radiometry modeling of ASIS. The AO system has 11 protected silver mirrors and the 50/50 dichroic. Figure 4.7 shows the modeled spectral transmission versus the given data for the 50/50 dichroic.

4.2.4 Sensor Optics. The sensor optics has nine protected silver mirrors for the visible light and ten for the near-IR. Included in these mirrors are the reduction telescope, the de-rotator and several turning flats. Also, the sensor optics includes two dichroic elements for wavelength separation. Figure 4.8 shows the spectral transmission for the ASIS dichroics. Modeling the SWIR and VIS/NIR dichroics with the same method as the other ASIS elements (the polynomial fitting method) is especially

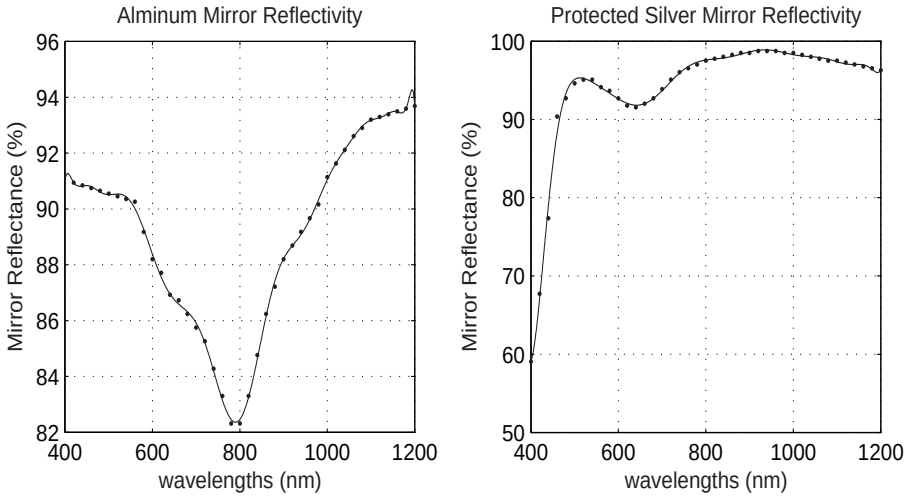

Figure 4.6: Model of the Aluminium and Protected Silver mirrors used in ASIS. The points represent the given data and the solid line the model.

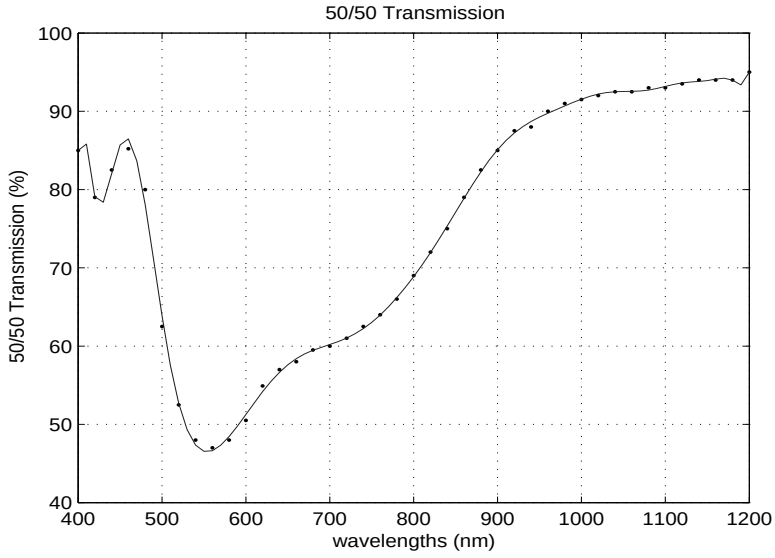

Figure 4.7: Model of the 50/50 dichroic used for the AO system in ASIS. The points represent the given data and the solid line the model.

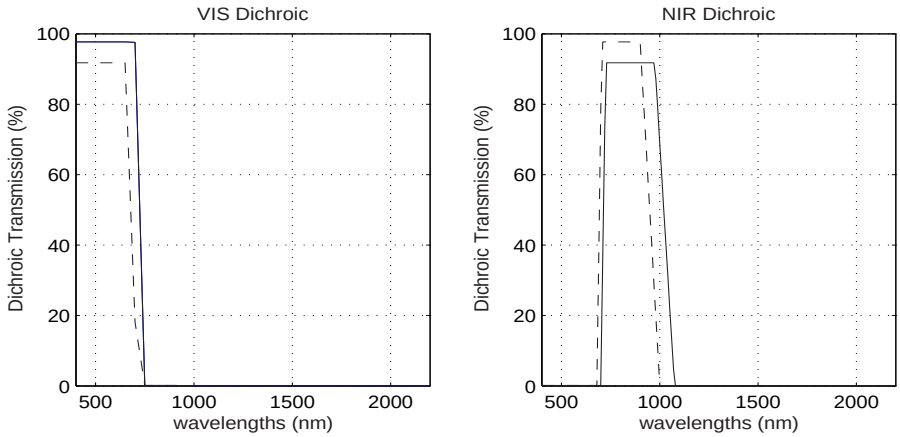

Figure 4.8: Model of the VIS/NIR and NIR/SWIR dichroics used in ASIS. The solid line is the S polarization, the dashed line is the P polarization.

difficult. The sharp cut-offs did not lend itself to this method. Therefore the dichroic model is a look-up table of values at a 0.1nm sampling.

The optical elements for the atmospheric dispersion corrector, imaging lenses and relays have many different types of coatings. Figure 4.9 shows the modeled spectral transmission versus given data for these coatings.

4.2.5 LCTFs. The LCTFs are the only spectral blurring element and form the basis for the SMF. The transmission through the LCTFs is modeled as a Gaussian curve. The maximum transmission and bandwidth are derived from provided truth data. These values are then used to construct a Gaussian profile corresponding to the filter transmission for any filter setting. Figure 4.10 shows a model LCTF transmission versus the manufacture provided data for the LCTF.

4.2.6 Imaging System. The imaging system is a high gain/low noise camera. For this camera, the QE curve is part of the spectral radiometry and is modeled. Figure 4.11 gives the modeled QE of the camera versus given data.

4.2.7 Overall First-Order Model. Combining all of these elements together gives the first-order model of the ASIS sensor. Figures 4.12 and 4.13 show the overall first-order model of the spectral transmission of ASIS in the visible and near-IR

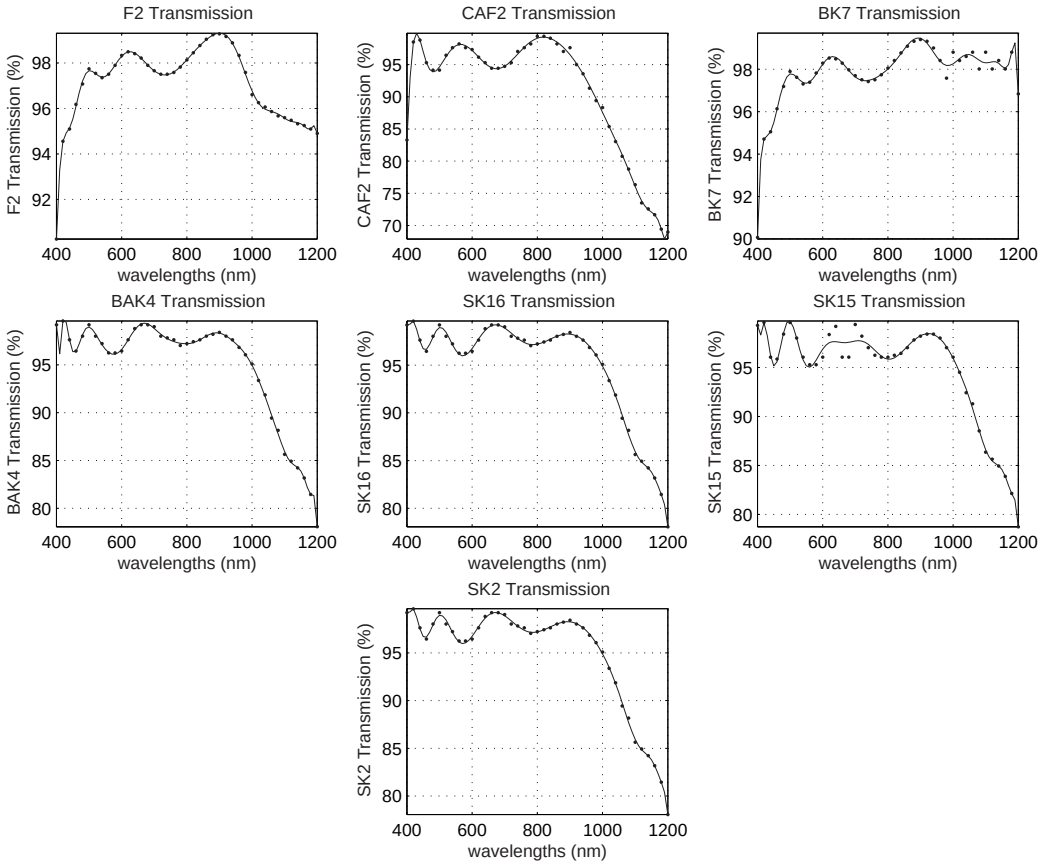

Figure 4.9: Model of the various coatings used in ASIS. The different coating include BK7, BAK 4, CAF2, F2, SK2, SK15 and SK16. The points represent the given data and the solid line the model.

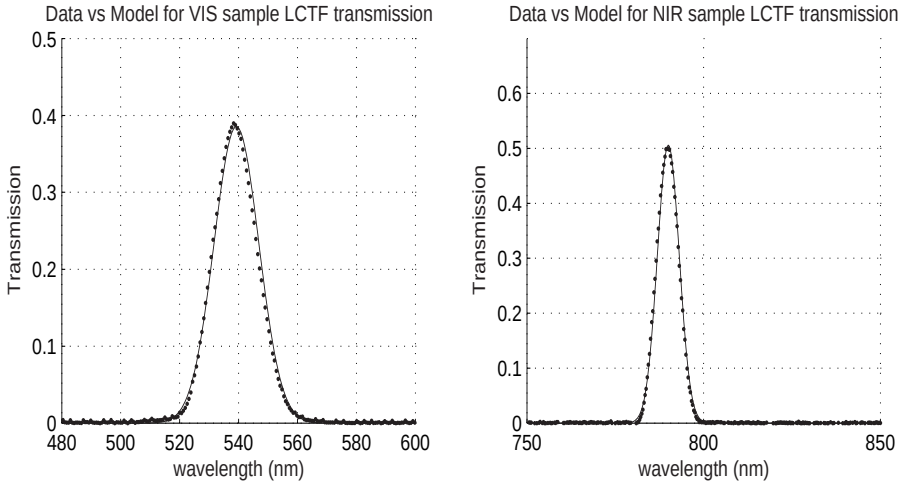

Figure 4.10: Model of one transmission profile of the VIS and NIR ASIS LCTFs. The points represent the given data and the solid line the model.

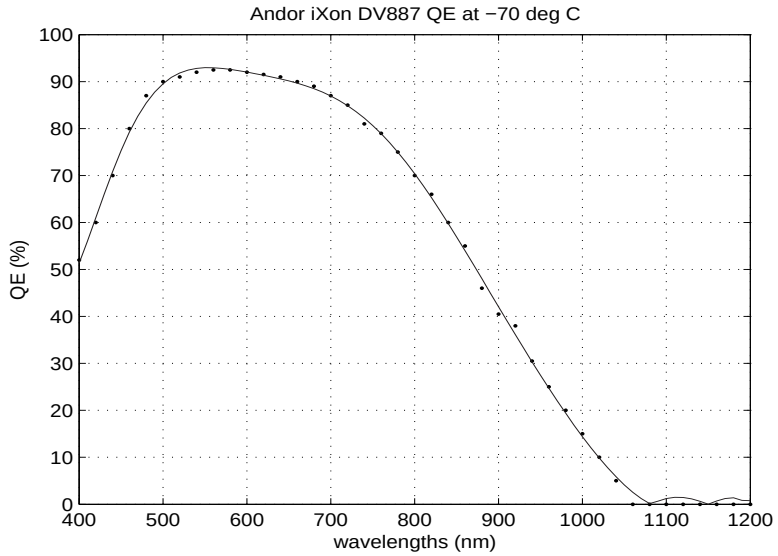

Figure 4.11: Model of the ASIS camera. The points represent the given data and the solid line the model.

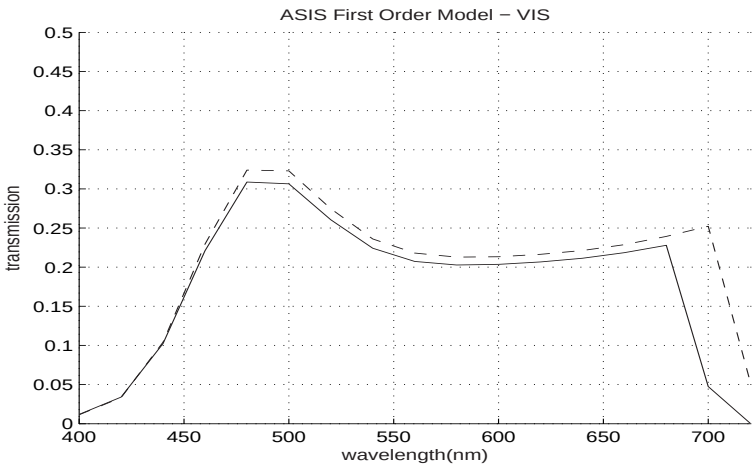

Figure 4.12: Spectral transmission of the first-order ASIS model in the visible without the LCTFs. The solid lines represent the P polarization, while the dashed lines are the S polarization.

without including the LCTFs. In the figures, the S and P polarizations refer to the orthogonal vertical and horizontal polarization states. As Figure 4.14 shows this model has a reasonably close match to the best available truth data for the spectral radiometry of the sensor. As Figure 4.14 shows, the model has an average maximum error of less than 3% in the visible to near-IR range.

4.3 Second-Order ASIS Model

After ASIS was fully constructed, several calibration measurements were taken to determine the actual sensor response. Additionally, the atmospheric transmission effects were taken into account by simulating the conditions at the MSSC. Both of these steps were accomplished to create a second-order model of the sensor. Since the visible channels is the only fully operational channel, containing the dual filter/array sub-channels for polarization collection, the calibration measurements were made for the visible only. Similar measurements will be made for the NIR when the full NIR channel is completed. Until the NIR measurements are made, the first order model for the optical components in the NIR will be used.

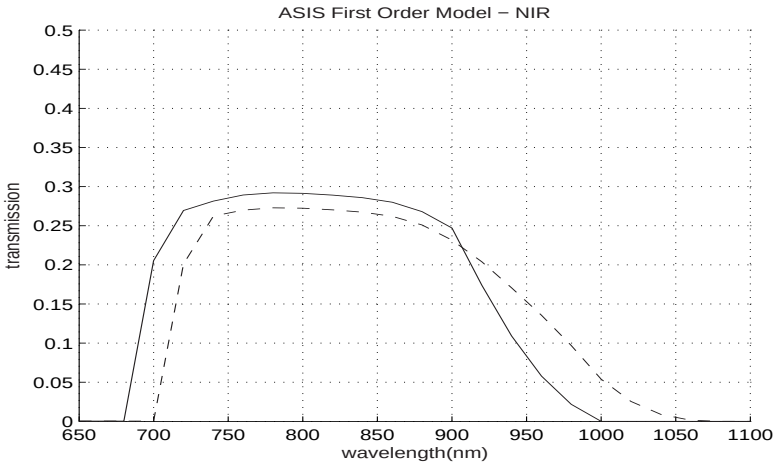

Figure 4.13: Spectral transmission of the first-order ASIS model in the near-IR without the LCTFs. The solid lines represent the P polarization, while the dashed lines are the S polarization.

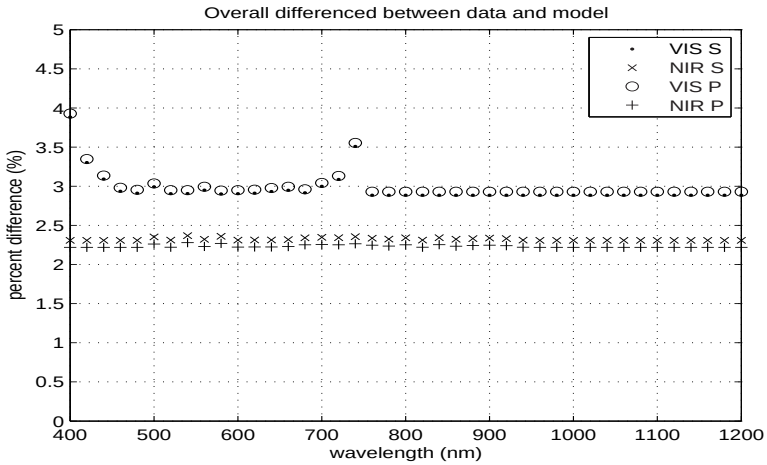

Figure 4.14: Overall model error in the spectral radiometry of the ASIS model.

The measurements changed the modeling of the AO system and sensor optics. Instead of using the individual optical element transmission and reflection values, the measured total spectral response is used. The LCTF model uses the results of calibration measurements instead the measured data provided by the manufacturer. Because actual spectral response measurements are used, the sampling resolution of the second-order model is limited to the spectral resolution of the measurements, which is 1nm.

4.3.1 Atmosphere. The transmission losses associated with the atmosphere are implemented in the second-order ASIS model through the atmospheric simulator in the High Energy Laser End-to-End Operational Simulator (HELEEOS) software. HELEEOS is an AFIT developed simulation for high energy laser propagation through the atmosphere. Part of the HELEEOS software includes an atmospheric simulation that provides atmospheric transmission losses for a variety of elevations, ranges and environmental conditions. For the second-order model, an elevation of 10,000 ft is used in a tropical summer environment for the typical conditions at the MSSC. Figure 4.15 gives the output of the HELEEOS atmospheric simulation for the visible to the near-IR. Spatially, the AO system is still assumed to correct any spatial blurring due to the atmospheric turbulence.

4.3.2 AEOS. Calibrating the spectral response of the AEOS system is difficult due to the location and size system of the entrance aperture. Therefore, the results of the first-order model will be carried forward unchanged for the second-order model.

4.3.3 Adaptive Optics. The calibration of the AO and other sensor optics was accomplished by using an Integrating Sphere (IS) placed in two locations within the ASIS path. By taking the difference of the data collected in the two locations, the spectral response was determined. Using this method two sets of calibrated spectral response were calculated. The first spectral response is for the optics in the AO

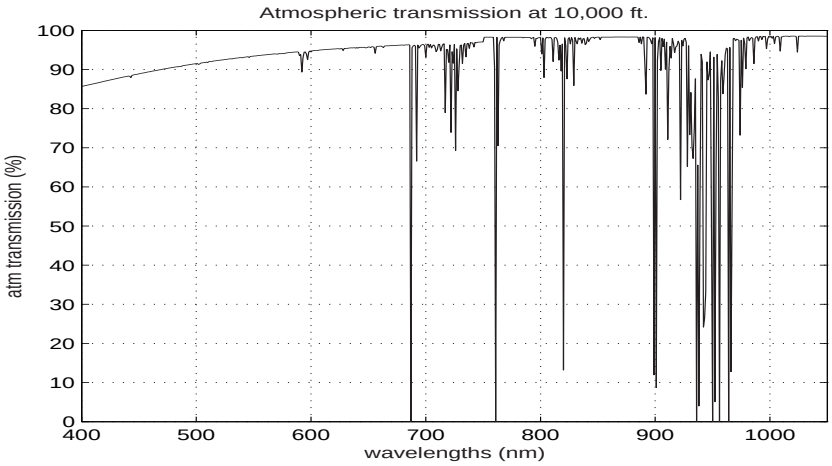

Figure 4.15: Typical atmospheric transmission profile for a summer tropical environment at a 10,000' altitude using the HELEEOS atmospheric simulation.

system. For this measurement, the IS was placed just before and then just after the AO bench. Figure 4.16 shows the calculated spectral response for the AO system. Both the S and P polarizations were collected to measure the different polarization dependent spectral responses.

4.3.4 Sensor Optics. The second spectral response is for the rest of the optics in ASIS. The integrating sphere was placed in front of the optics after the AO system and then just after these optics. Again, the difference was taken between these two measurements to calculate the spectral response for the ASIS optics shown in Figure 4.17. Again, both the S and P polarizations were collected to measure the different polarization dependent spectral responses.

4.3.5 LCTF Calibration. The transmission values for different filter center wavelengths were measured using a Varian Cary 5000 UV-Vis-NIR Spectrophotometer. The results of these measurements were used in the second-order model for ASIS.

Several different calibration measurements were taken for the visible wavelengths. The Cary 5000 uses a grating spectrometer to measure the spectral transmission of the filters, so the spectral light is polarized. Therefore, the P and S polarizations need to be collected independently for each calibration measurement to ensure

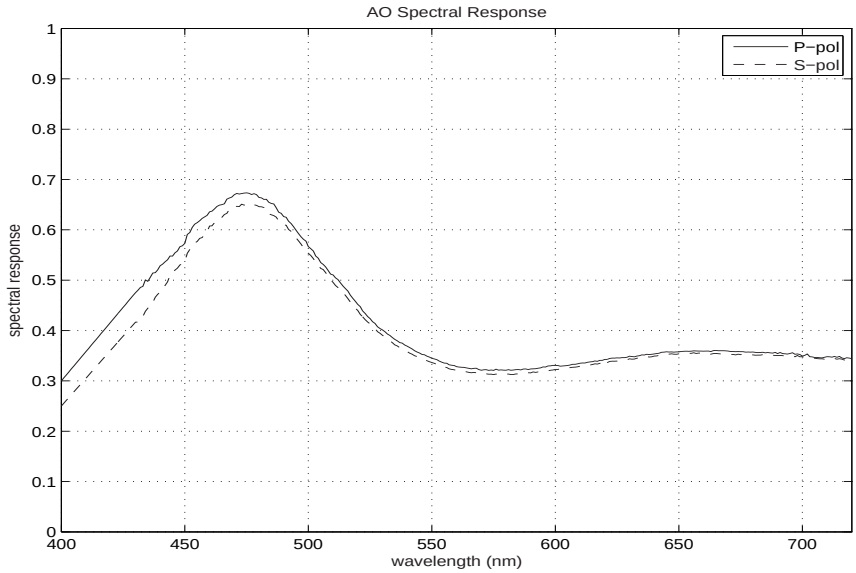

Figure 4.16: Measured spectral response of the adaptive optics system in the visible [26].

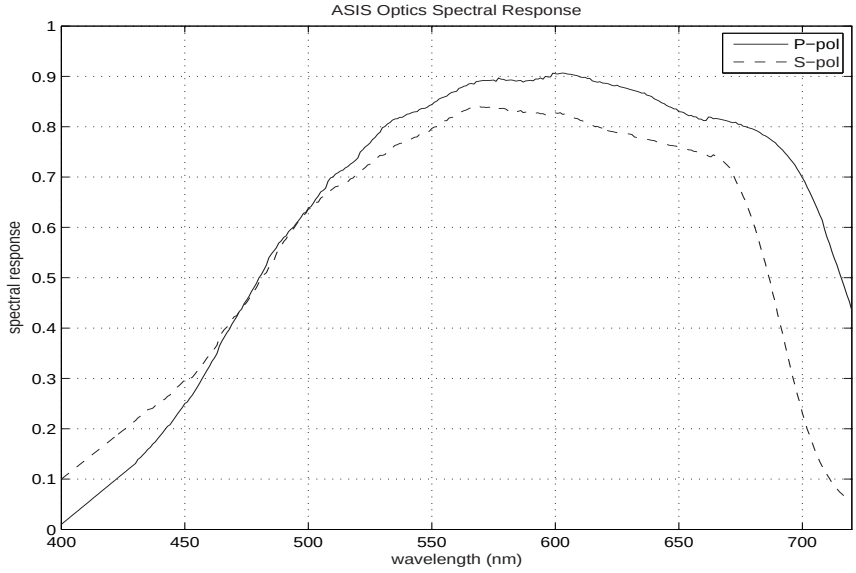

Figure 4.17: Measured spectral response of the ASIS optical components in the visible [26].

that the full spectral response of the filter was captured. Three scans were collected to measure the repeatability of the spectral transmission, based on a 1nm scan across the range of the filter. For both the VIS filter 50845 and 50928, the transmission was repeatable to less than 1% difference. Scans were also completed at higher 0.1nm and 0.5nm resolutions to obtain an average spectral throughput for the LCTF model.

The temperature dependence of the filters was also measured. The 1nm filter scans were repeated with the 50845 filter 11^{o}C and the 50928 filter 12^{o}C higher than the previous scans. The elevated temperature affected the amplitude of the peak transmission, but did not substantially alter the bandwidth. For the 50845 filter the mean peak transmission was 15.5% higher while the bandwidth was 0.76% lower. For the 50928 filter, the transmission was 18% higher and the bandwidth was 0.035% higher. Because of the increase in the peak transmission, the LCTFs must be re-measured for the operating temperature of the filters is changed.

4.3.6 Imaging System. The imaging arrays were not calibrated for the second-order model. The first-order model will be carried forward for use in the second-order model.

4.3.7 Overall Second Order Model. The elements in this section were combined to give the second order model of ASIS. Figure 4.18 shows the overall second-order model transmission of ASIS.

4.4 First- and Second-Order ASIS Model Comparison

Figure 4.19 shows how the combination of the measured elements has changed the model of ASIS. The figure shows the difference between the overall first and second-order spectral transmission models without the LCTFs. The difference between the models average 3% across the visible range. The most significant change is due to the addition of the spectral atmospheric effects. The model differences are

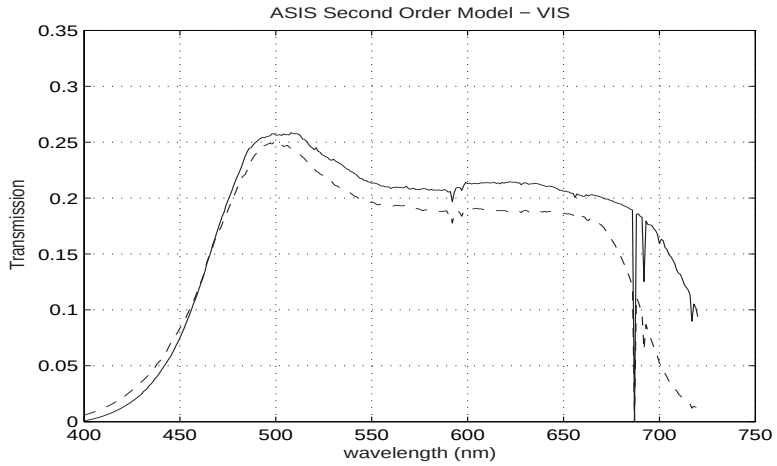

Figure 4.18: Spectral transmission of the second-order ASIS model in the visible without the LCTFs. The solid lines represent the P polarization, while the dashed lines are the S polarization.

larger near the atmospheric absorption line just below 700nm and at the dichroic at 700nm.

Figures 4.20 and 4.21 show the difference of the peak transmission and the bandwidth between the given data for the visible LCTFs and measured values. The average difference in the peak transmission is 13% and 7% of filters 50845 and 50928. The average difference in the bandwidth is 2.5% and 1%.

4.5 AFIT Spectral Image Reconstruction Test Bench

As mentioned previously, the ASIR-TB sensor is similar to ASIS, but is less complicated, cheaper, and does not require scheduling to use. From a modeling perspective, the two sensors share many of the same elements. ASIR-TB has three basic subsystems as compared to six for ASIS. The basic ASIR-TB subsystems include the sensor optics, filters for wavelength selection and a imaging array, while those for ASIS add the atmosphere, AEOS, and the adaptive optics.

In the ASIS data collections, diffraction of the aperture was the only assumed spatial blurring in the collected images. Using diffraction is not practical for ASIR-TB

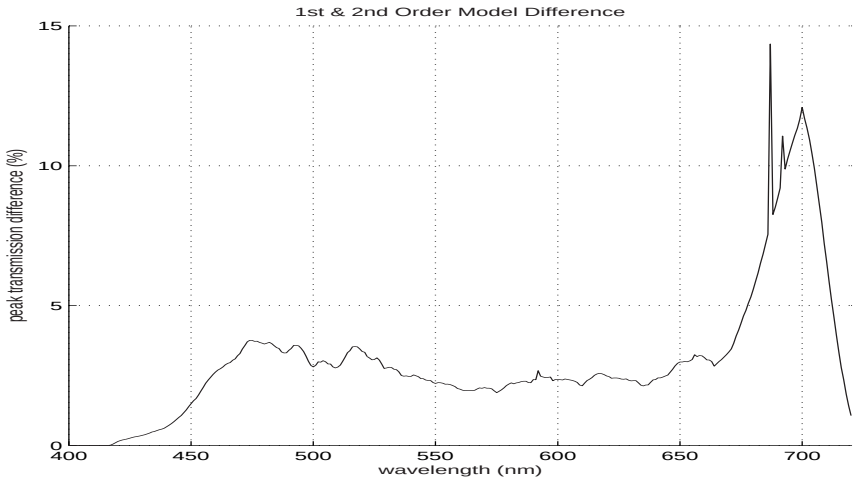

Figure 4.19: Overall model differences in peak spectral transmission of the ASIS first- and second-order models without the LCTFs.

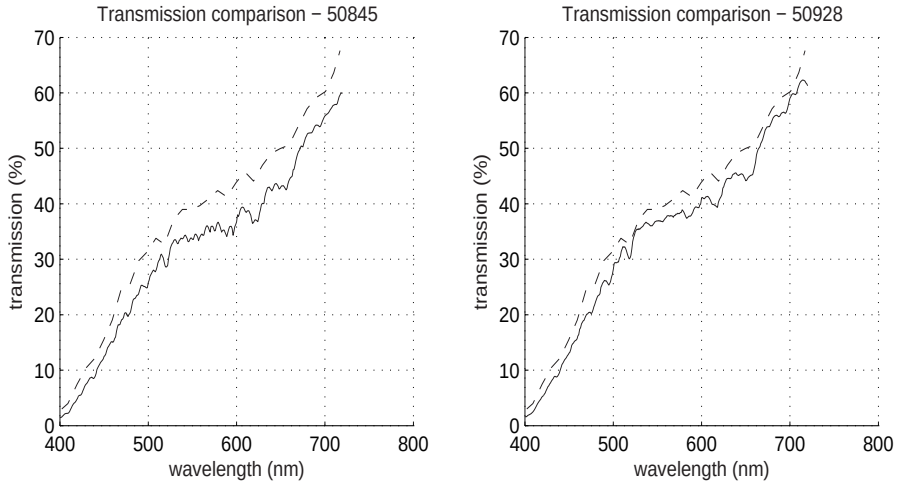

Figure 4.20: Difference between the given and the measured peak transmission for the visible LCTFs. The solid line is the measured data, while the dashed line is the given values.

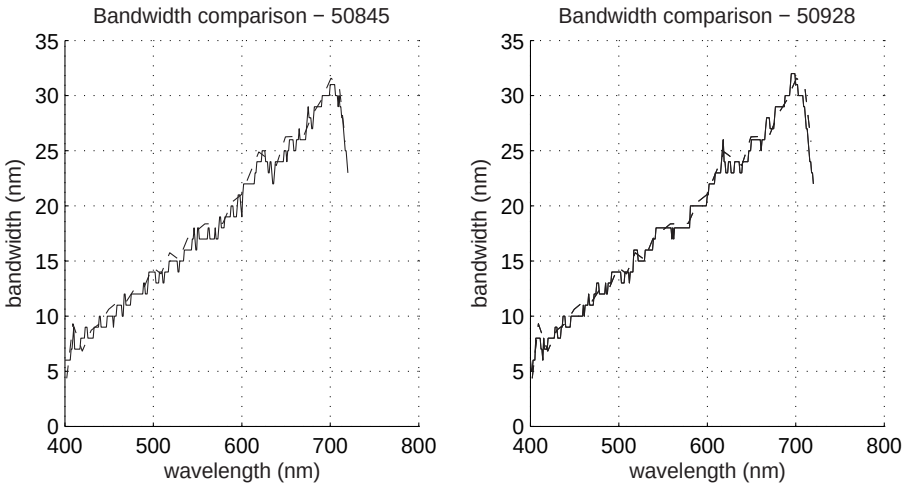

Figure 4.21: Difference between the given and the measured bandwidth for the visible LCTFs. The solid line is the measured data, while the dashed line is the given values.

Table 4.2: ASIS and ASIR-TB Model Comparison.

	ASIS	ASIR-TB
Atmosphere	Spectral Trans.	None
AEOS (Spatial blurring)	Diffraction	Focus Error
Adaptive Optics	Spectral Trans.	None
Sensor Optics	Spectral Trans.	Spectral Trans.
LCTFs	Yes	Yes
Imaging Array	Si	CMOS

given the sizes of the lenses and distance limitations. Instead, for ASIR-TB, a known defocus will be used to spatially blur the two filaments of the sources.

The main element that both ASIS and ASIR-TB share are the filters for selecting the spectral wavelength to image. Both sensors use the same LCTFs as the spectral selection element. Table 4.2 provides a comparison the model elements of ASIS and ASIR-TB.

4.5.1 Sensor Optics. ASIR-TB has three lenses all of which have a diameter of 2.54cm and have a BK7 coating. The initial lens has a focal length of 7.56cm. With the source placed 45cm in front of this lens, this lens forms an image of the source 9cm behind the lens, with the image reduced in magnification 5 times. Located 50cm

behind this intermediate image plane is a 50cm focal length lens which serves to collimate the image. After this collimating lens is a 5.02cm focal length imaging lens which takes the incoming collimated light and forms an image on the imaging array. The combination of the second and third lenses provide a further 10 times reduction in the image size of the source. The complete system offers a 50 times demagnification of the source image.

4.5.2 LCTF. Placed in the collimated space between the second and third lenses is the same VIS and NIR CRI VariSpec^{TM} LCTF used for wavelength selection in ASIS. ASIR-TB will only collected randomly polarized sources so dual orthogonal polarization channels are not needed.

4.5.3 Imaging System. Located behind the third lens is are two different imaging arrays. The first is a SUMIX SMX-110 Complementary Metal Oxide Semiconductor (CMOS) imaging array used to collect the image of the source after passing through the LCTFs with the visible filter. For the NIR filter, a Lumenera Lu-105 CMOS imaging array is used as this higher quality camera became available for the NIR collections. While these simple arrays are not low noise, they are sufficient for collecting the spectral image cube for the MBSIR algorithm since the signal level is controllable. Both arrays are 1.3 megapixel and have 7.5μm pixels for the SMX-110 and 5.2μm pixels for the Lu-105. Both arrays are capable of multiple read out rates and binning to most effectively record the ASIR-TB data. No QE curve was given for the SMX-110, so a generic CMOS QE curve was assumed and is shown in Figure 4.22. The QE curve for the Lu-105 was provided and is given in Figure 4.23.

4.6 ASIR-TB Model

To apply the MBSIR algorithm, a model of ASIR-TB must be created. The parts of the ASIR-TB model are similar to those of ASIS, except that ASIR-TB does not include any atmospheric effect or adaptive optics.

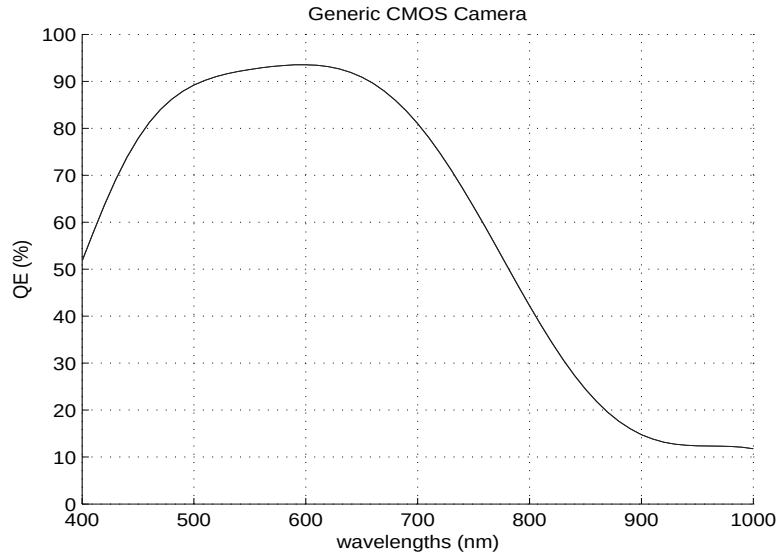

Figure 4.22: QE of a generic CMOS imaging array [31].

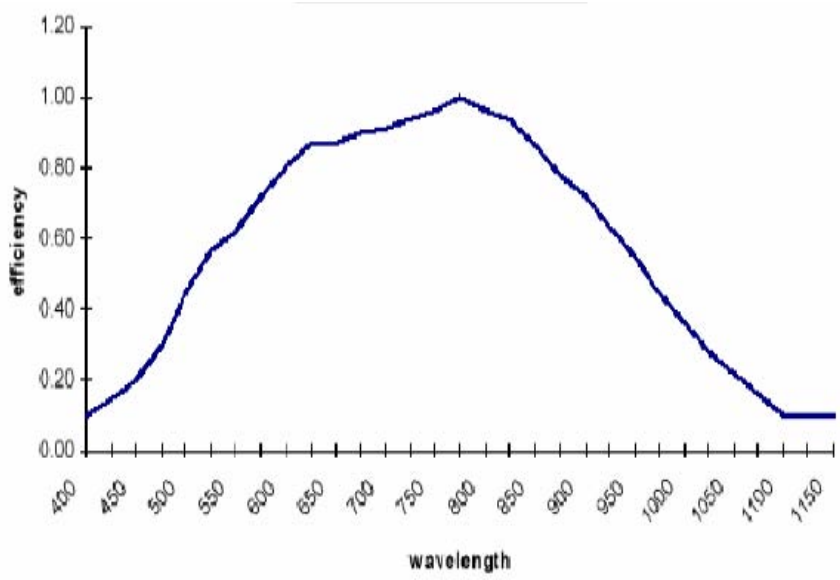

Figure 4.23: QE of the Lumenera Lu-105 imaging array [2].

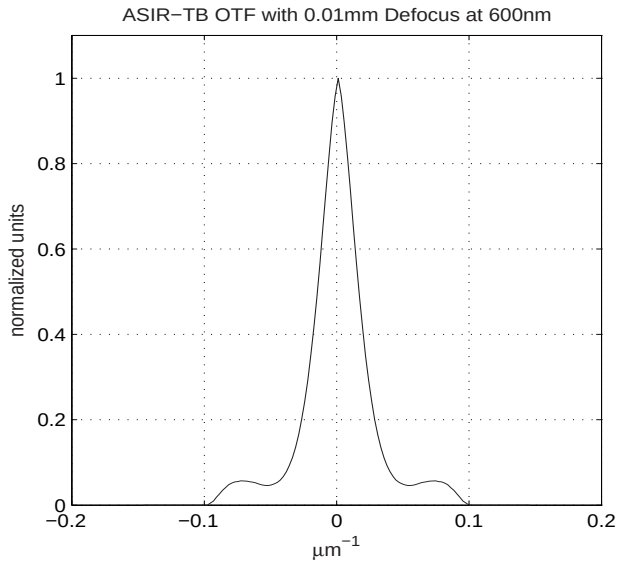

Figure 4.24: The cross-section of the OTF for ASIR-TB with a 0.01mm induced focus error at a wavelength of 600nm.

4.6.1 AEOS (Spatial Blurring). While ASIR-TB does not use AEOS as its entrance aperture, an abberation is introduced to spatially blur the blubs of the source. For ASIR-TB, this abberation is a known focus error. The focus error is created by intentionally defocusing the imaging array. The abberation is described by placing the phase corresponding to the focus error in the description of the entrance aperture. For ASIR-TB, the entrance aperture is the first lens in the optical path. Figure 4.24 shows the OTF corresponding to the phase of the focus error.

4.6.2 Sensor Optics. The sensor optics for ASIR-TB is modeled by looking at the spectral transmission of the coating on the three lenses in the sensor. While the spectral transmission does not contribute to the spatial or spectral blurring, it does go into the third part of the model describing the spectral transmission. Since all of the lenses have the same BK7 coating, the spectral transmission of the sensor optics will be the transmission of six BK7 coatings, or one coating for each side of the three leses. Figure 4.25 shows the modeled transmission of the six BK7 coatings.

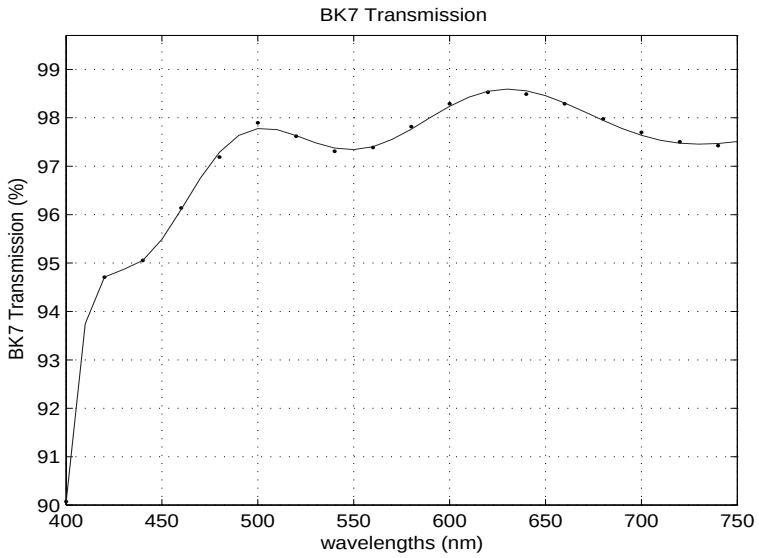

Figure 4.25: Spectral transmission for the six BK7 optical coatings in ASIR-TB. The points represent the given data and the solid line the model.

4.6.3 LCTFs. The calibration measurements discussed in section 4.3.5 are used to model the VIS LCTFs in ASIR-TB. The NIR filter uses the interpolated data described in the first-order model of ASIS. Figure 4.26 shows the spectral transmission that will be used for ASIR-TB.

4.6.4 Imaging System. As with the sensor optics, the imaging system will contribute to the spectral radiometry of the sensor. The spectral radiometry is given in the quantum efficiency of the CMOS imaging arrays. Figures 4.27 and 4.28 show the modeled quantum efficiency.

4.7 ASIR-TB Experimental Set-up

The experimental set-up of ASIR-TB is shown in Fig 4.29. For this research, Mercury Argon (Hg(Ar)) and Neon (Ne) Newport/Oriel Spectral Pencil lamps are used and emit persistent lines in the VIS and NIR ranges as shown in Fig 4.31 and 4.32 [3]. The location and relative amplitude for each line of the sources was measured with a spectrometer and verified in a database of atomic spectra [43].

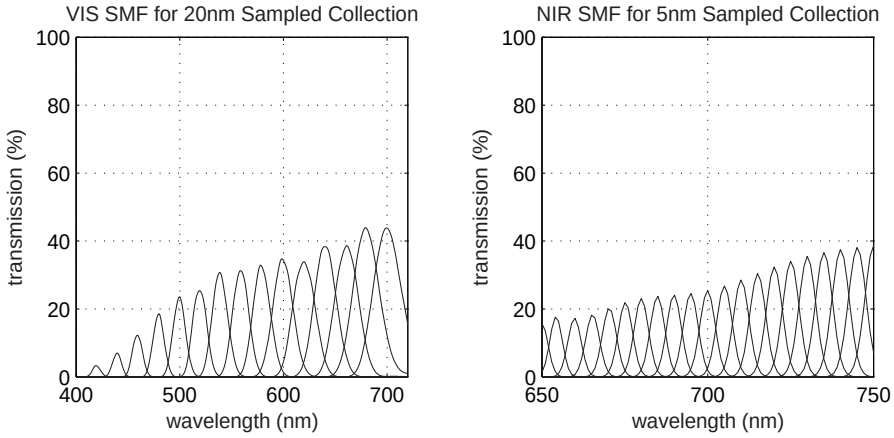

Figure 4.26: The SMF for the visible and near-IR LCTFs. For the visible, there are 15 selected center wavelengths representing a 20nm sampling from 420nm to 720nm. For the near-IR, there are the 21 selected center wavelengths, representing a 5nm sampling from 650nm to 750nm.

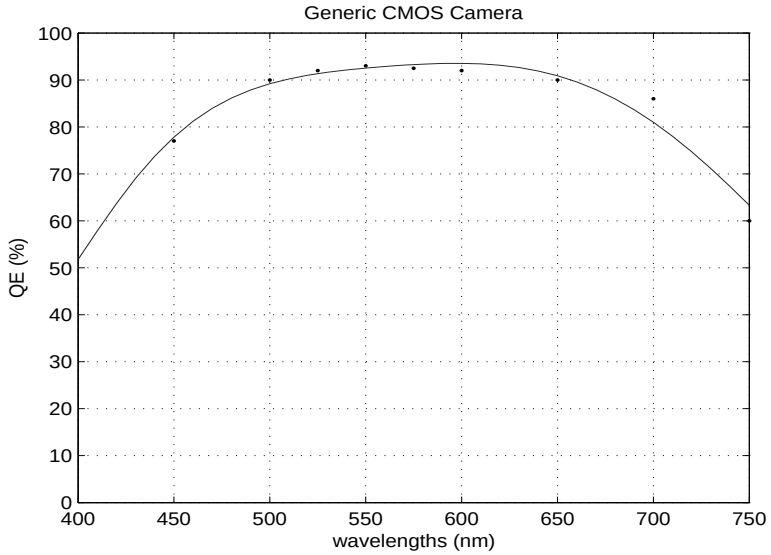

Figure 4.27: Quantum efficiency for a generic CMOS imaging array used for the SMX-110 CMOS imaging array [31]. The points represent the given data and the solid line the model.

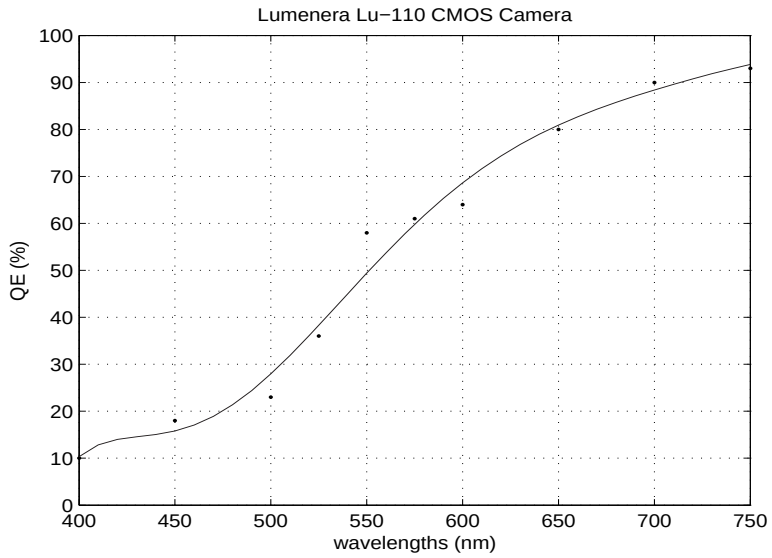

Figure 4.28: Quantum efficiency for the Lu-105 CMOS imaging array. The points represent the given data and the solid line the model.

The pencil lamps consists of a single bulb that is bent back on itself so that two filament like areas can be seen. These two filaments are approximately 3mm wide and are separated by approximately 0.5mm. An image of the source taken with the experimental set-up given in Fig 4.29 is show in Fig 4.33.

To demonstrate the MBSIR algorithm, a spectral data cube of the sources was collected with the experimental set-up described in this section. A known amount of focus error was induced to spatially blur the bulbs together. The LCTF was set to collect a coarse spectral scan of the source. For the visible, this scan was started at 420nm and went to 700nm in 20nm steps. For the NIR, the spectral sampling was from 650nm to 750nm in 5nm steps. The NIR scan was only collected from 650nm to 750nm because the lines over 750nm are not intense enough to be collected. These fifteen images in the VIS and 21 images in the NIR comprised the spectral data cube. The course spectral resolution blurred the spectral lines of the source. The spectral blurring made the spectral lines at 546 and 576/579nm in the visible and lines at 653nm and 660nm; 693nm and 703nm; and 717nm and 724nm in the NIR unresolvable.

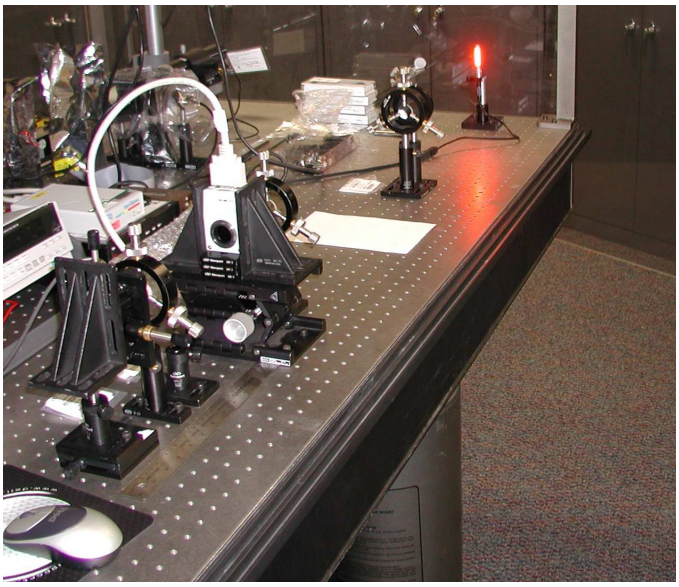

Figure 4.29: The experimental set-up of ASIR-TB for testing the MBSIR algorithm. The system used three lenses to demagnify the spectral source 50 times, while passing collimated light through the LCTF. The source is located at the end of the optics bench, at the top right of the figure.

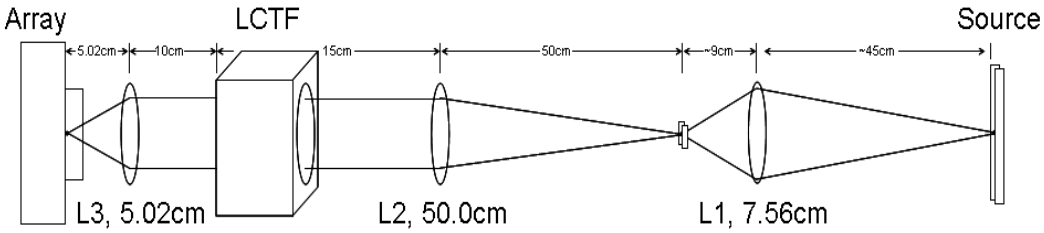

Figure 4.30: A schematic of the experimental set-up for ASIR-TB testing the MBSIR algorithm. The system used three lenses to demagnify the spectral source 50 times, while passing collimated light through the LCTF.

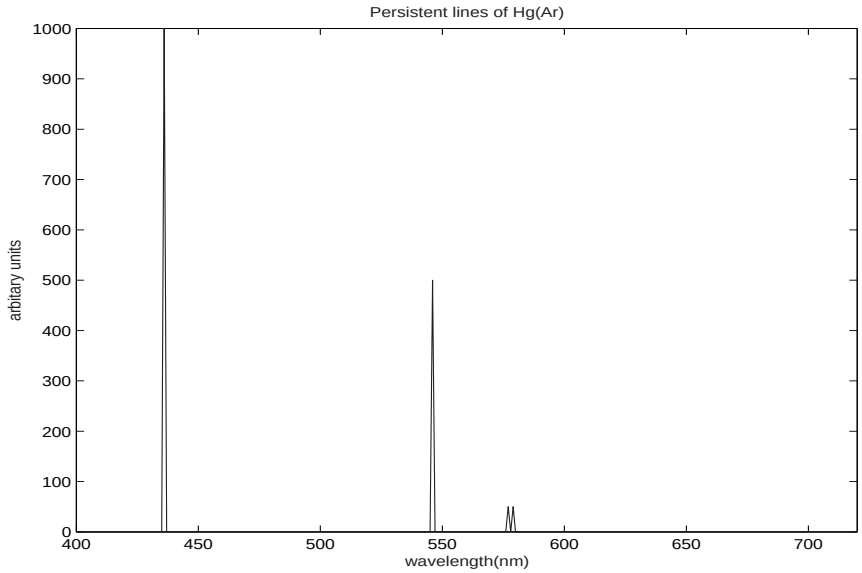

Figure 4.31: The known emission lines of Hg(Ar) [3]. The amplitude of the lines derived from the dominant Hg emissions [43].

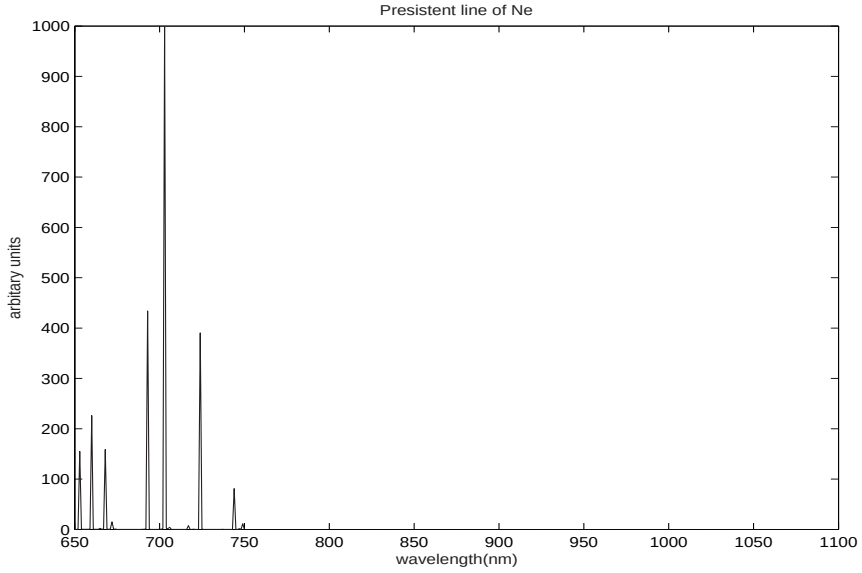

Figure 4.32: The known emission lines of Ne [3]. The amplitude of the lines are referenced from the dominant line [43].

Figure 4.33: An image of the two filament like areas of the Newport/Oriel Hg(Ar) pencil lamp. The image was captured through the LCTF with a selected center wavelength of 546nm. The Ne source looks similar when imaged with the NIR filter.

4.8 Filter Sampling

The sampling for the collection of the spectral data cube ("filter sampling") is critical for the quality of the reconstruction. The MBSIR algorithm functions best when the algorithm is provided shared spectral information between successive images in the spectral data cube. The shared information comes from the overlapping of the bandwidths of the selected filter transmissions. A balance must be reached between too little and too much overlap. Too little overlap yields a lack of shared spectral content in the data reducing the achievable post-processed spectral resolution. Too much overlap provides excessive spectral repetition within the collected data. The over-sampled data increases the required time to collect the spectral image cube while not providing any increase in the post-processed spectral resolution. The effect of filter sampling on the quality of the reconstruction will be further discussed in Chapter VII.

The filter sampling and the sampling of the reconstruction can be chosen independently. Typically, the filter sampling is dependent on time constraints required to image a non-stationary satellite. The faster the object is moving, the coarser the

sampling. However, the coarse filter sampling will degrade the performance of the MBSIR algorithm. The reconstruction sampling is typically 1nm, and is limited by the sampling limitations of the model.

The critical filter sampling can be determined by examining at the cut-off of the Fourier transform of the Gaussian-shaped filter transmission. However, since the Fourier transform of a Gaussian is another Gaussian, a cut-off is never reached. Therefore, assuming that the transformed Gaussian reaches its cut-off when it reaches 1% of its maximum value, the critical sampling is given by,

$$\Delta_\lambda = \frac{2\pi b_w}{\sqrt{-2ln(1\%)}}, \tag{4.2}$$

where b_w is the bandwidth of the transmission of the filter for a certain wavelength selection. Using 5nm as the minimum fixed bandwidth for the visible and near-IR filters, the critical fixed filter sampling is 2.59nm. However, a non-linear filter sampling can also be used. For this case, the filter sampling of each image is dependent on the bandwidth of the previous image. Since the bandwidth of the filter increase with wavelength, employing the non-linear sampling is the most effective way to sample the filter, while maintaining the overlap required to reconstruct the spectral image. Finding the minimum number of images required for spectral reconstruction is critical when imaging non-stationary objects.

4.9 Summary

This chapter developed the three models that are needed in this research. These models are critical to optimize performance of the MBSIR algorithm, and will be used in rest of the research. The first-order model was created while ASIS was still being constructed and uses a summation of predicted models of the ASIS's individual components. The second-order model replaces some of the individual component models with a measured sensor spectral response after the sensor was constructed. The results of the two models are very similar. While either model can be used, the

second-order model is considered more accurate since it used the measured data, but it has a limited spectral sampling.

The other model developed in this chapter was the ASIR-TB model. This model was done as a mixture of the element by element method and calibration method. The lenses and imaging array were modeled separately, but the model for the visible LCTF was constructed from calibration measurements.

The chapter also contains a brief discussion of some sampling issues between the filter and the MBSIR reconstruction. The finer the filter sampling, the better the results. However, the finer filter sampling increases the amount of time it takes to collect the spectral data cube.

V. Simulations

Simulations provide a way to determine the expected performance of the MBSIR algorithm. The models developed in the previous chapter were used for simulations of both the ASIR-TB and ASIS sensors. The first two simulations are a visible and near-IR spectral source as collected by the ASIR-TB sensor. The purpose of the simulations is to show that the ASIR-TB sensor will blur the spectral source such that the source cannot be resolved spatially or spectrally. The MBSIR algorithm was then applied to the simulated data to show the post-processed data can be resolved using the defined criteria.

The third and fourth simulations were simulations of a singlet and binary star collected with the ASIS sensor. The purpose of these simulations is to show the algorithm can reconstruct the spectra of the stars. For the singlet star, a spectral only reconstruction was done. For the binary star, the reconstruction included both spatial and spectral elements.

5.1 Resolution Criteria

In this research two resolution criteria need to be defined. The first is spatial resolution. Two spatial features are resolved if the features can be distinguished in a spatial sense using the familiar Rayleigh criteria [25]. The spectral resolution is defined as the ability to differentiate between two closely spaced spectral features. The criteria to differentiate the two features will be based on the Rayleigh criteria. The spectral features will be defined to be resolvable if the minimum value between the two features is less than 86% of the amplitude of the smaller feature.

5.2 ASIR-TB

A visible and near-IR spectral source collection was simulated with ASIR-TB to show the benefits of the MBSIR algorithm. The visible source was Hg(Ar) and the near-IR source was Ne. In both cases, ASIR-TB blurred the source such that the spatial and spectral features were not resolvable using the defined criteria. The

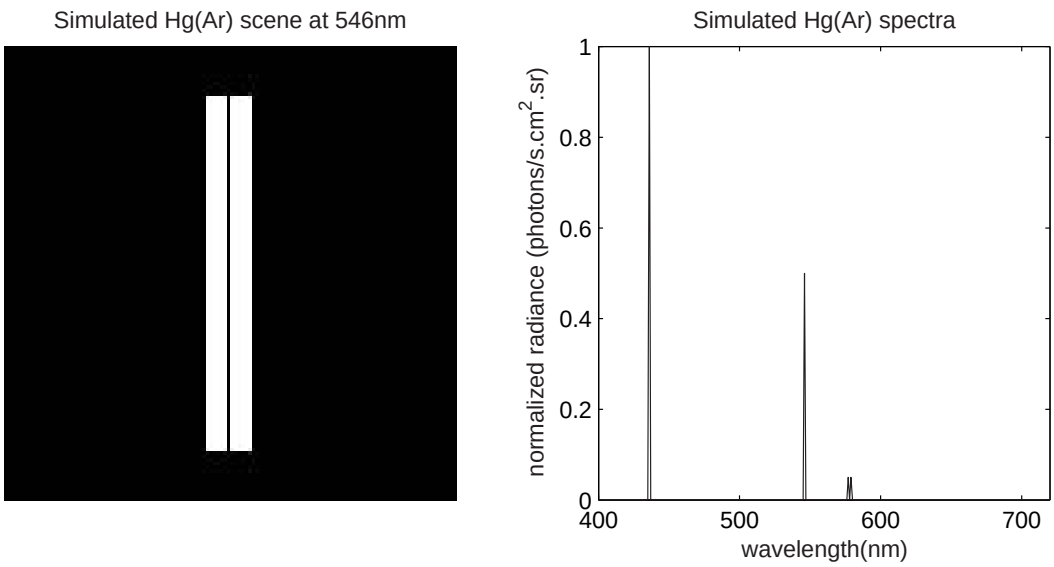

Figure 5.1: The Hg(Ar) source used to create a simulation of the spectral image collection and reconstruction with ASIR-TB. The spatial image is the scene at 546nm.

MBSIR algorithm was applied and the blurring was reduced so the features were resolvable.

5.2.1 Hg(Ar) Spectral Source. This simulation began with the creation of a Hg(Ar) source with the same spatial and spectral profile as the actual source. The simulated spatial and spectral scene is shown in Figure 5.1. This spectral cube of the source has 321 image plans, or one image plane for every 1nm from 400nm to 720nm.

5.2.1.1 Hg(Ar) Simulated Data Generation. The ASIR-TB model developed in section 4.5 was used to create a simulated spectral data cube of the source. The OTF was calculated for each wavelength and was used to spatially blur the image of the simulated source in Figure 5.1. Each of the images in the scene was then multiplied by the spectral transmission profiles of the LCTF. The application of the spectral mixing function reduced the image cube from 321 planes for the source to 15 planes for the data. These 15 image planes correspond to the selected LCTF sampling of 20nm from 420nm to 720nm. Poisson noise was added to the simulated data cube to account for the expected statistical noise of the collected image. One

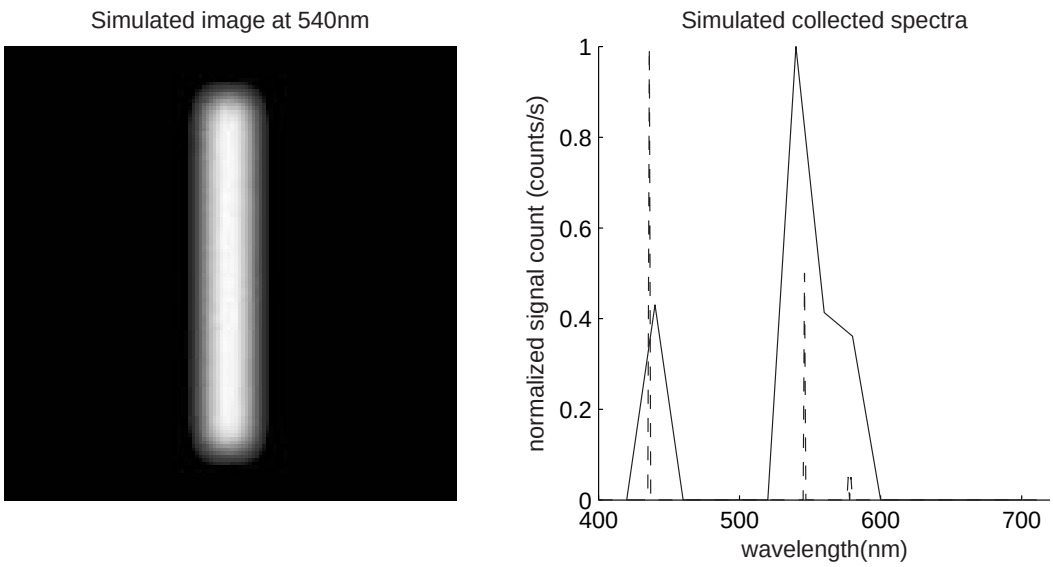

Figure 5.2: Simulation of the Hg(Ar) source collected by ASIR-TB. The spatial image is the scene at 540nm. The solid lines represent the spectra of the simulated image, while the dashed lines are the spectral lines of the source.

image of the simulated spectral data cube is shown in Figure 5.2. Notice that the two filaments in the image and the lines at 546nm and 577/579nm in the spectra are no longer resolvable.

5.2.1.2 Hg(Ar) Simulated Reconstruction. The MBSIR algorithm was then applied to the simulated spectral data cube. Starting with an initial guess of unity for the scene, the MBSIR algorithm iterated to reduce the blurring. The application of the MBSIR algorithm produced a reconstructed source with 321 image planes, or a plane for every 1nm from 400nm to 720nm. The reconstructed source scene and spectra are shown in Figure 5.3.

5.2.1.3 Hg(Ar) Simulation Results. A closer examination of the results show that, in the simulation, the MBSIR algorithm was able to resolve the two filaments in the image and the 546nm and 577/579nm lines in the spectra. A close up of these areas is shown in Figure 5.4, where the solid line represents the resolvable features in the reconstruction and the dashed line the unresolvable features as

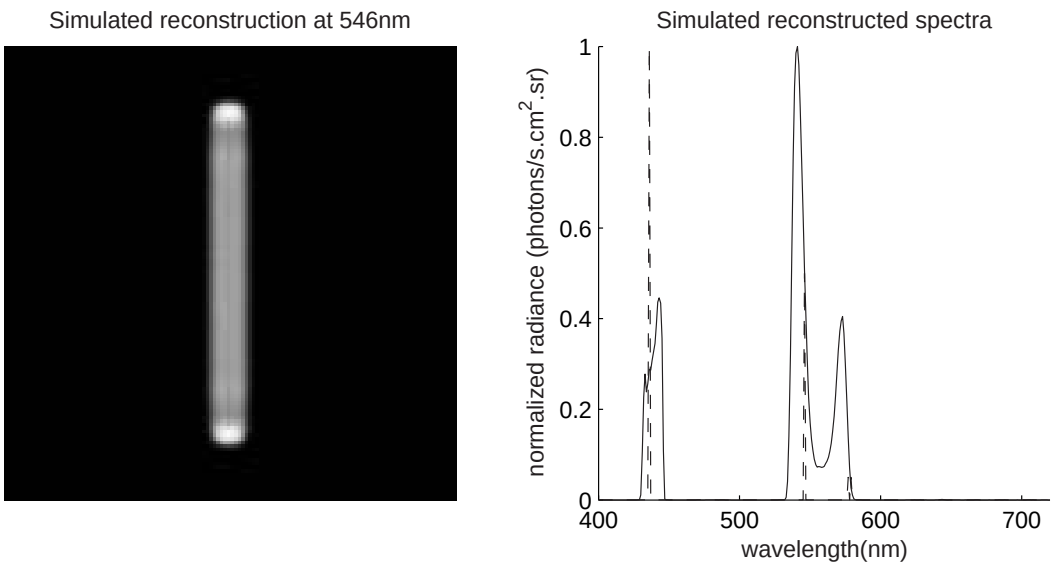

Figure 5.3: Simulated reconstruction of the Hg(Ar) scene. Image is the source at 546nm. The solid lines represent the spectra of the simulated reconstruction, while the dashed lines are the spectral lines of the source.

they were prior to processing. Thus, the MBSIR algorithm has been demonstrated in simulation to improve both the spatial and spectral resolution of a spectral image.

The simulation does show the reconstruction was not able to place the features at the correct locations, or with the correct amplitudes. These differences will be discussed in the next chapter.

5.2.2 Ne Spectral Source. As with the Hg(Ar) source, the NIR simulation began with the creation of a simulated Ne source. The simulated spatial and spectral scene was shown in Figure 5.5 and has the same spatial and spectral profile as the actual source. This spectral cube of the source has 101 image plans, or one image plane for every 1nm from 650nm to 750nm. The NIR wavelength range was reduced because the lines for Ne over 750nm and not detectable with ASIR-TB. Including these undetectable lines greatly increase the computation time for the algorithm with no benefit.

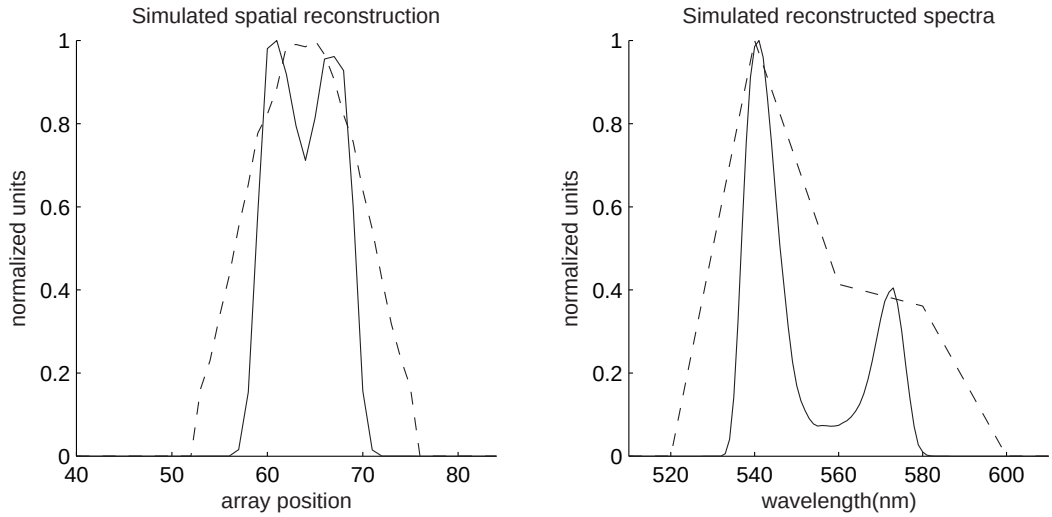

Figure 5.4: Demonstration of the non-resolved to resolved spatial and spectral profile of the simulated Hg(Ar) source.

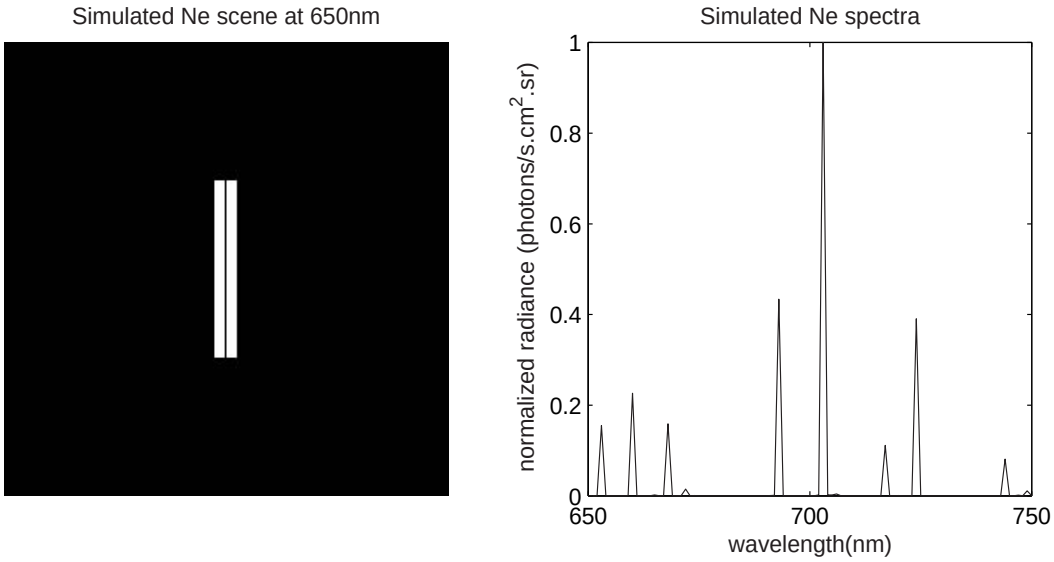

Figure 5.5: The Ne source used to create a simulation of the spectral image collection and reconstruction with ASIR-TB. The spatial image is the scene at 650nm.

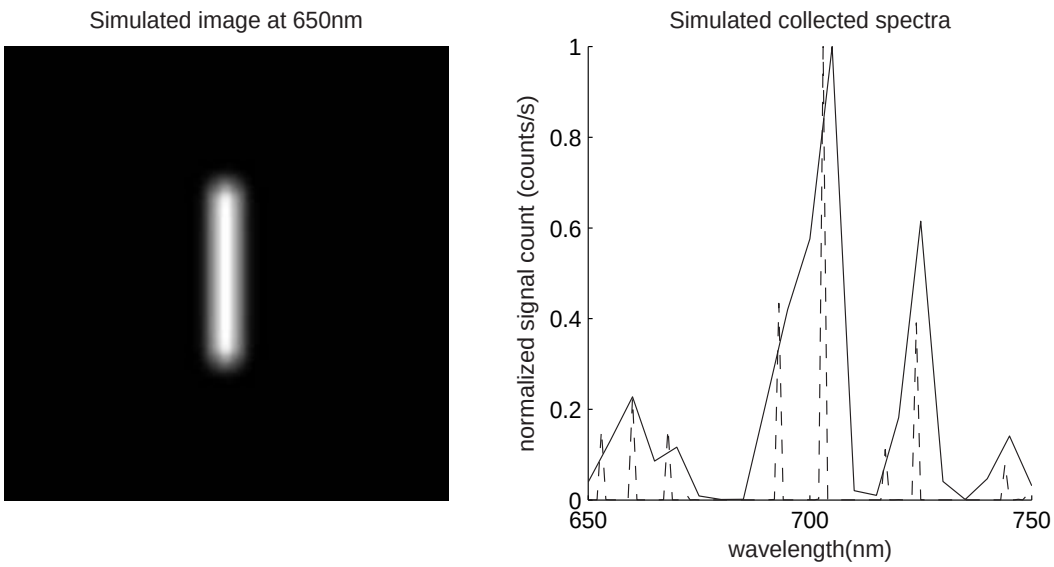

Figure 5.6: Simulation of the Ne source collected by ASIR-TB. The spatial image is the scene at 650nm. The solid lines represent the spectra of the simulated image, while the dashed lines are the spectral lines of the source.

5.2.2.1 Ne Simulated Data Generation. The ASIR-TB model developed in section 4.5 was used to create a simulated spectral data cube of the source. The OTF was calculated for each wavelength and was used to spatially blur the image of the simulated source in Figure 5.5. Each of the images in the scene was then multiplied by the spectral transmission profiles of the LCTF. The application of the spectral mixing function reduced the simulated data cube from 101 planes for the source to 21 planes for the data. These 21 image planes correspond to the selected LCTF sampling of 5nm from 650nm to 750nm. Poisson noise was added to the simulated data cube to account for the expected statistical noise of the collected image. The simulated spectral data cube is shown in Figure 5.6. Notice that the two filaments in the image and the lines at 653nm and 660nm; 693nm and 703nm; and 717nm and 724nm in the spectra are no longer resolvable.

5.2.2.2 Ne Simulated Reconstruction. The MBSIR algorithm was then applied to the simulated data. Starting with an initial guess of unity for the scene, the MBSIR iterated on the estimate of the scene until the algorithm reduced as much of

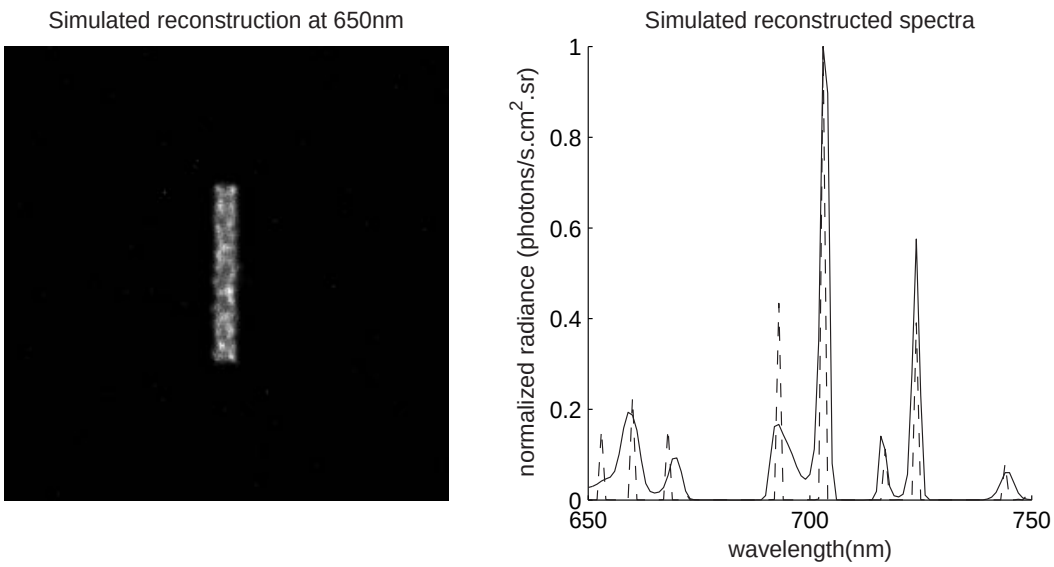

Figure 5.7: Simulated reconstruction of the Ne scene. Image is the source at 650nm. The solid lines represent the spectra of the simulated reconstruction, while the dashed lines are the spectral lines of the source.

the blurring as possible. The application of the algorithm produced a reconstructed source with 101 image planes, or a plane for every 1nm from 650nm to 750nm. The reconstructed source scene and spectra are shown in Figure 5.7.

5.2.2.3 NIR Simulation Results. A closer examination of the results show that, in the simulation, the MBSIR algorithm was able to resolve the two filaments in the image and the 653nm and 660nm; the 693nm and 703nm; and the 717nm and 724nm lines in the spectra. A close up of these areas is shown in Figure 5.8, where the solid line represents the resolvable features in the reconstruction and the dashed line the unresolvable features in the simulated image. Thus, the MBSIR algorithm has demonstrated the ability to improve both the spatial and spectral resolution of a spectral image. As with the Hg(Ar) simulation, the reconstruction shows similar, but not quite as pronounced, difference in the reconstructed feature locations and amplitudes from truth. These differences will also be discussed in the next chapter.

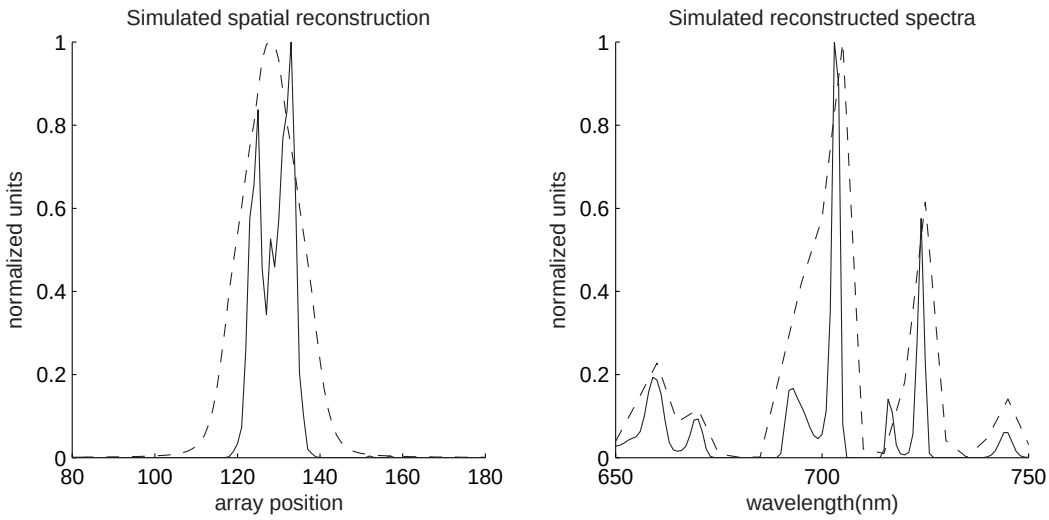

Figure 5.8: Demonstration of the non-resolved to resolved spatial and spectral profile of the simulated Ne source. The solid lines represent the cross-section of the simulated reconstructed image and the spectra of the simulated reconstruction, while the dashed lines are the cross-section and spectra of the simulated image.

5.2.3 ASIR-TB Simulation Results. The simulations for the Hg(Ar) and the Ne sources show that the MBSIR algorithm can successful reduce the blurring of a spectral image. While the exact image scene is not reconstructed, the algorithm is able to resolve both spatial and spectral features in the images after post-processing, that were not resolvable when the image was collected.

5.3 ASIS

To simulate the performance of the MBSIR algorithm on data collected with ASIS, two different simulations were used. The first simulation was a spectral only reconstruction of a singlet star. A binary star was then used to simulate the performance of the algorithm with the added spatial component.

For the both star simulations, the first-order ASIS model developed in section 4.2 was used. For the singlet star simulation, the filter sampling will be set at 5nm, so 57 images will be collected in the visible (every 5nm between 420nm and 700nm) and 69 images in the near-IR (every 5nm between 660nm and 1050nm). For the binary star simulation, the filter sampling will be set at 1nm, so 321 images will be collected in the

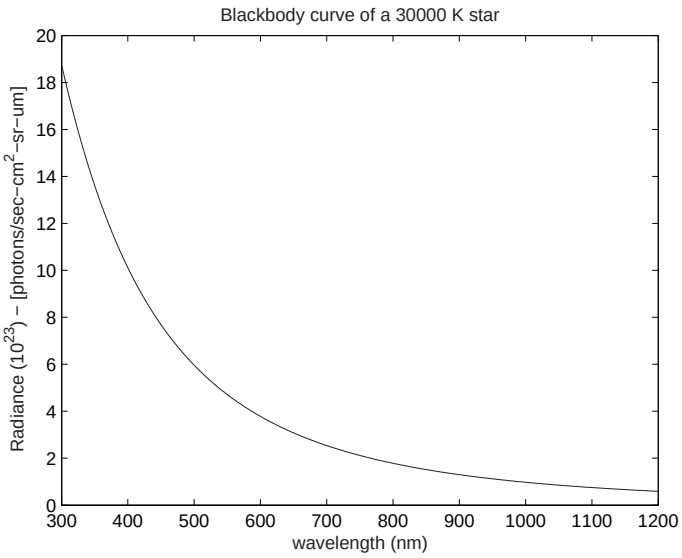

Figure 5.9: Spectral output of a 30000K star. The O class star is assumed to be a perfect blackbody.

visible (every 1nm between 420nm and 700nm) and 391 images will be collected in the near-IR (every 1nm between 660nm and 1050nm). For both simulations, the MBSIR algorithm was used to reconstruct the spectra of the scene to a 1nm resolution, but with the blurring reduced. For the binary star, diffraction in the ASIS aperture was the only spatial blurring.

5.3.1 Singlet Star. The first simulation was a spectral only reconstruction of a 30,000K singlet star. For this simulation, no spatial blurring was used. The spectra of the star will be blurred and then reconstructed using a spectral only reconstruction.

According to the Planck blackbody equation, the 30,000K star has the spectra like the one shown in Figure 5.9 [15]. This was the input to the vector representing the spectra of the true scene. Since this was a spectral only reconstruction, there was no spatial component.

5.3.1.1 Singlet Star Data Generation. The blackbody curve in Figure 5.9 was used with the first-order model of ASIS to produce the simulated spectra. For radiometric purposes in this scenario, the following parameters for the singlet star

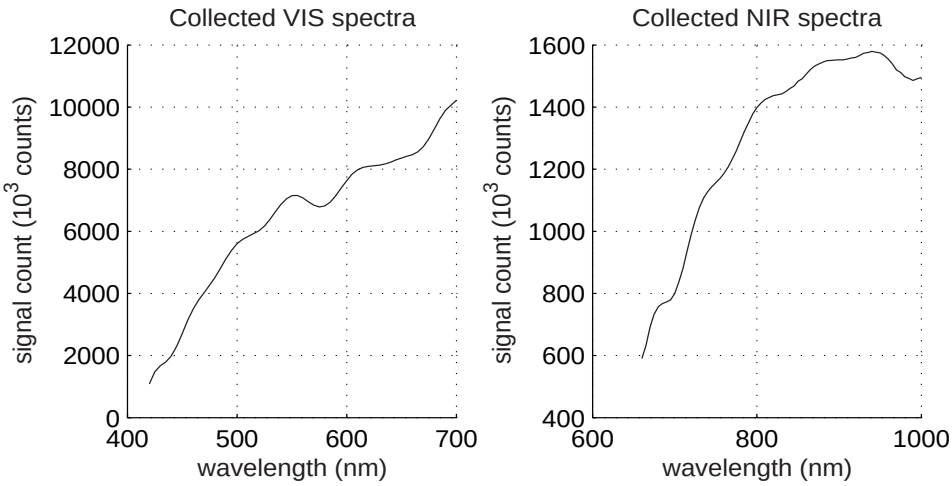

Figure 5.10: Collected spectra of a 30000K star. The O class star is simulated to be 2.5 solar units and at a distance of 220 light years.

were used; the star is at a distance of 220 light years and has a radius of 2.5 solar units. A set integration time of 1s was used for the sensor imaging arrays. Poisson noise was added to the simulated data to account for the expected noise. Figure 5.10 shows the simulated singlet star data.

5.3.1.2 Singlet Star Reconstruction. The spectral-only MBSIR algorithm from Equation (3.17) was then applied to the spectra shown in Figure 5.10. The reconstruction was started with an initial guess of unity for the entire reconstruction vector. The result of the spectral-only MBSIR algorithm are shown in Figure 5.11.

5.3.1.3 Singlet Star Simulation Results. As Figure 5.12 shows, the average percent difference between the reconstruction and the truth data for the visible and near-IR spectra is approximately 0.5% for this scenario. Therefore, the simulation shows the reconstruction was able to undo much of the spectral blurring inherent in ASIS. The reconstruction is worse near the upper and lower wavelengths of the spectra. This is due to the algorithm estimating the spectra at the edges of the filter settings where there is a lack information needed for reconstruction.

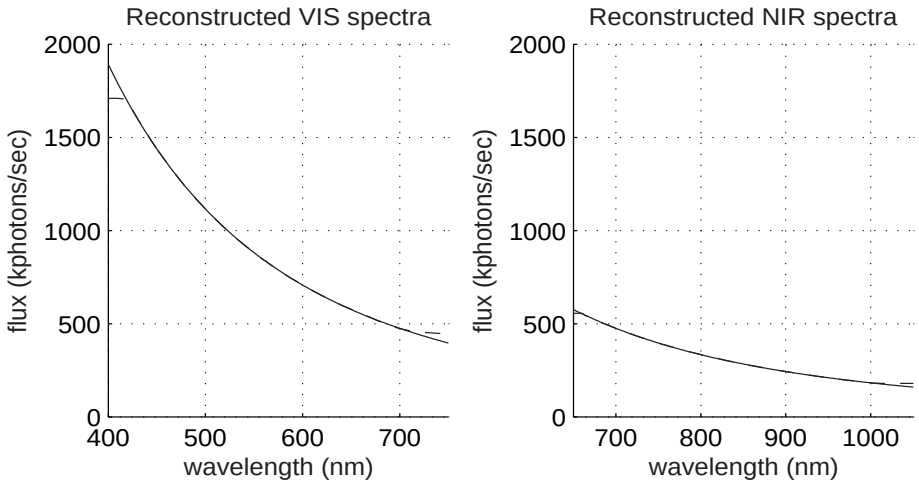

Figure 5.11: Reconstructed spectra of a 30000K star. The solid line represents the true spectra, while the dashed line is the reconstructed spectra. The dashed and solid lines overlap in the figure.

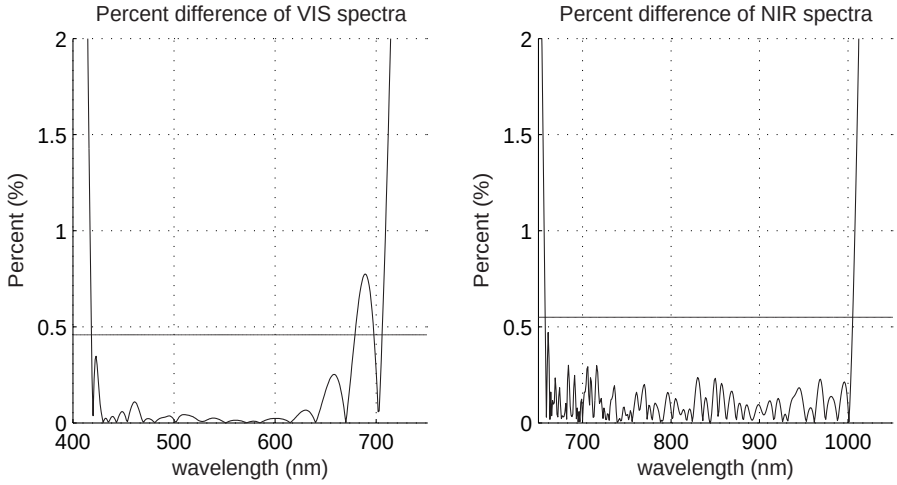

Figure 5.12: Percent difference between the truth and spectral-only reconstructed blackbody spectra of the singlet star. The strait line represents the average percent difference.

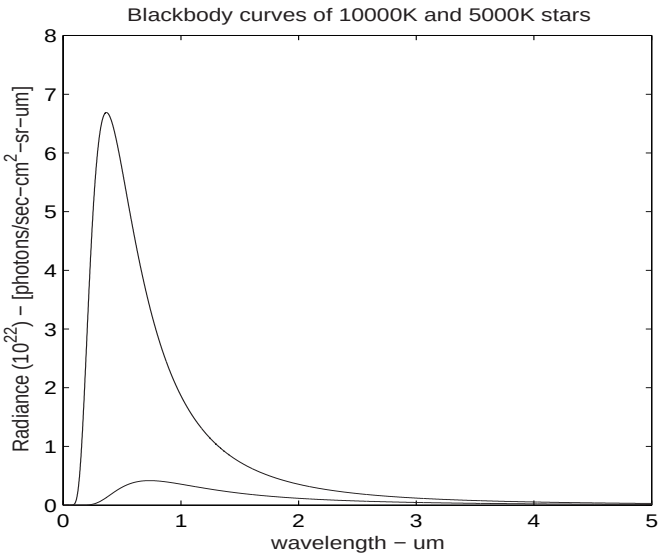

Figure 5.13: Spectral output of a 10000K and 5000K binary star. Both the B and G class stars are assumed to be perfect blackbodies.

5.3.2 Binary Star. The binary star simulation expands on the singlet star simulation in the previous section and shows the performance of the algorithm when the spatial blurring was introduced.

According to the Planck blackbody equation, a 10,000K and 5,000K binary star has the spectral output like that shown in Figure 5.13. This was the spectral input to the spectral image cube representing the true image scene. The spatial component of this true scene was two point sources. The point sources were separated by one pixel, which represents a 0.04 arc second separation of the two stars. The visible and near-IR true spectral cubes are shown in Figures 5.14 and 5.15.

5.3.2.1 Binary Star Spectral Data Generation. The blackbody curves in Figures 5.14 and 5.15 are then used with the first-order model of ASIS to produce the simulated data. For radiometric purposes the following parameters for the binary star were used; both stars are at a distance of 25 light years and star one has a radius of 0.25 solar units and star two has a radius of 5 solar units. A set integration time of 1s was used for the sensor imaging arrays. Poisson noise was then added to anticipate the

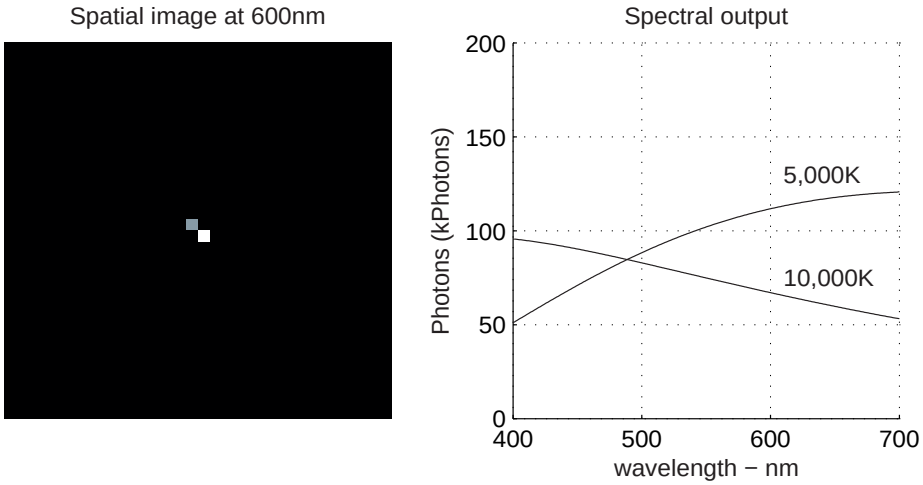

Figure 5.14: Spatial image and spectral output of a 0.25su radius 10000K and a 5su radius 5000K binary star separated by 0.04arcsecs at a distance of 25 light years in the visible.

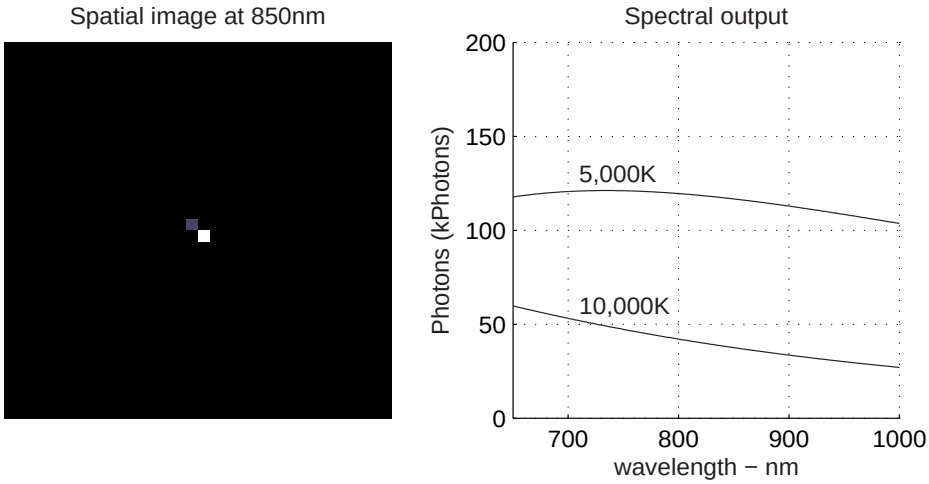

Figure 5.15: Spatial image and spectral output of a 0.25su radius 10000K and a 5su radius 5000K binary star separated by 0.04arcsecs at a distance of 25 light years in the near-IR.

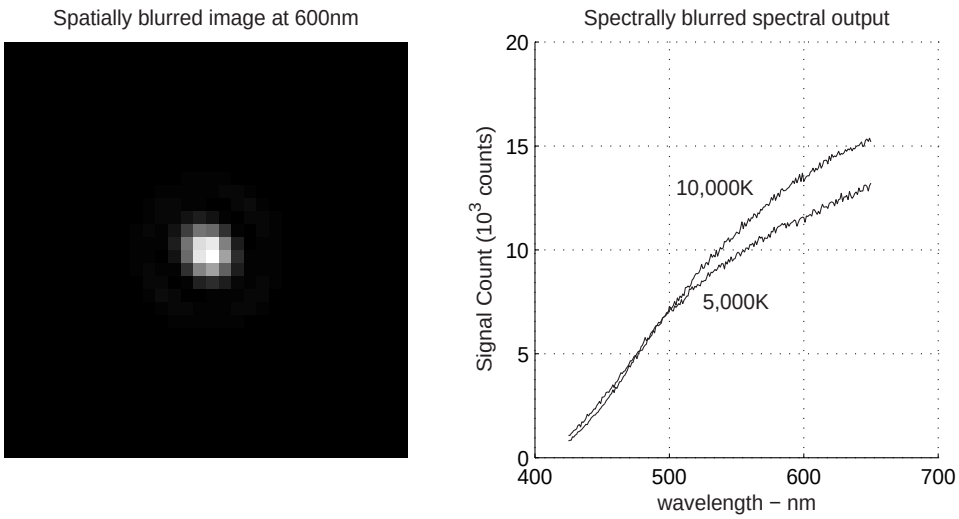

Figure 5.16: Spatially and spectrally blurred image and spectral output of a 0.25su radius 10000K and a 5su radius 5000K binary star at 25 light years in the visible.

expected noise. The model of the sensor blurred the true image scene both spatially and spectrally in the visible and near-IR as shown in Figures 5.16 and 5.17.

5.3.2.2 Binary Star Reconstruction. The MBSIR algorithm from Equation (3.15) was then applied to the spatially and spectrally blurred images shown in Figures 5.16 and 5.17. Again, the reconstruction was started with an initial guess of unity for the entire spectral image cube. The results of the MBSIR algorithm are shown in Figures 5.18 and 5.19. In these figures, a least-squares polynomial line is fit to the final reconstruction is used to smooth out some of the discontinuities in the estimation. The discontinuities are a results of residual spatial blurring in the reconstruction cube. The spatial portion of the MBSIR algorithm did not place all of the photons back into the proper pixel locations. This results in a spectra difference when looking a singe pixel location. These discontinuities are not seen in the spectral only reconstruction, as seen in the singlet star reconstruction shown in Figure 5.11.

5.3.2.3 Binary Star Simulation Results. As Figures 5.18 and 5.19. show, the two stars are resolvable after applying the MBSIR algorithm. Additionally, as Figure 5.20 shows, the average percent difference between the reconstruction and

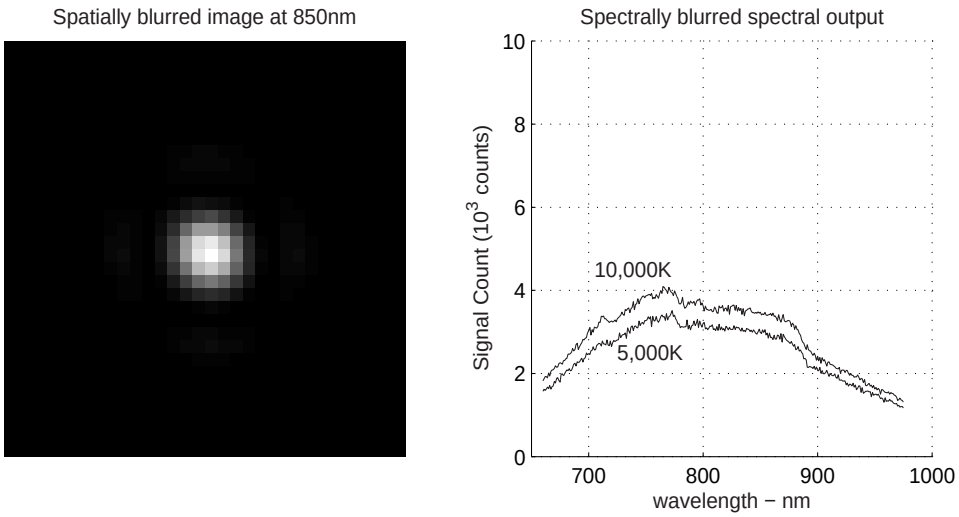

Figure 5.17: Spatially and spectrally blurred image and spectral output of a 0.25su radius 10000K and a 5su radius 5000K binary star at 25 light years in the near-IR.

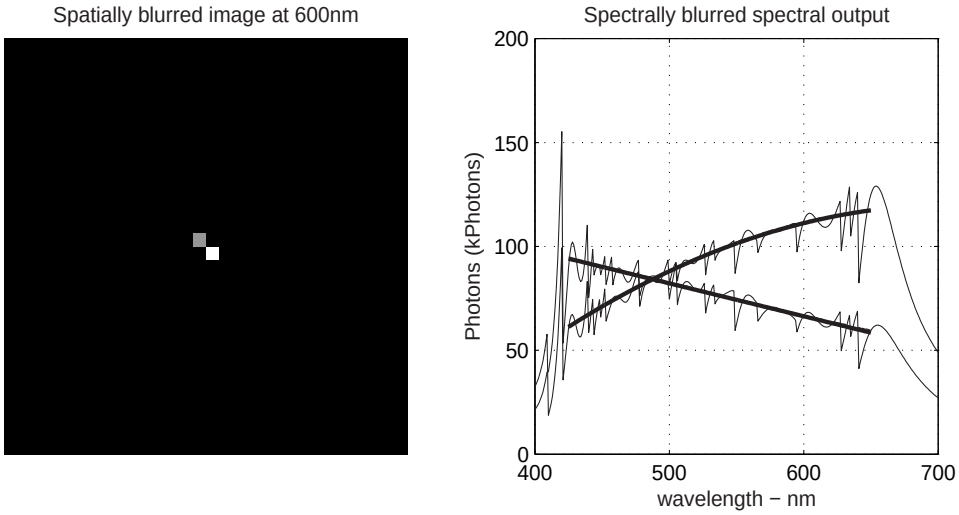

Figure 5.18: Spatially and spectrally reconstructed image and spectral output of a 0.25su radius 10000K and a 5su radius 5000K binary star at 25 light years in the visible. The thin solid line is the reconstruction and the thick line is a least-squares polynomial fit to the reconstruction to smooth out some discontinuities. The true spectra is shown in a dashed line and cannot be seen since it is coincident with the MMSE fit to the reconstruction.

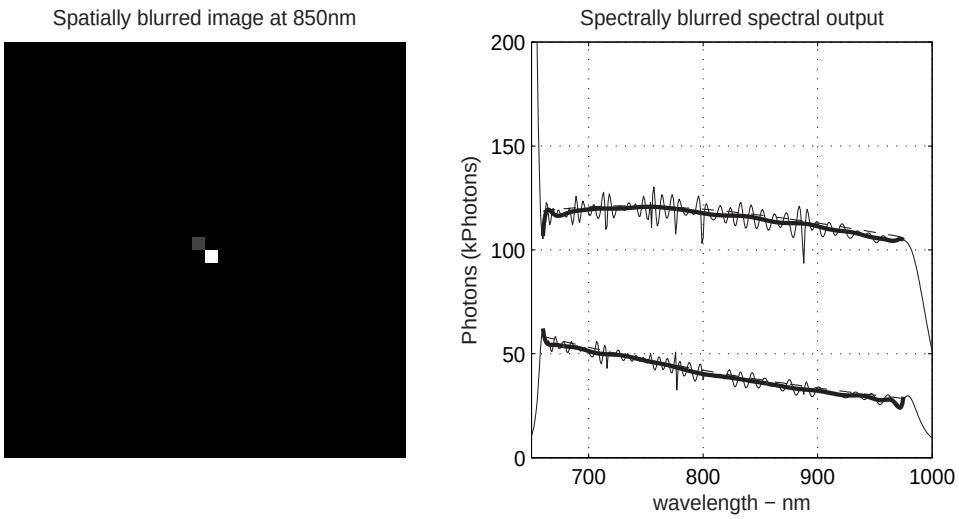

Figure 5.19: Spatially and spectrally reconstructed image and spectral output of a 0.25su radius 10000K and a 5su radius 5000K binary star at 25 light years in the near-IR. The thin solid line is the reconstruction and the thick line is a least-squares polynomial fit to the reconstruction to smooth out some discontinuities. The true spectra is shown in a dashed line and cannot be seen since it is coincident with the MMSE fit to the reconstruction.

the truth data for the visible approximately 4% for both stars in the visible and 5.5% and 3% in the near-IR. Therefore, the simulation shows that the reconstruction was able to undo much of the blurring in ASIS. As with the singlet star, the edges of the spectra are less accurate.

5.3.3 ASIS Simulation Results. As the two simulations show, the spectra of the stars collected with ASIS were blurred. Using the MBSIR algorithm successfully reduced the blurring in the simulated images to recover the blackbody curves of the stars.

5.4 Summary

The purpose of the simulations in this chapter was to show the benefit of the MBSIR algorithm. These simulations showed that the MBSIR algorithm can significantly improve the resolution of images collected with ASIR-TB and ASIS. While the reconstructed image scenes are not perfect, the algorithm is capable of resolving

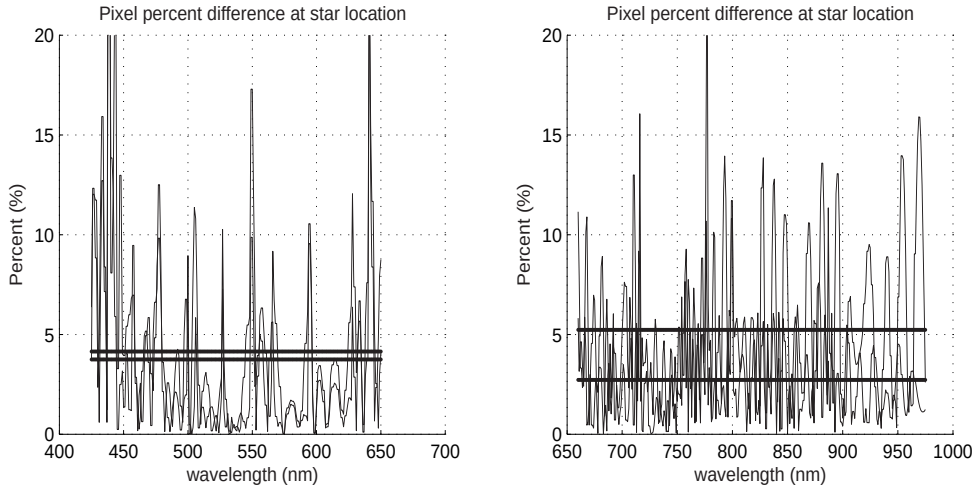

Figure 5.20: Pixel percent difference between the truth and reconstructed blackbody curves of the binary star. The strait lines represent the average percent difference.

features that were not resolvable in the simulated data. The next step is to apply the algorithm to collected data.

VI. Data

This chapter will repeat the processing from the previous chapter, but the MBSIR algorithm will be used on data collected with ASIR-TB and ASIS. The Hg(Ar) and Ne source collected with ASIR-TB will be shown first, followed by a singlet star collected with ASIS. The goal of this chapter is to demonstrate the resolution improvements shown in the simulations are possible with actual data. The results in this chapter will show the MBSIR algorithm will improve the resolution of spectral images.

6.1 Resolution Criteria

The same resolution criteria used for the simulations in the previous chapter will be used for the data in this chapter. The spatial resolution will be defined by the familiar Rayleigh criteria [25]. The spectral resolution is based on the Rayleigh criteria. Two spectral features is defined as resolved if the minimum value between the two features is less than 86% of the spectral amplitude of the smaller feature.

6.2 ASIR-TB

The ASIR-TB sensor was configured to collect the Hg(Ar) and Ne spectral sources as described in section 4.7. The same parameters used for the simulations are applied to the data collection.

6.2.1 Hg(Ar) Spectral Source. ASIR-TB was set-up to collect data of the Hg(Ar) source with the same parameters given for the simulation. Fifteen images were collected of the source, one image for each 20nm sampling from 420nm to 700nm. One of the collected images of the source and the collected spectra are shown in Figure 6.1. As with the simulated image, the filaments and the spectral lines at 546nm and 577/579nm are not resolvable.

6.2.1.1 Hg(Ar) Reconstruction. The MBSIR algorithm was then applied to the collected data. As with the simulation, the reconstruction produced 321

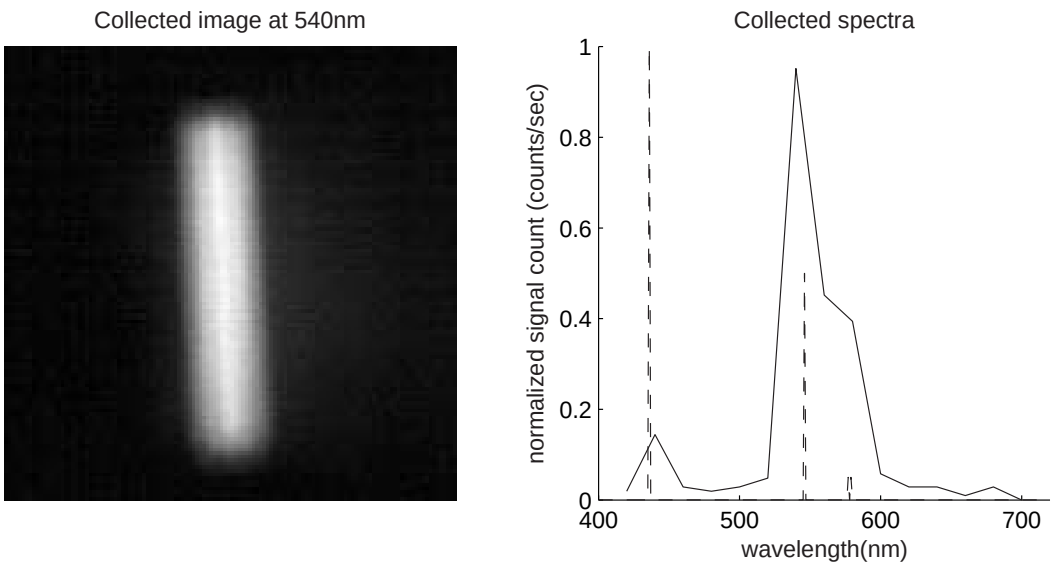

Figure 6.1: Collected spectral image collected by ASIR-TB. Spatial image is the image at 540nm and the spectra was collected from 420nm to 700nm at a 20nm sampling. The dashed lines represent the location and amplitudes of the spectra of the Hg(Ar) source.

images, or one spectral image plane for every 1nm from 400nm to 720nm. The results of the reconstruction are shown in Figure 6.2.

6.2.1.2 Hg(Ar) Results. An examination of the results of the MBSIR algorithm shows that after applying the algorithm, the filaments and the spectral lines are resolvable. The areas of interest are shown in Figure 6.3, where the solid lines are the resolvable features in the reconstruction and the dashed lines the unresolvable features in the collected data.

While the features are resolvable, the algorithm did not place the resolved features at the correct wavelengths. The algorithm placed the 546nm feature at 539nm and the 577/579nm feature at 575nm. These differences of 7nm and 4nm are consistent with the simulated results. In the simulation, the 546nm feature was reconstructed at 541nm and the 577/579nm feature at 575nm for a difference of 5nm and 3nm. The inaccuracy in the placement of the reconstructed spectral features is due to the coarse spectral scan used and the selected filter sampling wavelengths. At a higher

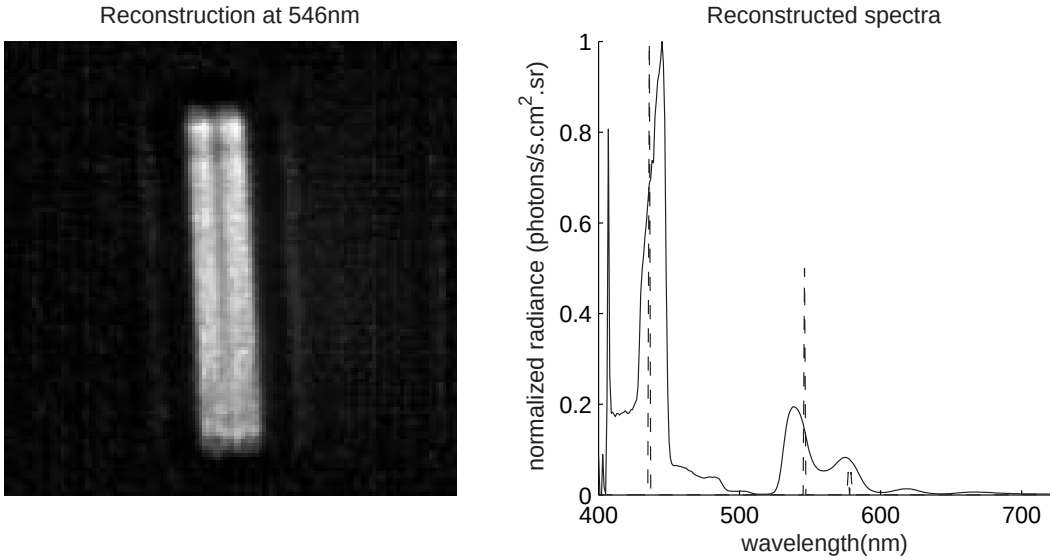

Figure 6.2: Reconstruction of the collected Hg(Ar) source. The dashed lines represent the location and amplitudes of the spectra of the Hg(Ar) source.

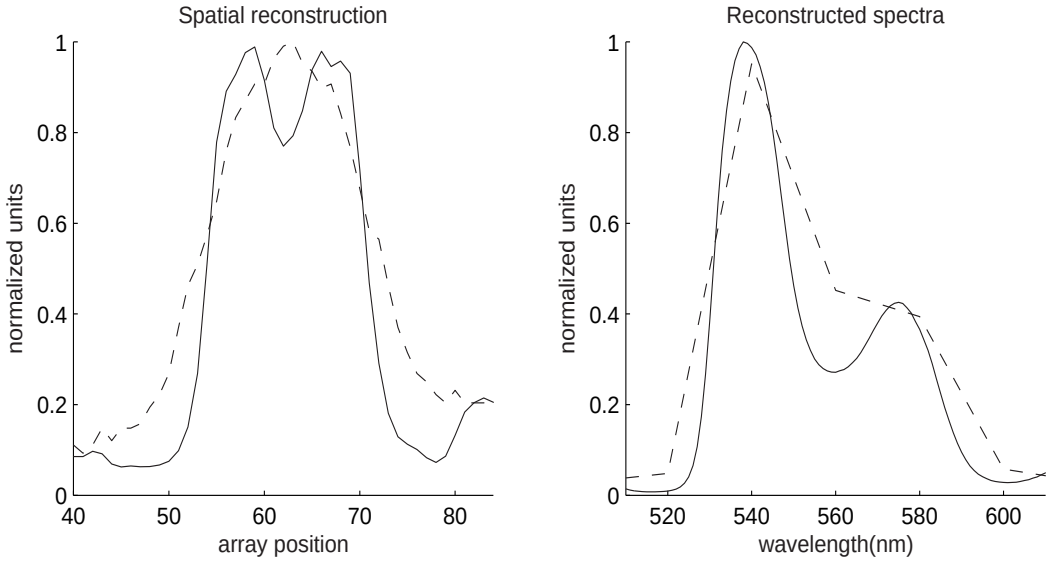

Figure 6.3: Demonstration of the non-resolved to resolved spatial and spectral profile of the Hg(Ar) source. The solid lines represent the cross-section of the reconstructed image and the spectra of the reconstruction, while the dashed lines are the cross-section and spectra of the image. The dashed lines show the unresolved spatial and spectral features in the collected image, and the solid lines show the same features are resolvable after applying the MBSIR algorithm.

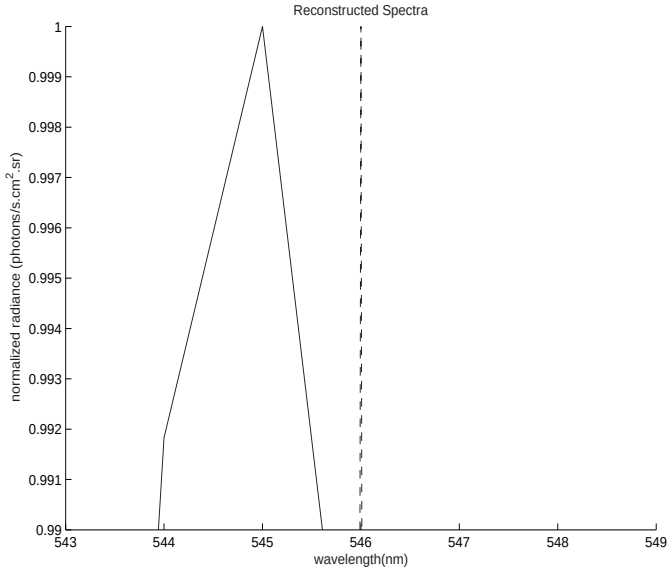

Figure 6.4: The spectral accuracy of the reconstruction was improved when the filter center wavelengths were shifted The reconstruction is shown in the solid line and the dashed line shows the location of the spectral feature. With the shifted selected wavelengths, the difference is now only 1nm.

resolution spectral scan, as Chapter VII will show, a more accurate reconstruction can be expected. In addition, if the same coarse sampling is used, but the selected center wavelengths are shifted to be 426nm to 686nm with a 20nm sampling, the accuracy also improves. To show this, the processing was repeated, but with the shifted center wavelengths. As Figure 6.4 shows, the reconstruction shown in the solid line, now only differs from the location of the spectral feature shown in the dashed line, by 1nm. The improved accuracy is due to the alignment of the feature location with the filter's selected center wavelength.

The results also show a difference in the anticipated and reconstructed amplitude of the spectral features. In the original Hg(Ar) scene, the ratio of the persistent line amplitudes is approximately 10. In the reconstruction, the features are not completely reconstructed back to a single wavelength bin. Instead, there is some residual spectral blurring around the location of the features. The blurring is due to the coarse 20nm filter sampling used to collect the image. The coarse resolution led to photons that should have been placed in the 546nm feature to be placed near the 577/579nm feature

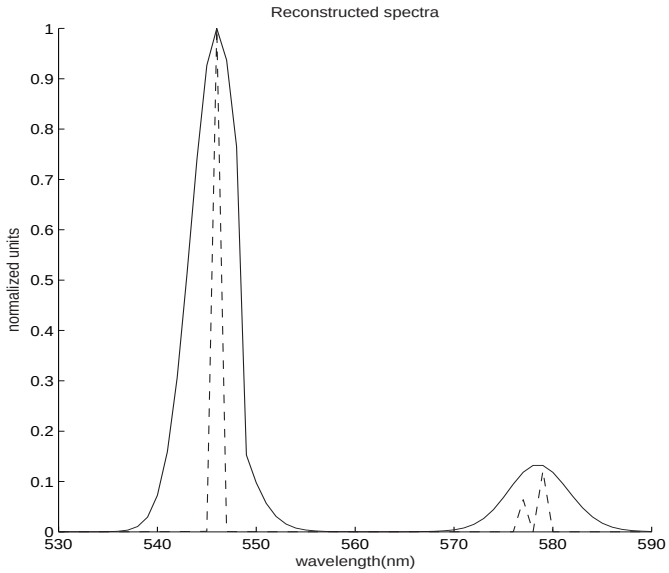

Figure 6.5: The Hg(Ar) source reconstructed when an initial filter sampling of 2nm was used. The higher filter sampling leads to a more accurate reconstruction of the spectral feature amplitudes.

during reconstruction. This lowered the amplitude of the 546nm feature, while raising the 577/579nm amplitude, resulting in the incorrect ratio.

If a higher spectral scan is used then the amplitudes are reconstructed to the proper ratio. Figure 6.5 shows the reconstruction of the Hg(Ar) scene when the data was collected with a 2nm filter sampling. The 2nm sampling allows the algorithm to properly place the photons of the two features. As the figure shows, the reconstruction of the higher filter sampling reconstructs the feature amplitudes to a ratio of 10, matching the measured truth for the source.

6.2.2 Ne Spectral Source. ASIR-TB was set-up to collect data of the Ne source with the same parameters given for the simulation. Twenty-one images were collected of the source, or one image for a 5nm sampling from 650nm to 750nm. One of the collected images of the source and the collected spectra are shown in Figure 6.6. As with the simulated image, the filaments and the spectral lines at 653nm and 660nm; 693nm and 703nm; and 717nm and 724nm are not resolvable.

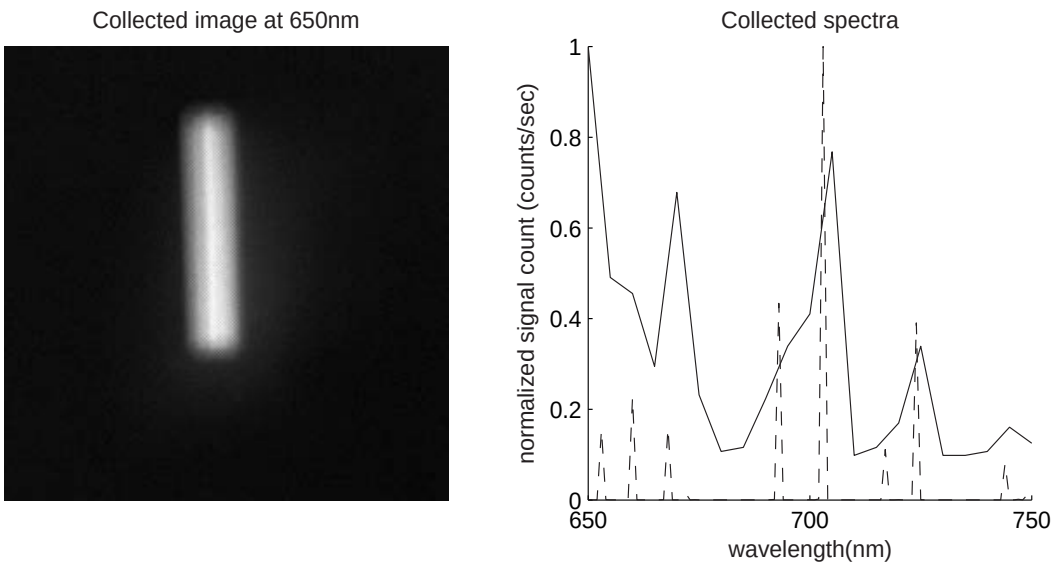

Figure 6.6: Collected spectral image collected by ASIR-TB of the Ne source. Spatial image is the image at 650 and the spectra was collected from 660nm to 750nm at a 5nm sampling. The dashed lines represent the location and amplitudes of the spectra of the NE source.

6.2.2.1 Ne Data Reconstruction. The MBSIR algorithm was then applied to the collected data. As with the simulation, the reconstruction produced 391 images, or one spectral image plane for every 1nm from 660nm to 1050nm. The results of the reconstruction are shown in Figure 6.7.

6.2.2.2 Ne Data Results. As in the simulation of the Ne source, the filaments and the spectral lines are resolvable. A close up of the areas of interest is shown in Figure 6.8, where the solid lines are the resolvable features in the reconstruction and the dashed lines the unresolvable features in the collected data.

The location of the reconstructed features in the Ne are more accurate then the Hg(Ar) reconstruction, with the Ne averaging an accuracy error of 1.3nm to the average 5.5nm accuracy error for the Hg(Ar). The increased accuracy of the Ne source is due to the finer filter sampling used for the Ne data. All of the resolved spectral features in the Ne data, except for the 667nm feature, have only a 1nm accuracy

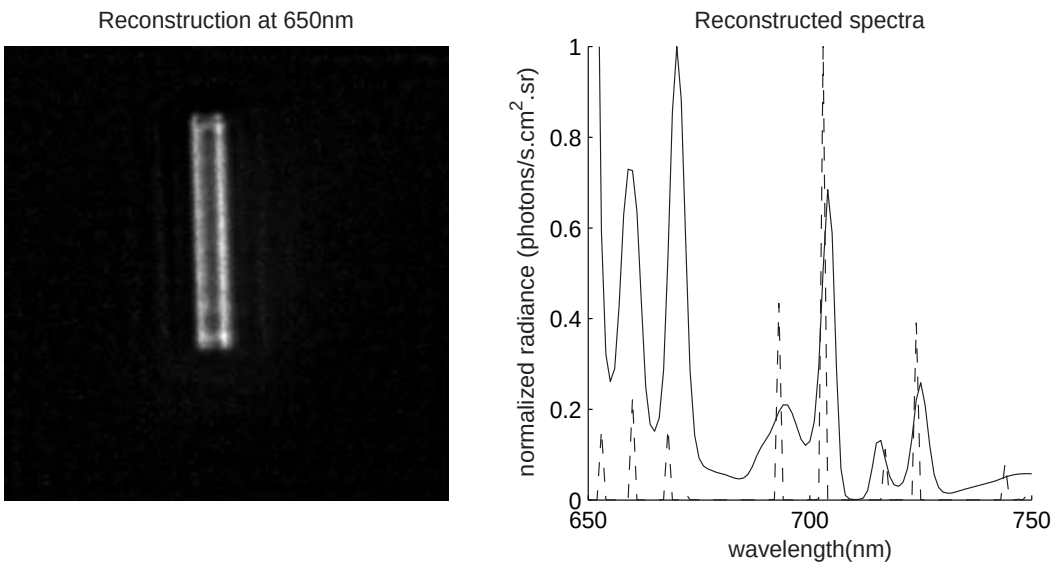

Figure 6.7: Reconstruction of the collected Ne source. The dashed lines represent the location and amplitudes of the spectra of the Ne source.

error. The 667nm feature was reconstructed at 670nm for a 3nm inaccuracy. The 1nm difference is consistent with the simulation of the Ne reconstruction.

While the 5nm sampling improves the spectral accuracy, the sampling is still not fine enough to reconstruct the spectral amplitudes. Figure 6.7 shows two differences between the reconstruction and the spectra. For wavelengths greater than 675nm, the amplitude ratios of the closely spaced features are lower than the spectra. The lower ratios are due to the same spectral blurring and reconstruction that occurred with the Hg(Ar) source. For wavelengths lower than 675nm, there is an additional error with the reconstruction amplitudes; the 653nm, 660nm and 667nm spectral feature amplitudes are also higher than expected.

As Figure 5.7 showed, these feature amplitudes in the simulation were much closer to the spectra. There are three potential reasons for the higher than expected results for the features in the data. The first is an error with the MBSIR algorithm. This is not considered to be the error given the success of the algorithm for the visible data and the higher wavelengths in the near-IR data. The second potential error is the spectra of the Ne source used is incorrect. This is also not considered to be the

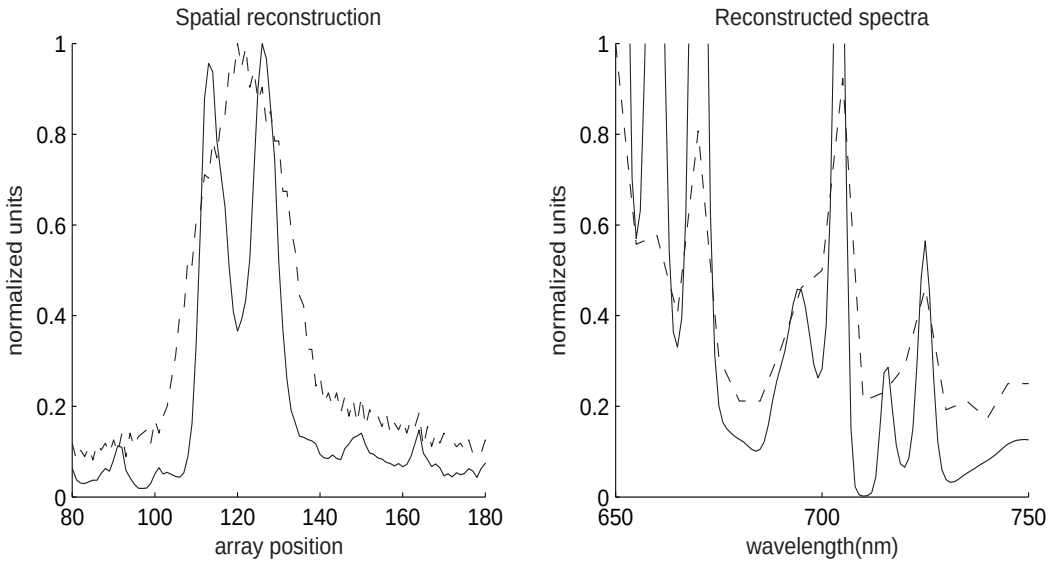

Figure 6.8: Demonstration of the non-resolved to resolved spatial and spectral profile of the Ne source. The solid lines represent the cross-section of the reconstructed image and the spectra of the reconstruction, while the dashed lines are the cross-section and spectra of the image.

error since the Ne spectra was measured with a spectrometer. The third possible error is that the spectral radiometry part of the ASIR-TB sensor model is incorrect for wavelengths between 650nm and 675nm. This is the most likely cause for the high amplitudes for the three features. To resolve this error, the spectral throughput of the ASIR-TB sensor needs to be more accurately measured.

6.2.3 ASIR-TB Data Results. As the results in the previous sections show, the MBSIR algorithm was able to improve the resolution of data collected with ASIR-TB. The results of the algorithm applied to the data from ASIR-TB are similar to the results expected from the simulations, with the exception of the 650nm to 675nm wavelengths of the Ne reconstruction. While the algorithm did not perfectly reconstruct the spectral scene, it does resolve both spatial and spectral features that were not resolvable in the collected data. The accuracy of the placement and amplitudes of the spectral features is strongly dependent on the sampling used when collecting the data.

6.3 ASIS

Although many test data sets were collected during the construction of ASIS, few of the data sets are complete enough to be processed with the MBSIR algorithm. Most of the data sets were collected with parameter settings useful for sensor check-out, but not for reconstruction. The data showing the most promise for applying the MBSIR are singlet stars.

Many of the data collections occurred during nights with poor seeing conditions, leading to a fair amount of atmospheric blurring even with the AO system active. Without knowing the exact atmospheric blurring, a spatial and spectral reconstruction is very difficult. The unknown spatial blurring due to the atmosphere prevents the algorithm from reconstructing the spatial scene. Since the spatial scene cannot be reconstructed, the algorithm cannot process a closely spaced binary, where the spectra of the binary star pair will be overlapping. However, singlet stars can be processed with a spectral only reconstruction.

6.3.1 Singlet Star. The singlet star, Harvard Reserve (HR) 1156, also know as Merope, is a B-Class star in the Pleiades of Taurus. The large star, estimated to be 14,000K, is 385 light years from Earth, and is 4.3 times larger than the sun [29]. Merope was collected in September 2005 with a dual-channel visible scan from 420nm to 650nm with a 5nm filter sampling. Figure 6.9 shows an image of Merope at 600nm, where the atmospheric effects are easily seen. To remove the unknown spatial effects of the atmosphere, all of the photons above the background noise were summed together in each image of the spectral cube and were placed in a single pixel. This has the effect of artificially forcing a perfect spatial reconstruction and allows for a spectral only reconstruction to be preformed on the resultant spectra. Figure 6.10 shows the collected spectra of Merope with the spatial blurring removed.

6.3.2 Singlet Star Reconstruction. The spectra shown in Figure 6.10 was processed with the 1st-order model of ASIS. The 1st-order model was used because

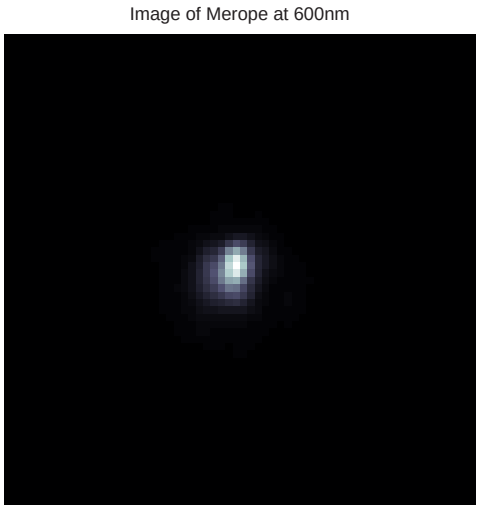

Figure 6.9: Image of the singlet star Merope (HR1156) at 600nm. The unknown atmospheric blurring is evident in the non-uniform shape of the star.

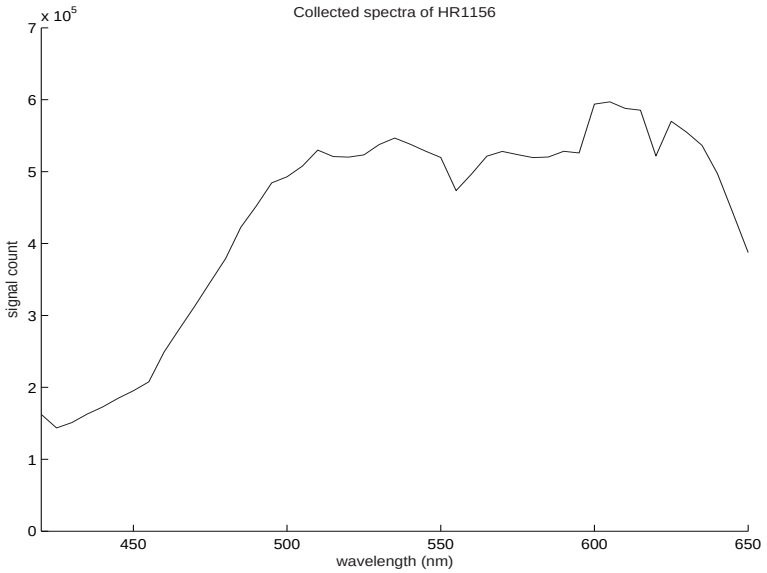

Figure 6.10: Collected spectra of Merope (HR1156) in the visible.

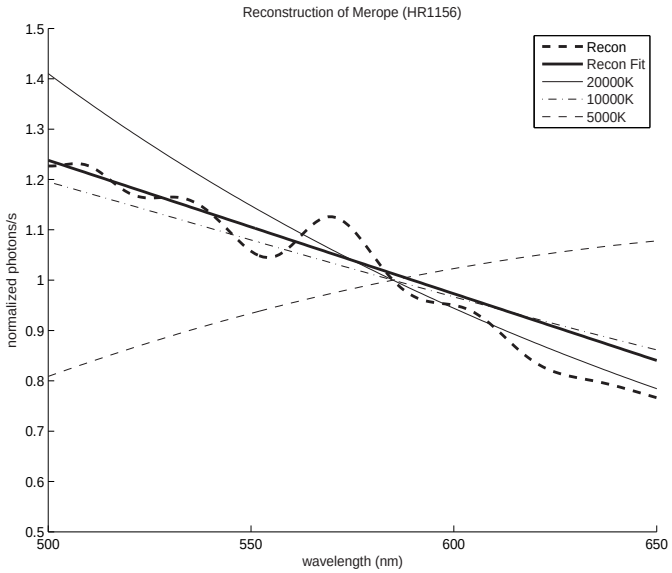

Figure 6.11: Normalized spectra reconstruction of Merope (HR1156), a B class star. While a lack of calibration prevents a complete application of the spectral only reconstruction algorithm, a normalized reconstruction shows that reconstructed spectra matches the normalized blackbody curve for a star between 10,000K and 20,000K.

the data was collected when ASIS was in an initial configuration for sensor check-out. The calibration that occurred after ASIS was in a more complete configuration is not applicable to this data. Since a full calibration of ASIS has not been accomplished, the results of the spectral only reconstruction are normalized to 600nm. The result of the reconstruction is shown in Figure 6.11. In the figure, the reconstruction is compared to the normalized blackbody curves of 5,000K, 10,000K, and 20,000K stars. Since every blackbody curve has a unique shape, an approximate spectra match can be accomplished by matching the shape of the reconstruction to the shape of the normalized blackbody curve. This is done by fitting a 2nd order polynomial to the reconstruction and matching it to the blackbody curves. As seen in Figure 6.11, the reconstruction matches a bright B or O class star, with a temperature between 10,000K and 20,000K. Further analysis of the reconstructed spectra indicates that the star has a temperature of 10,750K.

6.4 Summary

This chapter demonstrated that the MBSIR algorithm improves the resolution of spectral data. The improvement in the resolution was similar to those seen in the simulation of the last chapter. The most obvious example of the resolution improvement was seen in the application of the algorithm to images collected of spectral sources with the ASIR-TB sensor. Both the spatial and spectral resolution of the Hg(Ar) source in the visible and the Ne source in the near-IR were improved. In the initial data, neither the filaments or some spectral features were resolvable. After the algorithm was applied to the data, the filaments and features were resolvable.

While much of the ASIS data is not suitable for processing with the MBSIR algorithm, some of the singlet star data showed promising results. The unknown spatial blurring prevented a full MBSIR processing on the data. However, when the data was pre-processed to allow a spectral only reconstruction, the results matched what would be expected. Since ASIS is not is its final configuration, a full calibration of the system has not been accomplished. Therefore, the results cannot give a full radiometric reconstruction. But, the normalized results of the reconstruction do match the unique normalized shape of the blackbody curve of the estimated temperature of the star. This indicates that the MBSIR algorithm is not giving completely erroneous results and is showing some promise.

A natural next step is to ask how well the MBSIR algorithm could improve the spectral data collected with ASIS. To help quantify this answer, the lower bounds on the algorithm performance will be calculated.

VII. Bounding Algorithm Performance

The Cramér-Rao Lower Bound (CRLB) is one measure to how well the MBSIR algorithm performs [49]. Two CRLBs will be examined in this chapter. The first is the bound on spectral resolution and the second is the bound on the spectral accuracy. The spectral resolution lower bound examines the best possible spectral resolution that data processed with MBSIR can achieve. The spectral accuracy lower bound measures the limit of the ability of the MBSIR algorithm to reconstruct a spectral feature at the correct wavelength.

For the resolution CRLB, the calculated lower bound will be compared to the resolution for ASIR-TB and ASIS. The resolution is determined through simulation and represents the minimum distance two spectral features can be separated so that the features are resolved after processing with the MBSIR algorithm. A similar comparison is also made for the spectral accuracy lower bound. For this case, the accuracy lower bound is compared to the simulated spectral accuracy for both ASIR-TB and ASIS.

The CRLBs calculated in this chapter are the ultimate lower bounds for the spectral resolution and accuracy. The lower bound will be calculated by estimating the spectra at only two wavelengths for the spectral resolution and at only one wavelength for the spectral accuracy. When the CRLBs are compared to the simulations, the CRLBs may be significantly lower than the simulated performance. The main reason for this potential difference is the way the simulation was run. In the simulation, the spectra was estimated for all of the visible and near-IR wavelengths. A simulation that estimates the spectra at all wavelengths will have decreases performance over a simulation that only estimates the spectra at a few wavelengths. However, simulating the resolution and accuracy by estimating the spectra at all wavelengths represents a more realistic application of the MBSIR algorithm. Therefore, the comparison between the CRLBs and the realistic simulations will be made, but it is with the possibility that the CRLBs may be significantly lower. However, the CRLBs will still provide insight on the performance of the algorithm.

For the bounds examined in this section, only the spectral portion of the MBSIR algorithm is used. This can be done since the spatial and spectral parts of the MBSIR algorithm can be separated. Looking at the spectral only bounds provides a cleaner way to examine the improvement in spectral resolution.

7.1 Balancing Imaging Time and Algorithm Performance

For ASIS, the CRLB can be used to balance the performance of the MBSIR algorithm with the time required to collected a spectral image. Because ASIS was designed to collected spectral images of satellites in orbit, it has a limited amount of time to collect the spectral image. The amount of time depends on several factors, including the altitude and elevation of the satellite, and the sun illumination angle. In general, ASIS needs to complete the collection of the spectral image before the aspect of the satellite toward the sensor changes significantly. The amount of time before a significant change in aspect is usually several seconds for low altitude satellites, to several minutes for the high altitude satellites.

Since ASIS uses LCTFs to collect the spectral image, care must be taken in the setting of the filter sampling. The filter sampling is the number of selected center wavelength that will be used to crete the spectral image. The LCTFs have a 50ms nominal switching time. Therefore, each selected center wavelength will take 50ms plus the integration time of the imaging arrays. Using a typical integration time of 200ms, the image from each center wavelength setting takes approximately 250ms. One way to select the filter sampling is to estimate the time that the satellite will present the same aspect to the sensor, then determine how many center wavelength settings can be accomplished in that interval.

Another method to determine the filter sampling is to look at the CRLB and determine the point at which finer filter sampling leads to little increased performance of the MBSIR algorithm. Instead of simply basing the sampling on the amount of estimated time available, using the CRLB allows a quantifiable approach to selecting the filter sampling. For this method, the total signal collected for the different filter

samplings will be kept constant. The constant collected signal is the same as fixing the imaging time for each CRLB calculation. This allows for a fair comparison of the bounds determined for each sampling. The constant signal collection will be done by increasing the signal received in the coarser samplings as compared to finer filter samplings. This method will be investigated further after looking at the CRLBs in each of the following two sections.

7.2 Cramér-Rao Bound for Spectral Resolution

The first CRLB of interest is the lower bound on the spectral resolution. This CRLB calculates the best possible spectral resolution improvement the MBSIR algorithm can achieve. The CRLB for spectral resolution provides a statistical representation for the resolvability of different spectral features. The CRLB will determine the variance of the estimated distance between the two features when the MBSIR algorithm is applied. When this variance, or uncertainty, in the distance between the two features is equal to the distance between the two features, the features are not resolvable.

This is an important bound since it gives a measure of the spectral resolution improvement the MBSIR algorithm can provide. Figures 7.1 and 7.2 give a simulated example of the spectral resolution improvement the MBSIR algorithm provides over unprocessed spectral images from ASIS. In the Figure 7.1, the spectral features are unresolvable. In Figure 7.2, the same features are resolvable when the MBSIR algorithm is applied. The purpose of the spectral resolution CRLB is to determine the minimum distance between two spectral features such that the features are resolvable after processing with the algorithm. When the MBSIR algorithm is applied to the data from the sensor, it may or may not come close to meeting this bound, but on average, it should never be expected to exceed this bound. Therefore, the spectral resolution bound gives a quantitative measure of the best possible spectral resolution improvement the algorithm will provide when used to post-process the data.

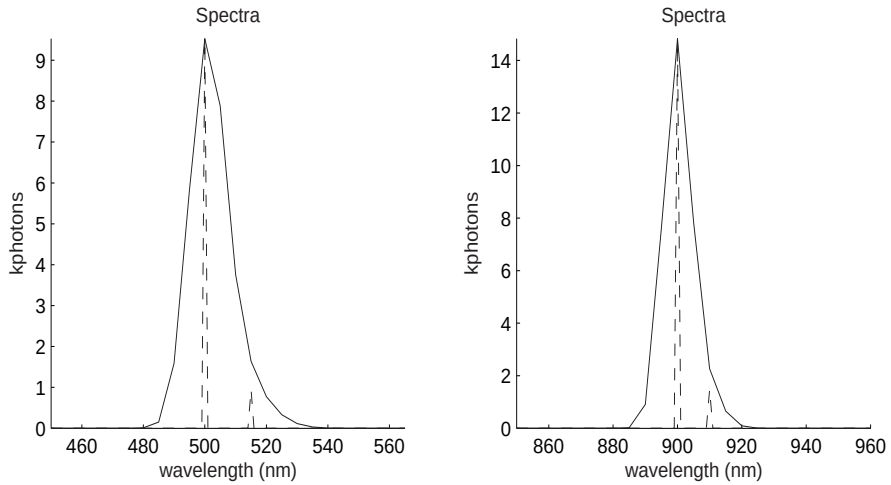

Figure 7.1: Simulated spectral output of ASIS for two spectral feature at 500nm and 515nm in the VIS and 900nm and 910nm in the NIR. These spectral features are unresolvable.

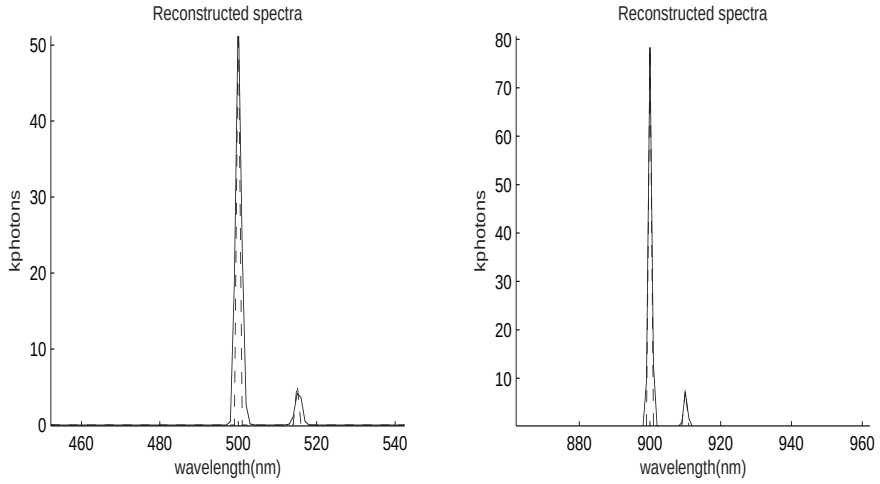

Figure 7.2: Reconstruction of simulated spectral output for two spectral feature at 500nm and 515nm in the VIS and 900nm and 910nm in the NIR. The MBSIR algorithm has made the features spectrally resolvable.

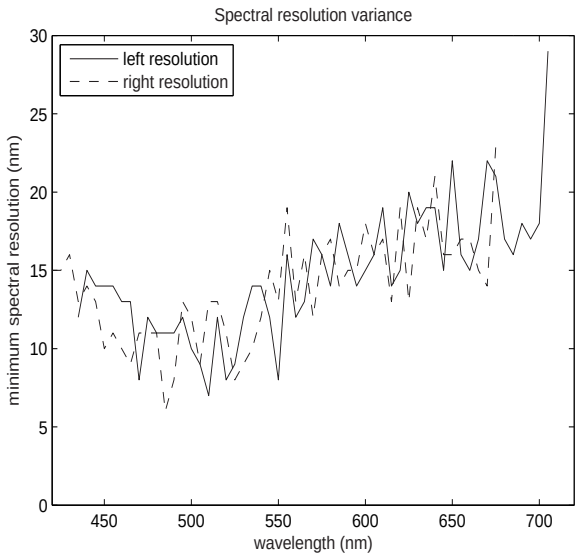

Figure 7.3: Example of the difference in the left and right spectral resolutions. The difference is caused by the spectrally variant ETFs used in ASIS and ASIR-TB.

7.2.1 Left vs. Right Resolution. Since the spectral blurring for ASIS and ASIR-TB is variant, there are actually two spectral resolutions for each wavelength. The spectral resolution to the right of the feature and the left of the feature are slightly different. Figure 7.3 shows an example of the difference in the left and right spectral resolutions. The figure shows what the simulated minimum resolution is for two spectral features collected with ASIS and then processed with the MBSIR algorithm. The first spectral feature was placed at the wavelength corresponding to the wavelength on the x-axis. The second feature was placed to the left to get the left resolution, and then to the right to get the right resolution.

Either the left or the right resolution can be used for this chapter since Figure 7.3 shows both resolutions are similar. Since normal convention is to read from left to right, the second feature will be assumed to be the right of the first feature. This leads to a right spectral resolution being used for this chapter.

7.2.2 Spectral Resolution CRLB. Since each element of the true spectral scene is estimated with the ML Bayesian estimator, the bound on the estimator will be a non-random multiple parameter bound. The bound on the variance of the

estimator, that is the difference of the estimated value, $\hat{a}_i(R)$, from the true value, A_i, will be determined by the diagonal of the inverse of the Fisher information matrix, $F_{i,j}$, according to [49],

$$Var[\hat{a}_i(R) - A_i] \geq F_{i,j}^{-1}. \tag{7.1}$$

Where the entries in the information matrix will be given by,

$$F = -E[\frac{\partial^2}{\partial \alpha^2}(ln(P[d(x_o, y_o, \lambda_o) = D(x_o, y_o, \lambda_o)]))] \tag{7.2}$$

where $\alpha = [I_1, I_2, \Delta\gamma]$, the parameters of interest for this bound. For these parameters, I_1 is the intensity of the first spectral feature, I_2 is the intensity of the second spectral feature and $\Delta\gamma$ is the distance between the two features. The partial derivatives within the expected value can be expanded into a matrix where each of the entries is the second partial of two of the parameters, I_1, I_1 and $\Delta\gamma$. Expanding Equation (7.2) leads to,

$$F = -E\begin{pmatrix} \frac{\partial^2}{\partial I_1^2}ln(P) & \frac{\partial^2}{\partial I_1 \partial I_2}ln(P) & \frac{\partial^2}{\partial I_1 \partial \Delta\gamma}ln(P) \\ \frac{\partial^2}{\partial I_2 \partial I_1}ln(P) & \frac{\partial^2}{\partial I_2^2}ln(P) & \frac{\partial^2}{\partial I_2 \partial \Delta\gamma}ln(P) \\ \frac{\partial^2}{\partial \Delta\gamma \partial I_1}ln(P) & \frac{\partial^2}{\partial \Delta\gamma \partial I_2}ln(P) & \frac{\partial^2}{\partial \Delta\gamma^2}ln(P) \end{pmatrix} \tag{7.3}$$

where P is the probability given in Equation (3.7), repeated below,

$$P[d(x, y, \lambda) = D(x, y, \lambda) \forall (x, y, \lambda)] = \prod_{x,y,\lambda} \frac{i(x, y, \lambda)^{D(x,y,\lambda)}}{D(x, y, \lambda)!} e^{-i(x,y,\lambda)}.$$

Performing the partial derivatives on the entries and looking at the spectral part of the bound only, the entries in the matrix are,

$$\frac{\partial^2}{\partial I_1^2}ln(P) = \sum_{\lambda} \frac{-D(\lambda)}{i^2(\lambda)}(\frac{\partial}{\partial I_1}i(\lambda))^2 + \frac{D(\lambda)}{i(\lambda)}\frac{\partial^2}{\partial I_1^2}i(\lambda) - \frac{\partial^2}{\partial I_1^2}i(\lambda), \tag{7.4}$$

$$\frac{\partial^2}{\partial I_2^2}ln(P) = \sum_{\lambda} \frac{-D(\lambda)}{i^2(\lambda)}(\frac{\partial}{\partial I_2}i(\lambda))^2 + \frac{D(\lambda)}{i(\lambda)}\frac{\partial^2}{\partial I_2^2}i(\lambda) - \frac{\partial^2}{\partial I_2^2}i(\lambda), \tag{7.5}$$

$$\frac{\partial^2}{\partial\Delta\gamma^2}ln(P) = \sum_{\lambda}\frac{-D(\lambda)}{i^2(\lambda)}(\frac{\partial}{\partial\Delta\gamma}i(\lambda))^2 + \frac{D(\lambda)}{i(\lambda)}\frac{\partial^2}{\partial\Delta\gamma^2}i(\lambda) - \frac{\partial^2}{\partial\Delta\gamma^2}i(\lambda), \tag{7.6}$$

$$\frac{\partial^2}{\partial I_1\partial I_2}ln(P) = \sum_{\lambda}\frac{-D(\lambda)}{i^2(\lambda)}\frac{\partial}{\partial I_1}i(\lambda)\frac{\partial}{\partial I_2}i(\lambda) + \frac{D(\lambda)}{i(\lambda)}\frac{\partial^2}{\partial I_1\partial I_2}i(\lambda) - \frac{\partial^2}{\partial I_1\partial I_2}i(\lambda), \tag{7.7}$$

$$\frac{\partial^2}{\partial I_1\partial\Delta\gamma}ln(P) = \sum_{\lambda}\frac{-D(\lambda)}{i^2(\lambda)}\frac{\partial}{\partial I_1}i(\lambda)\frac{\partial}{\partial\Delta\gamma}i(\lambda) + \frac{D(\lambda)}{i(\lambda)}\frac{\partial^2}{\partial I_1\partial\Delta\gamma}i(\lambda) - \frac{\partial^2}{\partial I_1\partial\Delta\gamma}i(\lambda), \tag{7.8}$$

$$\frac{\partial^2}{\partial I_2\partial\Delta\gamma}ln(P) = \sum_{\lambda}\frac{-D(\lambda)}{i^2(\lambda)}\frac{\partial}{\partial I_2}i(\lambda)\frac{\partial}{\partial\Delta\gamma}i(\lambda) + \frac{D(\lambda)}{i(\lambda)}\frac{\partial^2}{\partial I_2\partial\Delta\gamma}i(\lambda) - \frac{\partial^2}{\partial I_2\partial\Delta\gamma}i(\lambda), \tag{7.9}$$

$$\frac{\partial^2}{\partial I_1\partial I_2}ln(P) = \frac{\partial^2}{\partial I_2\partial I_1}ln(P), \tag{7.10}$$

$$\frac{\partial^2}{\partial I_1\partial\Delta\gamma}ln(P) = \frac{\partial^2}{\partial\Delta\gamma\partial I_1}ln(P), \tag{7.11}$$

$$\frac{\partial^2}{\partial I_2\partial\Delta\gamma}ln(P) = \frac{\partial^2}{\partial\Delta\gamma\partial I_2}ln(P). \tag{7.12}$$

The Fisher matrix can be simplified to,

$$F = \begin{pmatrix} \sum_{\lambda}\frac{1}{i(\lambda)}(\frac{\partial}{\partial I_1}i(\lambda))^2 & \sum_{\lambda}\frac{1}{i(\lambda)}\frac{\partial}{\partial I_1}i(\lambda)\frac{\partial}{\partial I_2}i(\lambda) & \sum_{\lambda}\frac{1}{i(\lambda)}\frac{\partial}{\partial I_1}i(\lambda)\frac{\partial}{\partial\Delta\gamma}i(\lambda) \\ \sum_{\lambda}\frac{1}{i(\lambda)}\frac{\partial}{\partial I_2}i(\lambda)\frac{\partial}{\partial I_2}i(\lambda) & \sum_{\lambda}\frac{1}{i(\lambda)}(\frac{\partial}{\partial I_2}i(\lambda))^2 & \sum_{\lambda}\frac{1}{i(\lambda)}\frac{\partial}{\partial I_2}i(\lambda)\frac{\partial}{\partial\Delta\gamma}i(\lambda) \\ \sum_{\lambda}\frac{1}{i(\lambda)}\frac{\partial}{\partial I_2}i(\lambda)\frac{\partial}{\partial I_1}i(\lambda) & \sum_{\lambda}\frac{1}{i(\lambda)}\frac{\partial}{\partial\Delta\gamma}i(\lambda)\frac{\partial}{\partial I_2}i(\lambda) & \sum_{\lambda}\frac{1}{i(\lambda)}(\frac{\partial}{\partial\Delta\gamma}i(\lambda))^2 \end{pmatrix} \tag{7.13}$$

using,

$$-E[-D(\lambda)] = i(\lambda). \tag{7.14}$$

For this CRLB, the two spectral features in the scene will be assumed to be narrow-band Gaussian functions for mathematical convenience. Since the features need to be differentiated, using Gaussian functions greatly reduces the complexity of the math and allows for the Fisher information matrix to be invertible. With the

narrow-band Gaussian assumption as the spectra, the image produced is,

$$i(\lambda) = \sum_{\gamma} \frac{I_1}{\sigma\sqrt{2\pi}} e^{\frac{-(\gamma-\gamma_o)^2}{2\sigma^2}} h_2(\lambda,\gamma) + \sum_{\gamma} \frac{I_2}{\sigma\sqrt{2\pi}} e^{\frac{-(\gamma-(\gamma_o+\Delta\gamma))^2}{2\sigma^2}} h_2(\lambda,\gamma). \tag{7.15}$$

Equation (7.15) has the following partial derivatives needed to compute the spectral resolution CRLB,

$$\frac{\partial}{\partial I_1} i(\lambda) = \sum_{\gamma} \frac{1}{\sigma\sqrt{2\pi}} e^{\frac{-(\gamma-\gamma_o)^2}{2\sigma^2}} h_2(\lambda,\gamma), \tag{7.16}$$

$$\frac{\partial}{\partial I_2} i(\lambda) = \sum_{\gamma} \frac{1}{\sigma\sqrt{2\pi}} e^{\frac{-(\gamma-(\gamma_o+\Delta\gamma))^2}{2\sigma^2}} h_2(\lambda,\gamma), \tag{7.17}$$

$$\frac{\partial}{\partial \Delta\gamma} i(\lambda) = \sum_{\gamma} \left(\frac{-I_2}{\sigma^3\sqrt{2\pi}} + \frac{I_2(\gamma-(\gamma_o+\Delta\gamma))^2}{\sigma^5\sqrt{2\pi}}\right) e^{\frac{-(\gamma-(\gamma_o+\Delta\gamma))^2}{2\sigma^2}} h_2(\lambda,\gamma). \tag{7.18}$$

All of the above equations are combined together to compute the Fisher matrix for the spectral resolution lower bound. A lower bound on the spectral resolution can be determined by inverting this matrix and looking at the (3,3) entry of the matrix. This value will correspond to the resolution of the spectral reconstruction for the value of $\Delta\gamma$, given the spectral feature intensities, I_1 and I_2 and the spectral feature location γ_o. The spectral resolution for the sensor is then determined by allowing γ_o to be all the wavelengths of the sensor.

7.2.3 ASIR-TB Spectral Resolution. The CRLB for the spectral resolution of ASIR-TB was calculated for the same scene used to simulate the spectral sources in Chapter V. These results were then compared to the simulated minimum spectral resolution for the same source. The CRLB and the minimum spectral resolution were then compared to the actual resolved data shown in Chapter VI. Figures 7.4 and 7.5 shows the comparisons described above. Figure 7.6 gives a closer view of the lower wavelengths shown in Figure 7.5.

As expected, the calculated CRLB is lower than the minimum spectral resolution for each of the spectral sources. Additionally, the resolution of the data is greater

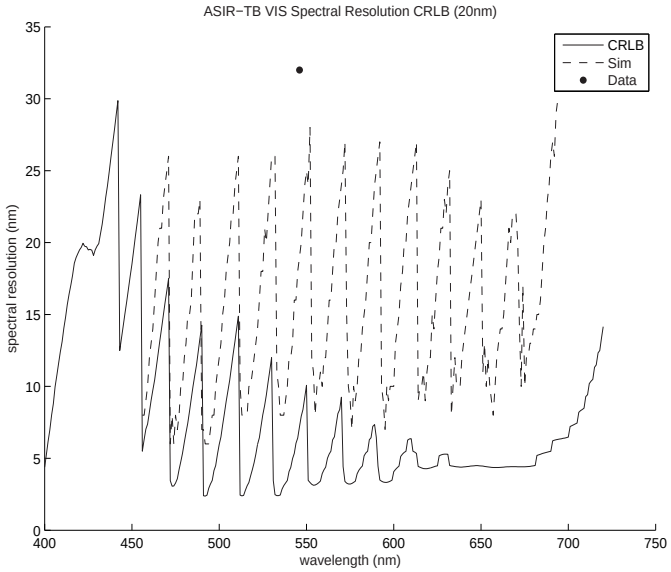

Figure 7.4: Comparison of the calculated CRLB for the spectral resolution of ASIR-TB to the simulated spectral resolution and measured spectral resolution of a Hg(Ar) source in the visible. The spectral resolution corresponds to $\Delta\gamma$ and the wavelength to γ_o in spectral resolution CRLB derivation.

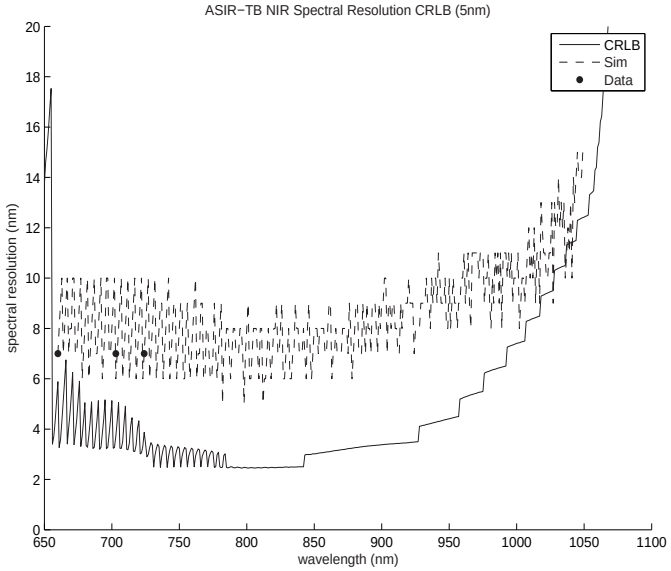

Figure 7.5: Comparison of the calculated CRLB for the spectral resolution of ASIR-TB to the simulated spectral resolution and measured spectral resolution of a Ne source in the near-IR. The spectral resolution corresponds to $\Delta\gamma$ and the wavelength to γ_o in spectral resolution CRLB derivation.

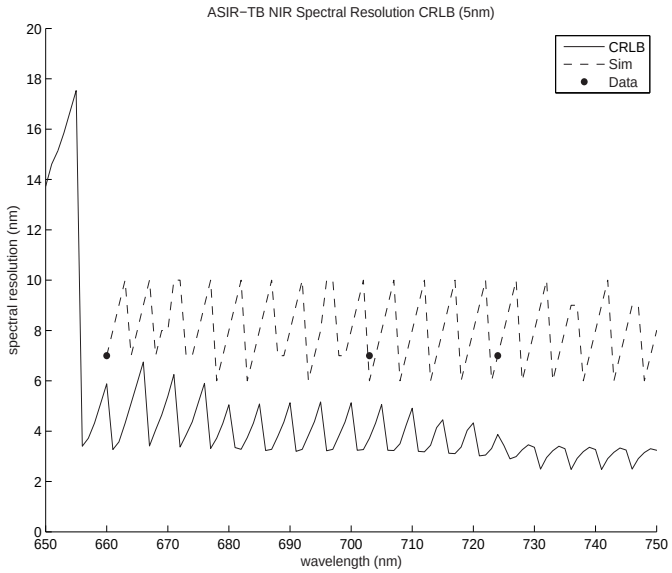

Figure 7.6: Magnified comparison of the calculated CRLB for the spectral resolution of ASIR-TB to the simulated spectral resolution and measured spectral resolution of a Ne source in the near-IR showing a close-up of the lower wavelengths. The spectral resolution corresponds to $\Delta\gamma$ and the wavelength to γ_o in spectral resolution CRLB derivation.

than the simulation. The fact that the spectral resolution of the visible data is higher than the simulated spectral resolution is expected. This is because the minimum spectral resolution is the minimum spectral separation, which is less than the spectral separation of the fixed spectral features of the sources. If the persistent lines of the sources were somehow adjustable, then the spectral lines could be moved close together and the resolved feature separation from the data could be more closely matched to the simulated minimum resolution. The data in the near-IR more closely matches the calculated spectral resolution because the spectral lines are closer to the minimum distance required for resolvability.

The coarse 20nm and 5nm visible and near-IR filter sampling cause the oscillations in the CRLBs in Figures 7.4 and 7.5. The coarse sampling leads to a lack of shared spectral information between successive images. When the wavelength for which the spectral resolution is being calculated is close to a center wavelength of the filter sampling, the spectral resolution increases. The spectral resolution decreases

when the wavelength for which the spectral resolution is being calculated moves away from the sampled filter wavelengths. This in turn leads to an increasing and decreasing spectral resolution cycling as the selected center wavelengths in the filter sampling coincide with the wavelengths in the x-axis. The oscillations are reduced at the higher wavelengths, where the larger bandwidths increase the amount of shared information between the successive images. Both the visible and near-IR CRLBs decrease at the higher wavelengths. For the visible, the decreased resolution occurs when the CRLB is calculated for features at wavelengths higher then the maximum selected filter setting of 700nm. At wavelengths over 700nm, there are no successive images to share the spectral information and the resolution decreases. For the near-IR, the signal reduction is due to the low quantum efficiency of the imaging array at wavelengths higher than 950nm. As the signal is reduced, the spectral resolution decreases. This is because the lower signal provides less information required to resolve the features.

7.2.4 ASIS Spectral Resolution. A comparison similar the one for ASIR-TB was done for ASIS, except no data points are available for comparison. Additionally, instead of the scene of the spectral sources, two spectral features of the same intensity were used as the spectral scene. These features provided for a SNR of 30. Figures 7.7 and 7.8 show the lower bound for the spectral resolution of a 10nm filter sampling in the visible and 5nm sampling in the near-IR. Each of these bounds is compared to the simulated spectral resolution. As with the ASIR-TB bounds, the CRLB is lower than the simulated spectral resolutions.

The CRLBs for ASIS do not show the same amount of oscillations seen in the ASIR-TB CRLBs, because a finer filter sampling is used for the ASIS CRLB calculation. The ASIS CRLBs do show the same decrease in the resolution due to the reduced signal. This can be seen in the near-IR CRLB shown in Figure 7.8. The signal in the lower wavelengths of the figure is reduced because of the dichroic located at 700nm. The signal reduction at the higher wavelengths is due to the low quantum

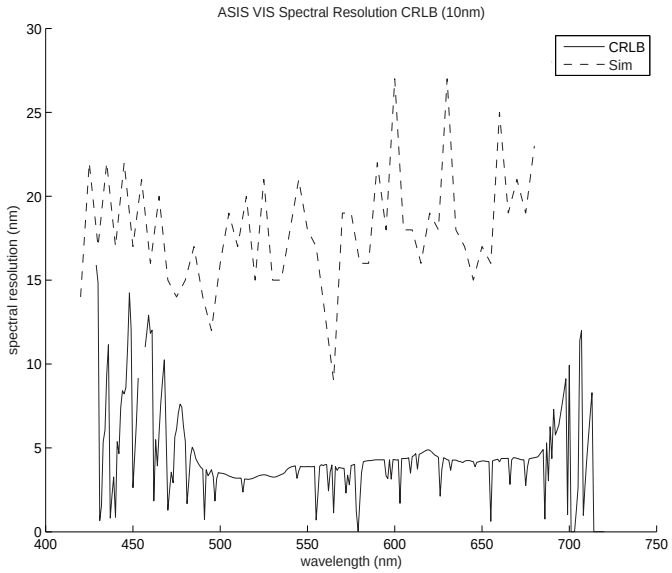

Figure 7.7: Comparison of the calculated CRLB for the spectral resolution of ASIS to the simulated spectral resolution for the visible.

efficiency of the imaging array above 1000nm. The visible CRLB in Figure 7.7 also shows the effect of the reduced signal due to the dichroic located at 700nm.

The spectral resolution lower bound can be used to aid in determining the most efficient filter sampling to achieve the optimal resolution versus imaging time. In Figure 7.9, the average spectral resolutions for the CRLB is shown for different filter samplings in the visible wavelengths. In the figure, each data point represents the CRLB averaged across the visible wavelengths, where the CRLB is calculated for the filter sampling given in the x-axis. A least-squares polynomial line was then fit to the data points of the calculated spectral resolution CRLBs. The trend line shows that a filter sampling of less than 5nm will not substantially improve the resolution of the post-processed ASIS data. Limiting the filter sampling to 5nm, instead of using the finest sampling of 1nm, will decrease the image collection time by 500% while achieving almost the same post-processed spectral resolution.

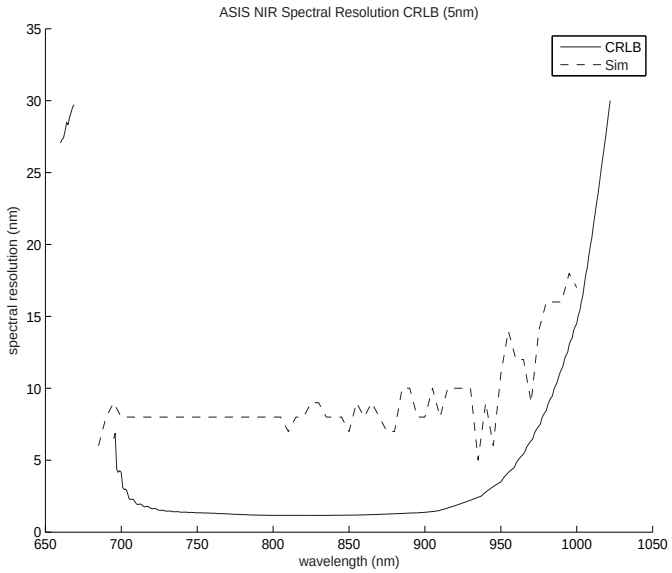

Figure 7.8: Comparison of the calculated CRLB for the spectral resolution of ASIS to the simulated spectral resolution for the near-IR.

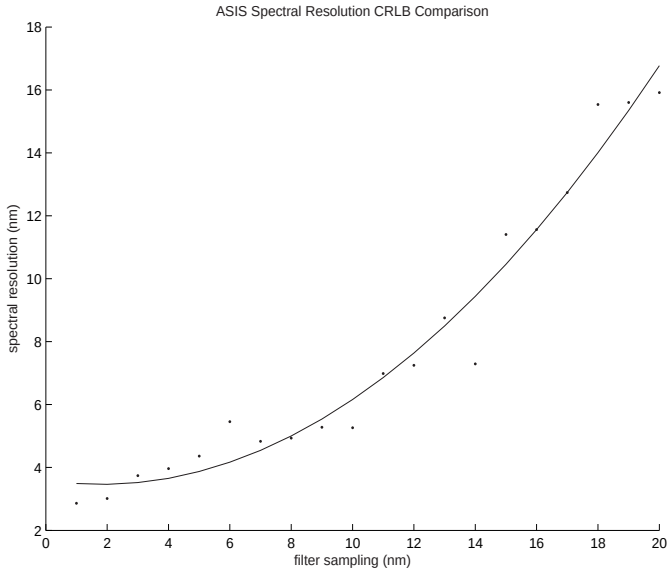

Figure 7.9: The effect of finer filter sampling to the calculated spectral resolution CRLB for the visible wavelengths of ASIS. The points are the calculated average CRLB for the visible wavelengths and the line a trend fit to the data.

7.3 Cramér-Rao Lower Bound for Spectral Accuracy

The second CRLB of interest is the lower bound on spectral accuracy. This bound determines the accuracy of the MBSIR algorithm; measuring how well the algorithm reconstructs a spectral feature at the correct wavelength. It is important to not only resolve the spectral features, but also to resolve the features at the correct wavelength.

7.3.1 Spectral Accuracy CRLB. The spectral accuracy CRLB is similar to the spectral resolution CRLB. However, instead of calculating the variance of the minimum resolved distance between two features, the variance in the location of one feature is determined. The CRLB for spectral accuracy starts the same as the spectral resolution CRLB, except the Fisher matrix is reduced by one parameter since only one spectral feature is needed,

$$F = -E[\frac{\partial^2}{\partial^2 \alpha}(ln(P[d(x_o, y_o, \lambda_o) = D(x_o, y_o, \lambda_o)]))] \tag{7.19}$$

where $\alpha = [\gamma_o, I_o]$ are the parameters of interest in this bound. These parameters correspond to the accuracy of the spectral reconstruction for the value of γ_o, given spectral feature intensity, I_o. Expanding this and looking only at the spectral part leads to,

$$F = -E \begin{pmatrix} \frac{\partial^2}{\partial \gamma_o^2} ln(P) & \frac{\partial^2}{\partial \gamma_o \partial I_o} ln(P) \\ \frac{\partial^2}{\partial I_o \partial \gamma_o} ln(P) & \frac{\partial^2}{\partial I_o^2} ln(P) \end{pmatrix} \tag{7.20}$$

where P is the probability given in Equation (3.7).

Preforming the partial derivatives the entries in the matrix become,

$$\frac{\partial^2}{\partial I_o^2} ln(P) = \sum_{\lambda} \frac{-D(\lambda)}{i^2(\lambda)} (\frac{\partial}{\partial I_o} i(\lambda))^2 + \frac{D(\lambda)}{i(\lambda)} \frac{\partial^2}{\partial I_o^2} i(\lambda) - \frac{\partial^2}{\partial I_o^2} i(\lambda), \tag{7.21}$$

$$\frac{\partial^2}{\partial \gamma_o^2} ln(P) = \sum_{\lambda} \frac{-D(\lambda)}{i^2(\lambda)} (\frac{\partial}{\partial \gamma_o} i(\lambda))^2 + \frac{D(\lambda)}{i(\lambda)} \frac{\partial^2}{\partial \gamma_o^2} i(\lambda) - \frac{\partial^2}{\partial \gamma_o^2} i(\lambda), \tag{7.22}$$

$$\frac{\partial^2}{\partial\gamma_o\partial I_o}ln(P) = \sum_{\lambda}\frac{-D(\lambda)}{i^2(\lambda)}\frac{\partial}{\partial\gamma_o}i(\lambda)\frac{\partial}{\partial I_o}i(\lambda) + \frac{D(\lambda)}{i(\lambda)}\frac{\partial^2}{\partial\gamma_o\partial I_o}i(\lambda) - \frac{\partial^2}{\partial\gamma_o\partial I_o}i(\lambda), \quad (7.23)$$

$$\frac{\partial^2}{\partial I_o\partial\gamma_o}ln(P) = \frac{\partial^2}{\partial\gamma_o\partial I_o}ln(P). \quad (7.24)$$

Using Equation 7.14, the Fisher matrix can be simplified to,

$$F = \begin{pmatrix} \sum_{\lambda}\frac{1}{i(\lambda)}(\frac{\partial}{\partial\gamma_o}i(\lambda))^2 & \sum_{\lambda}\frac{1}{i(\lambda)}\frac{\partial}{\partial\gamma_o}i(\lambda)\frac{\partial}{\partial I_o}i(\lambda) \\ \sum_{\lambda}\frac{1}{i(\lambda)}\frac{\partial}{\partial I_o}i(\lambda)\frac{\partial}{\partial\gamma_o}i(\lambda) & \sum_{\lambda}\frac{1}{i(\lambda)}(\frac{\partial}{\partial I_o}i(\lambda))^2 \end{pmatrix} \quad (7.25)$$

For this lower bound, the spectral features in the true spectral scene are again assumed to be narrow-band Gaussian functions. For the spectral accuracy lower bound, the image is,

$$i(\lambda) = \sum_{\gamma}\frac{I_o}{\sigma\sqrt{2\pi}}e^{\frac{-(\gamma-\gamma_o)^2}{2\sigma^2}}h_2(\lambda,\gamma), \quad (7.26)$$

which has the following partial derivatives,

$$\frac{\partial}{\partial I_o}i(\lambda) = \sum_{\gamma}\frac{1}{\sigma\sqrt{2\pi}}e^{\frac{-(\gamma-\gamma_o)^2}{2\sigma^2}}h_2(\lambda,\gamma), \quad (7.27)$$

$$\frac{\partial}{\partial\gamma_o}i(\lambda) = \sum_{\gamma}\frac{I_o(\gamma-\gamma_o)}{\sigma^3\sqrt{2\pi}}e^{\frac{-(\gamma-\gamma_o)^2}{2\sigma^2}}h_2(\lambda,\gamma). \quad (7.28)$$

All of the above equations are combined together to compute the Fisher matrix for the spectral accuracy lower bound. A lower bound on the spectral accuracy at one wavelength is determined by inverting this matrix and looking at the (1,1) entry of the inverted matrix. The spectral accuracy for the sensor is then determined by stepping through all possible values of γ_o for the given feature intensity.

7.3.2 ASIR-TB Spectral Accuracy CRLB. The bound comparison described in section 7.2.3 is repeated for the spectral accuracy CRLB. The spectral accuracy CRLB is computed and is the compared to the simulated spectral accuracy. The spectral accuracy CRLB and simulated spectral accuracy are then compared to the

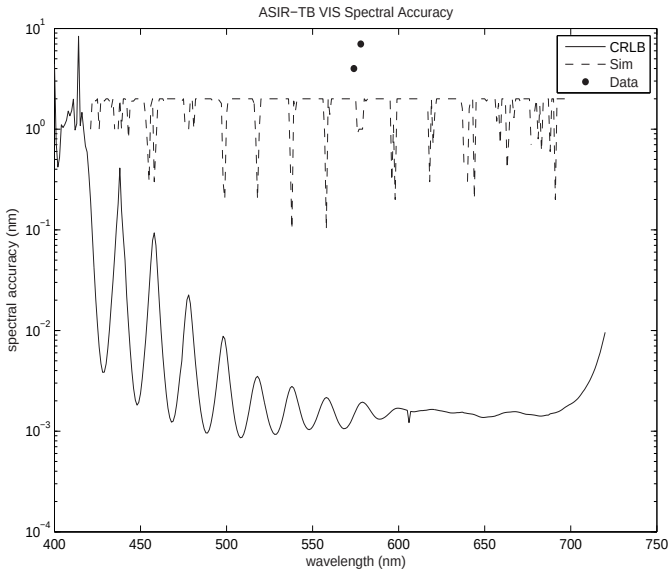

Figure 7.10: Comparison of the calculated CRLB for the spectral accuracy of ASIR-TB to the simulated spectral accuracy and measured spectral accuracy of the Hg(Ar) source in the visible.

measured accuracy from the reconstructed Hg(Ar) and Ne data. Figures 7.10 and 7.11 shows the comparisons described above.

As with the spectral resolution CRLBs, the lower bound of the spectral accuracy is lower than the calculated spectral accuracy. As first discussed in section 6.2.1.2, the accuracy of the Hg(Ar) reconstruction, shown in Figure 7.10 is worse than the simulated accuracy because of the coarse 20nm filter sampling and the selected center wavelengths for the filter. The reconstructed Ne data accuracy, shown in Figure 7.11, is closer to the calculated accuracy because of the finer 5nm filter sampling.

In both Figures 7.10 and 7.11 the difference in the CRLB and the simulation discussed in the introduction of this chapter is clearly noticeable. The CRLB for the spectral accuracy is several orders of magnitude lower than the simulated spectral accuracy. Additionally, for both cases, the calculated spectral accuracy CRLBs are different from the simulated accuracy because of the fidelity of the simulation. In simulating the spectral accuracy, the accuracy was limited to 0.1nm because of the processing time required for the simulation. This limit prevents some of the data points from be closer to the calculated lower bound.

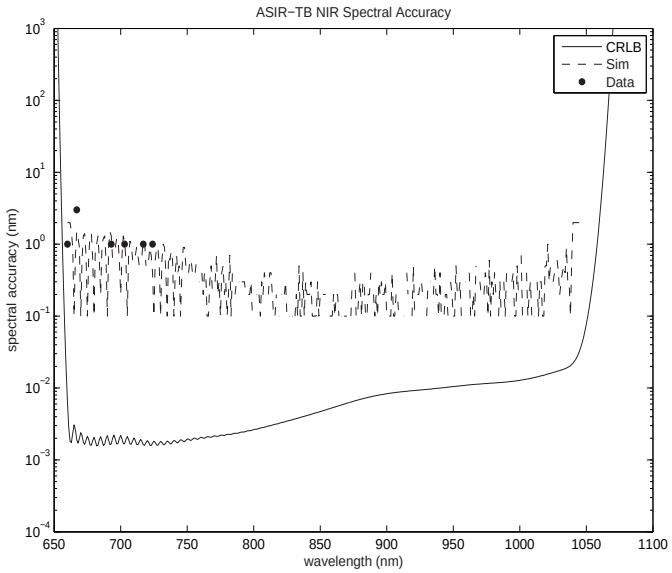

Figure 7.11: Comparison of the calculated CRLB for the spectral accuracy of ASIR-TB to the simulated spectral accuracy and measured spectral accuracy of the Ne source in the near-IR.

7.3.3 ASIS Spectral Accuracy CRLB. The spectral accuracy for ASIS was also computed for a 10nm sampling in the visible and a 5nm sampling in the near-IR. Figures 7.12 and 7.13 show the comparison of the CRLB and the simulated values, for the spectral accuracy.

Similar to the ASIR-TB spectral accuracy CRLB, the CRLB is orders of magnitude lower than the simulated accuracy. The reason for this difference is the same as discussed in the ASIR-TB section. The only difference is that the ASIS simulation was done to a 0.01nm fidelity, allowing the simulated accuracy to be closer to the calculated bound.

As with the spectral resolution lower bound, looking at the average spectral accuracy for different filter samplings provides a guideline for selecting the optimal sensor parameters to balance the performance of the MBSIR algorithm with the required imaging time. Figure 7.14 shows the average lower bound on the spectral accuracy for five filter samplings with a least-square polynomial line fit to the data. As the figure shows, the algorithm will not have substantial accuracy errors with a filter sampling of less than 10nm.

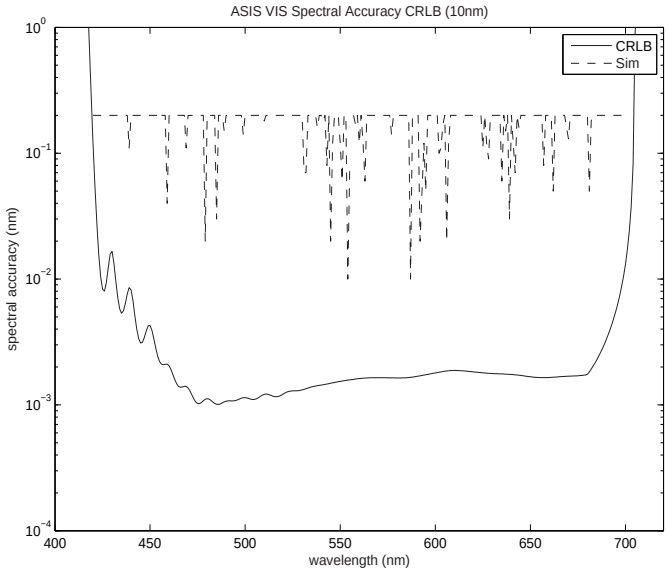

Figure 7.12: Comparison of the calculated CRLB for the spectral accuracy of ASIS to the simulated spectral accuracy in the visible.

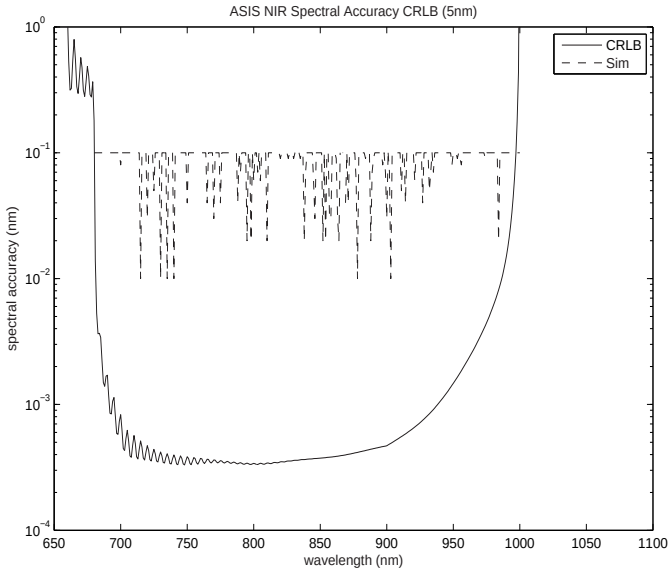

Figure 7.13: Comparison of the calculated CRLB for the spectral accuracy of ASIS to the simulated spectral accuracy in the near-IR.

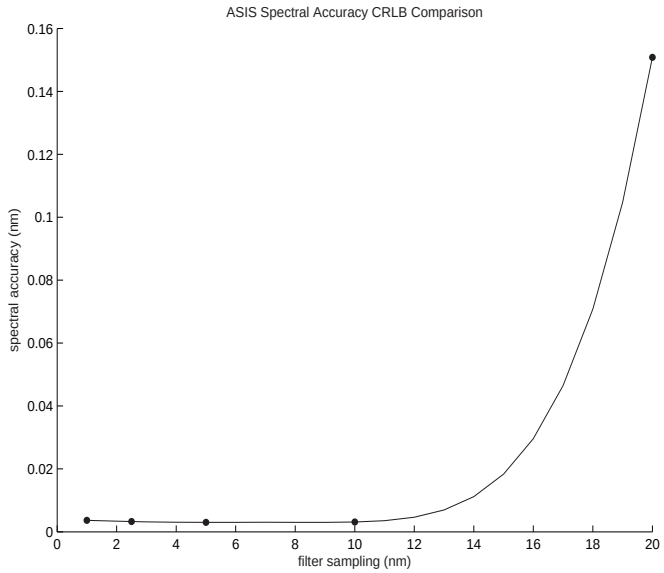

Figure 7.14: The effect of finer filter sampling to the calculated spectral accuracy CRLB for the visible wavelengths of ASIS. The points are the calculated CRLB and the line a trend fit to the data.

7.4 Summary

This chapter developed two lower bounds on the performance of the MBSIR algorithm. The spectral resolution and accuracy lower bounds are critical measurements in determining how well the algorithm improves the spectral resolution of an image. The spectral resolution lower bound measures the minimum resolvable distance between two spectral features. The spectral accuracy lower bound measures the accuracy in the location of the reconstructed spectral feature. These lower bounds were calculated for both of the ASIR-TB data collections, and compared well with the simulated and measured resolution and accuracy. The bounds for ASIS were also calculated. While the bounds were used to calculate the filter sampling that balances the performance of the MBSIR algorithm and imaging time, there is no ASIS data for comparison.

In the next chapter, these lower bounds will be used to compute a performance metric for the algorithm. This metric can be used to compare the benefits of the MBSIR algorithm on different sensors and can provide a quantitative way to select

key sensor design parameters to get the maximum benefit from the MBSIR post-processing.

VIII. Algorithm Performance Metrics

A measure of the spectral image reconstruction performance, known as the Spectral Reconstruction Capability Metric (SRCM), can be found by looking at the calculated lower bounds for the spectral accuracy and resolution of the ASIS image reconstruction. When comparing different spectral reconstruction algorithms, the better spectral reconstruction algorithm would provide: 1) the highest spectral resolution, and 2) the highest spectral accuracy.

This chapter will develop a set of SRCMs for the MBSIR algorithm and ASIS, from the spectral resolution and accuracy lower bounds. Then the SRCMs will be determined for ASIS using the 10nm and 5nm bounds calculated in the last chapter. The chapter will also discuss how the SRCM can be used.

8.1 Spectral Reconstruction Capability Metric

A set of SRCMs can be derived for the reconstruction algorithm. The first is a measure of the algorithm SRCM per spectral wavelength. This SRCM is calculated by inverting the product of the lower bound on the spectral reconstruction and accuracy for each corresponding wavelength, or

$$SRCM(\lambda) = (CRLB_{res}(\lambda)CRLB_{acc}(\lambda))^{-1}[nm^{-2}]. \tag{8.1}$$

Since smaller values of spectral accuracy and resolution represent better performance, inverting the product of these two leads to a SRCM with the larger value having the better the performance. The maximum $SRCM(\lambda)$ can then be found by looking at the highest value across the wavelengths and an average $SRCM(\lambda)$ can be found by taking the average value across the wavelength range, or,

$$SRCM_{max} = max(SRCM(\lambda))[nm^{-2}], \tag{8.2}$$

$$SRCM_{mean} = mean(SRCM(\lambda))[nm^{-2}]. \tag{8.3}$$

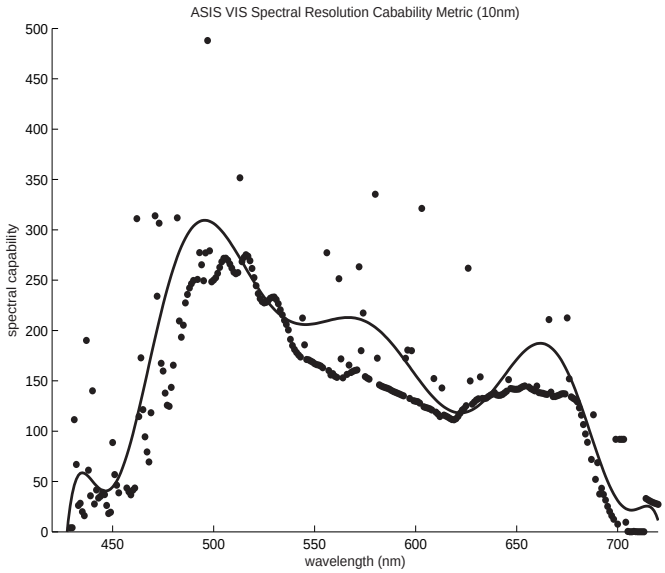

Figure 8.1: The Spectral Resolution Capability in the visible for the 10nm filter sampling. A least-squares polynomial is fit to the data points of the calculated SRCM.

With these performance measures, an assessment can be made between different spectral reconstruction algorithms and spectral sensors.

8.2 ASIS Spectral Resolution Capability Metric

Figure 8.1 and 8.2 shows the SRCM for the MBSID algorithm with the ASIS system for the 10nm and 5nm filter samplings in the visible and near-IR respectively. A least-squares polynomial was fit to both sets of data to smooth out the numerous discontinuities present in the spectral resolution and accuracy lower bounds. The discontinuities are due to the oscillatory nature of the resolution and accuracy lower bounds and occur when the oscillating minimums in the lower bounds align. For the visible, the maximum SRCM is 488 and the average SRCM is 163. In the near-IR, the maximum SRCM is 2586 and the average SRCM is 1184. The near-IR SRCM is approximately 7 times better than the visible. This is because the near-IR has a smaller bandwidth, allowing for the near-IR to have a lower spectral resolution and higher spectral accuracy. However, the smaller bandwidth allows fewer photons to the imaging array, leading to a lower SNR or longer integration times.

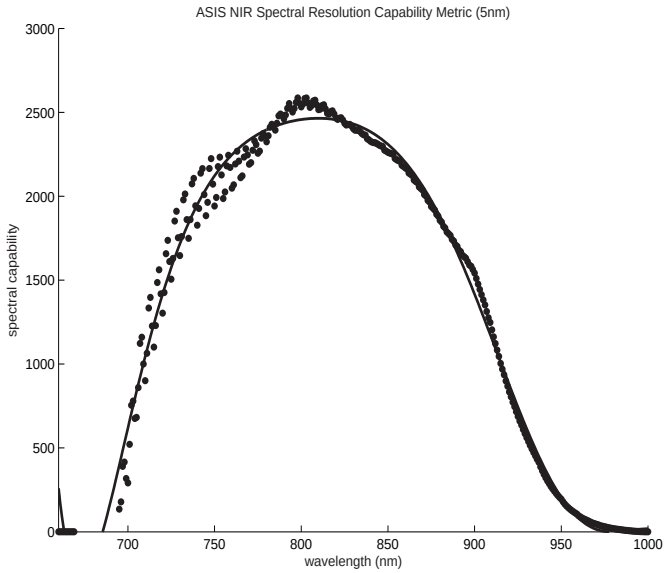

Figure 8.2: The Spectral Resolution Capability in the near-IR for the 5nm filter sampling. A least-squares polynomial is fit to the data points of the calculated SRCM.

8.3 Using the Spectral Resolution Capability Metric

There are two uses for the SRCM. The first is as a way to balance sensor settings with operational requirements. The second is a way to compare different sensor trade-offs.

8.3.1 Effective Filter Sampling. As seen in the last chapter, the lower bounds could be used to determine an effective filter sampling. An effective filter sampling is the coarsest filter sampling that provides the desired resolution improvement, while maintaining spectral accuracy. By using a coarser filter sampling, the image can be collected in a shorter amount of time when compared to a finer filter sampling. However, the resolution of the image will not suffer because the image will be processed with the MBSIR algorithm. So the effective filter sampling allows for shorter imaging time to spectrally image a non-stationary object, and still achieve the desired resolution by using the MBSIR algorithm.

The SRCM combines the separate resolution and accuracy effective filter samplings into one overall measurement. By calculating the SRCM for different filter

samplings an optimum sampling can be determined that will allow for the most effective use of the sensor. Figure 8.3 shows the calculated SRCM for ASIS in the visible for filter samplings of 1nm, 2.5nm, 5nm, 10nm, and 20nm. The figure shows that the SRCM increases as the filter sampling gets finer, for the shorter wavelengths, but the 2.5nm SRCM is better than the 1nm at longer wavelengths. This is due to the constant signal collection constraint used when the spectral resolution and accuracy lower bounds were calculated. The 2.5nm filter sampling collects the spectral cube at a higher signal per filter sample than the 1nm sampling. At the shorter filter center wavelengths, the increased signal in the 2.5nm sampling does not overcome the advantage finer filter sampling advantage of the 1nm sampling. At the longer filter center wavelengths, the higher signal in the 2.5nm sampling provides better performance over the 1nm. This is because the increased bandwidth of the filter transmission at the longer center wavelengths allows the 2.5nm to match the sampling performance of the 1nm sampling.

This is verified by removing the constant signal collection constraint and relooking at the calculated lower bounds. When this is done, the 1nm filter sampling out performs the 2.5nm filter sampling at center wavelengths below approximately 570nm. At center wavelengths of over 570nm, the 2.5nm and 1nm filter samplings have the same performance. This is also seen in Figure 8.3, at approximately 570nm, the 2.5nm and 1nm filter samplings have the same SRCM. However, at center wavelengths over 600nm, the increased signal in the 2.5nm sampling, from the constant signal constraint, gives the 2.5nm filter sampling a higher SRCM.

By using the average of the SRCMs the effective filter sampling for ASIS can be determined. Figure 8.4 shows the average of the SRCMs shown in Figure 8.3 and the imaging time required for those filter settings. For the imaging time, 50ms is used as the filter transition time and 200ms is used as the integration time. While the 1nm filter setting has the highest SRCM, the SRCM is turning away from a linear increase and has an imaging time of over 1.25min. From the figure, the most effective filter sampling appears to be around 2.5nm. Near this sampling, the SRCM is larger, but

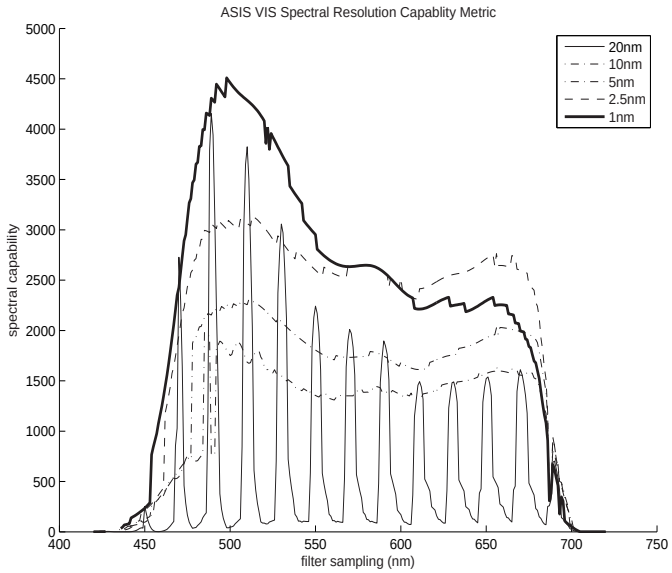

Figure 8.3: Comparison of the ASIS Spectral Resolution Capability in the visible for 1nm, 2nm, 5nm, 10nm, and 20nm filter samplings.

the imaging time is around 30secs. This filter sampling also agrees with the critical filter sampling calculated in section 4.8 for the Gaussian shaped filter transmission.

8.3.2 Sensor Trade-offs. The second use of the SRCM is to compare different sensor trade-offs when designing a new spectral imaging sensor that will process the collected data with the MBSIR algorithm. By modeling different sensor deigns, with different selected parameters, a SRCM can be calculated for each design. A comparison of the different SRCMs can show which design allows for the most improvement with the data is processed when the MBSIR algorithm. The best sensor design given by the SRCM can be balanced with other system requirements to provide the optimum design. By using the SRCM in the design of the sensor, the parameters of the sensor are better optimized to take advantage of the processing available to improve the image resolution.

8.4 Summary

This chapter introduces the Spectral Reconstruction Capability and developed a method for calculating the SRCM, a maximum SRCM and an average SRCM.

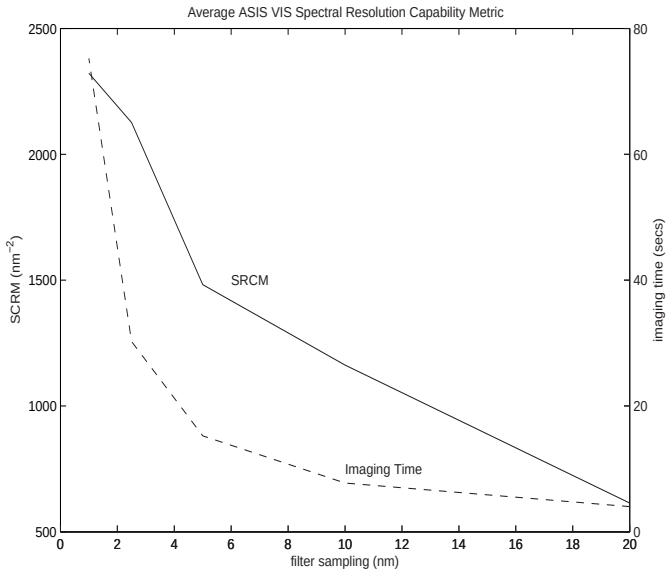

Figure 8.4: The average ASIS visible SRCM for the five different filter samplings and the imaging time required for those five filter samplings. The SRCM metric shows that the higher the filter sampling the better the SRCM, but the longer the imaging time. A 2.5nm to 5nm sampling appears to be an effective balance of resolution and imaging time.

The SRCM is a metric derived from the spectral resolution and spectral capability lower bounds and measures the reconstruction capability of the MBSIR algorithm when the algorithm is used to post-process the data. The SRCM is a useful metric to qualitatively compare both parameter settings when operating a sensor and parameter trade-offs when designing a new sensor.

IX. Model Based Spectral-Polarimetric Image Reconstruction

The MBSIR algorithm can be expanded to take advantage of the polarizations in the LCTFs. Instead of summing the linearly polarized sub-channels to account for all photons as described in section 4.1.4, the separate spectral-polarimetric images are used to estimate the true spectral-polarimetric scene. Spectral-polarimetric imaging provides even more information for satellite characterization, especially for material identification and degradation analysis. The additional polarization information provides new material characterization data that cannot be determined with spectral information alone. Since only the linear polarizations are collected, only the linear polarizations are estimated. However, if the full four Stokes images were collected, the algorithm could be expanded to reconstruct the full polarimetric image.

This chapter develops the model-based spectral-polarimetric image reconstruction algorithm (MBSPIR). The MBSPIR algorithm is very similar to the MBSIR algorithm. The difference between the two is the addition of a fourth polarimetric dimension into the algorithm. The chapter will also discuss how the model of ASIS has to be modified and will provide some simulated results.

9.1 Image Creation

The image created by the spectral-polarimetric imaging sensor can be mathematically described by,

$$i(x,y,\lambda,\pi) = \int \int_{-\infty}^{\infty} \int \int o(u,v,\gamma,\phi) h_1(x-u,y-v,\gamma) h_2(\lambda,\gamma) h_3(\pi,\phi) du dv d\gamma d\phi. \tag{9.1}$$

or in discrete terms,

$$i(x,y,\lambda,\pi) = \sum_{u,v,\gamma} o(u,v,\gamma,\phi) h_1(x-u,y-v,\gamma) h_2(\lambda,\gamma) h_3(\pi,\phi), \tag{9.2}$$

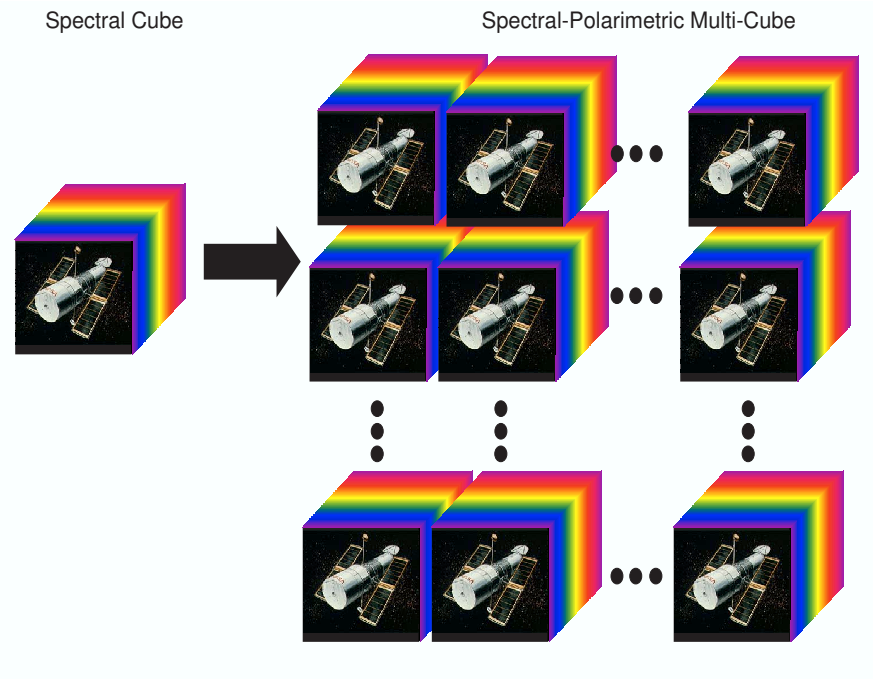

Figure 9.1: Spectral-Polarimetric Multi-Cube

Where $h_3(\pi, \phi)$ is known as the Linear Polarimetric Mixing Function (LPMF). Two polarization terms, (ϕ) and (π) are added to describe the polarization angle in the true spectral-polarimetric scene and the collected spectral-polarimetric image. The spectral-polarimetric image collected is then, $i(x, y, \lambda, \pi)$ which is the super-set of spectral images of the true scene collected in the desired wavelengths. In this case, $i(x, y, \lambda, \pi)$ is referred to as the spectral-polarimetric image multi-cube. As Figure 9.1 shows, the image multi-cube is the collection of spectral image cubes, with one cube for each linear polarization. As with the spectral blurring function in the MBSIR algorithm, the polarimetric blurring will also be treated as variant. The resultant image is the h_1, h_2, and h_3 blurring functions applied to the unblurred, true scene, $o(u, v, \gamma, \phi)$.

The variant spectral and polarimetric blurring is the general case. For the specific invariant spectral and polarimetric blurring, Equations (9.1) and (9.2) are,

$$i(x,y,\lambda,\pi) = \int_{-\infty}^{\infty} \int \int o(u,v,\gamma,\phi)h(x-u,y-v,\lambda-\gamma,\pi-\phi)dudvd\gamma d\phi, \quad (9.3)$$

or in discrete terms,

$$i(x,y,\lambda,\pi) = \sum_{u,v,\gamma,\phi} o(u,v,\gamma,\phi)h(x-u,y-v,\lambda-\gamma,\pi-\phi), \quad (9.4)$$

where the spatial, spectral and polarimetric blurring is described by the impulse response, $h(u,v,\gamma,\phi)$.

9.2 Image Statistics

The statistics of the image formation are identical to those for the MBSID algorithm, given in section 3.2. Therefore the bases of both algorithms is the reduction in Poisson noise.

9.3 Spectral-Polarimetric Image Reconstruction

The ML estimator developed for the spectral-polarimetric reconstruction begins the same as that for the spectral reconstruction, except there is an additional dimension for linear polarization. Again, starting with the Poisson distribution and looking at one specific point $(x_o, y_o, \lambda_o, \pi_o)$, the probability mass function is,

$$P[d(x_o,y_o,\lambda_o,\pi_o) = D(x_o,y_o,\lambda_o,\pi_o)] = \frac{i(x_o,y_o,\lambda_o,\pi_o)^{D(x_o,y_o,\lambda_o,\pi_o)}}{D(x_o,y_o,\lambda_o,\pi_o)!} e^{-i(x_o,y_o,\lambda_o,\pi_o)}. \quad (9.5)$$

where $D(x,y,\lambda,\pi)$ is a particular realization of random variable $d(x,y,\lambda,\pi)$ and $i(x_o,y_o,\lambda_o,\pi_o)$ is the noise free image created from the true scene. For all points

(x, y, λ, π), the probability is,

$$P[d(x_o, y_o, \lambda_o, \pi_o) = D(x_o, y_o, \lambda_o, \pi_o) \,\forall\, (x, y, \lambda, \pi)] = \prod_{x,y,\lambda,\pi} \frac{i(x, y, \lambda, \pi)^{D(x,y,\lambda,\pi)}}{D(x, y, \lambda, \pi)!} e^{-i(x,y,\lambda,\pi)}. \tag{9.6}$$

Repeating the use of the natural log of both sides to remove the exponential, the probability on the left side of Equation (9.6) can be maximized by taking the derivative of Equation (9.6) with respect to the true spectral-polarimetric scene, or truth multi-cube, at a specific point $o(u_o, v_o, \gamma_o, \phi_o)$, setting this equal to zero and solving for this truth multi-cube. So Equation (9.6) becomes,

$$\sum_{x,y,\lambda,\pi} \frac{d(x, y, \lambda, \pi)}{i(x, y, \lambda, \pi)} \frac{d}{do(u_o, v_o, \gamma_o, \phi_o)} i(x, y, \lambda, \pi) - \frac{d}{do(u_o, v_o, \gamma_o, \phi_o)} i(x, y, \lambda, \pi) = 0. \tag{9.7}$$

Since

$$\frac{d}{do(u_o, v_o, \gamma_o), \phi_o} i(x, y, \lambda, \pi) = h_1(x - u_o, y - v_o, \gamma_o) h_2(\lambda, \gamma) h_3(\pi, \phi), \tag{9.8}$$

Equation (9.7) then becomes,

$$\sum_{x,y,\lambda,\pi} [[\frac{d(x, y, \lambda, \pi)}{i(x, y, \lambda, \pi)} - 1] h_1(x - u_o, y - v_o, \gamma_o) h_2(\lambda, \gamma) h_3(\pi, \phi)] = 0. \tag{9.9}$$

Using the same algebraic manipulation as the MBSIR algorithm, the following iteration relation can be developed,

$$o^{new}(u_o, v_o, \gamma_o, \phi_o) = \frac{o^{old}(u_o, v_o, \gamma_o, \phi_o)}{\sum_{x,y,\lambda,\pi} h_1(x - u_o, y - v_o, \gamma_o) h_2(\lambda, \gamma) h_3(\pi, \phi)} \sum_{x,y,\lambda,\pi} \frac{D(x, y, \lambda, \pi)}{i^{old}(x, y, \lambda, \pi)} h_1(x - u_o, y - v_o, \gamma_o) h_2(\lambda, \gamma) h_3(\pi, \phi). \tag{9.10}$$

where,

$$i^{old}(x, y, \lambda, \pi) = \sum_{u,v,\gamma,\phi} o^{old}(u, v, \gamma, \phi) h_1(x - u_o, y - v_o, \gamma_o) h_2(\lambda, \gamma) h_3(\pi, \phi). \tag{9.11}$$

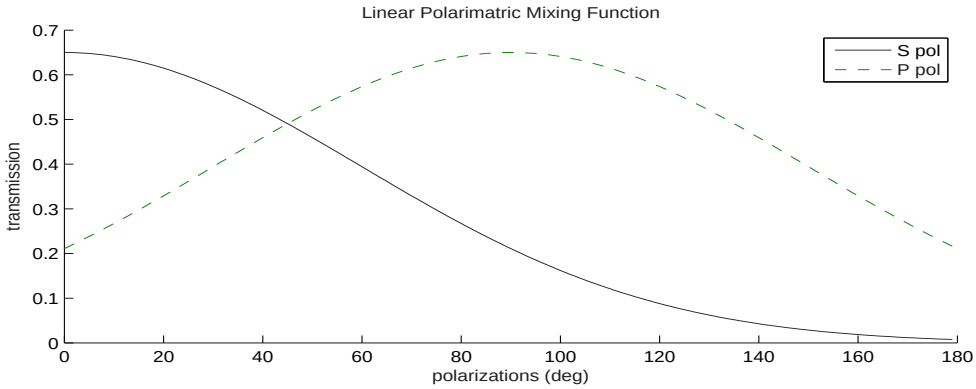

Figure 9.2: Assumed Linear Polarimetric Mixing Function.

9.4 Polarization Effects in ASIS

Unlike the spatial and spectral blurring in ASIS, the polarimetric blurring is not known and has never been accurately measured. Therefore, the LPMF given by h_3 must be assumed and the MBSPIR algorithm cannot be applied to actual ASIS data at this time. Efforts are on-going to measure the changes in polarization induced by ASIS, but these efforts will take some time to complete.

Given an assumed LPMF and the other functions from section 3.3, the ML estimator in Equation (9.10) can now be used to reduce much of the spatial, spectral and linear polarimetric blurring in the data from ASIS. As with the MBSIR, the initial reconstruction guess for Equation (9.10) can be a multi-cube of uniform unit value, and the iterations continue until the stopping criteria is reached.

9.5 ASIS Model for MBSPIR

The MBSPIR algorithm will use the first-order model of ASIS, with the addition of an assumed linear polarimetric mixing function. For simplicity, a broad gaussian will be used as the LPMF, and is shown in Figure 9.2. Figure 9.2 shows the LPMF for two orthogonal linear polarizations (S and P).

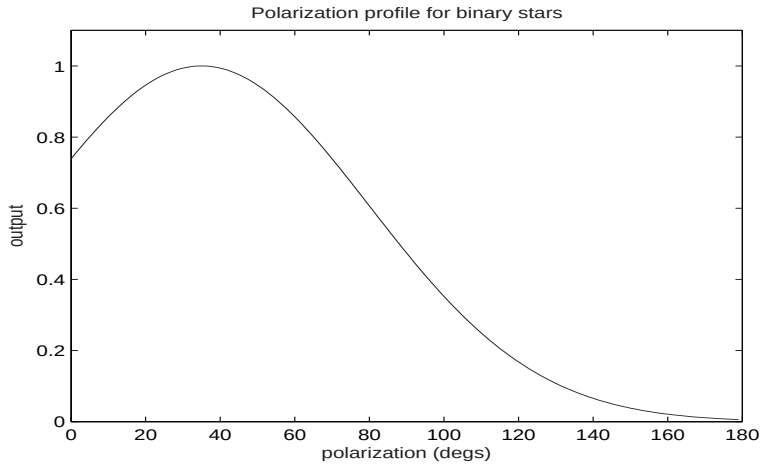

Figure 9.3: Linear polarization profile for the output of both binary stars. The peak output is at 35 degrees of linear polarization.

9.6 Simulation

The simulation in section 5.3.2 can be expanded to include a linear polarimetric reconstruction. To add the linear polarimetric dimension to the simulation, the linear polarization output profile shown in Figure 9.3 is used. This output is used to give the binary stars with a preferred linear polarization angle.

The spectral-polarimetric simulation looked at the binary stars in the visible wavelengths only. However, two different polarization angles were examined. The first angle was the linear polarization angle of greatest output and the second was an additional angle away from the primary. Figures 9.4 and 9.5 give the spatial image and spectral output for the two polarization angles of interest.

9.6.1 Spectral-Polarimetric Data Generation. The first-order ASIS model with the linear-polarimetric mixing was used to generate the spectral-polarimetric image multi-cubes. Figures 9.6 and 9.7 give the images for the S and P orthogonal linear polarizations collected by ASIS.

9.6.2 Spectral-Polarimetric Reconstruction. The MBSPIR algorithm from Equation (9.10) was then applied to the spatially, spectrally and polarimetrically

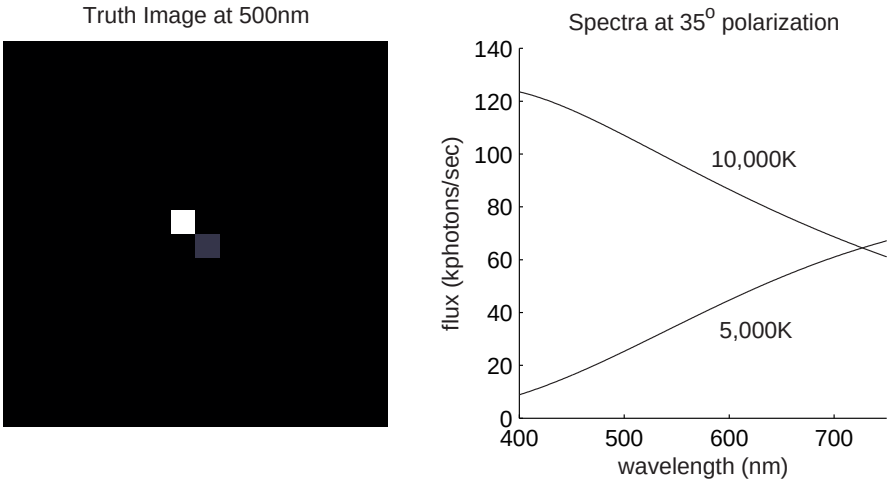

Figure 9.4: Spatial true image and spectral-polarimetric output of a 0.25su radius 10000K and a 5su radius 5000K binary star at 25 light years in the visible at 35 degree linear polarization.

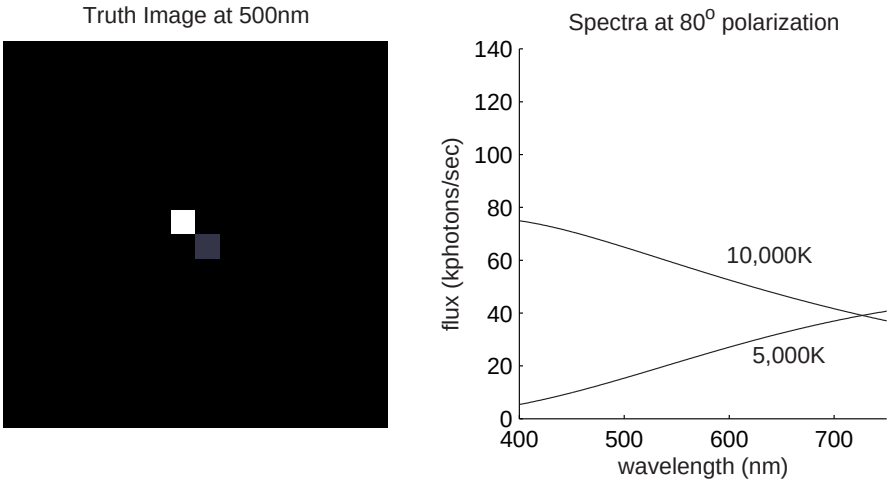

Figure 9.5: Spatial true image and spectral-polarimetric output of a 0.25su radius 10000K and a 5su radius 5000K binary star at 25 light years in the visible at 80 degree linear polarization.

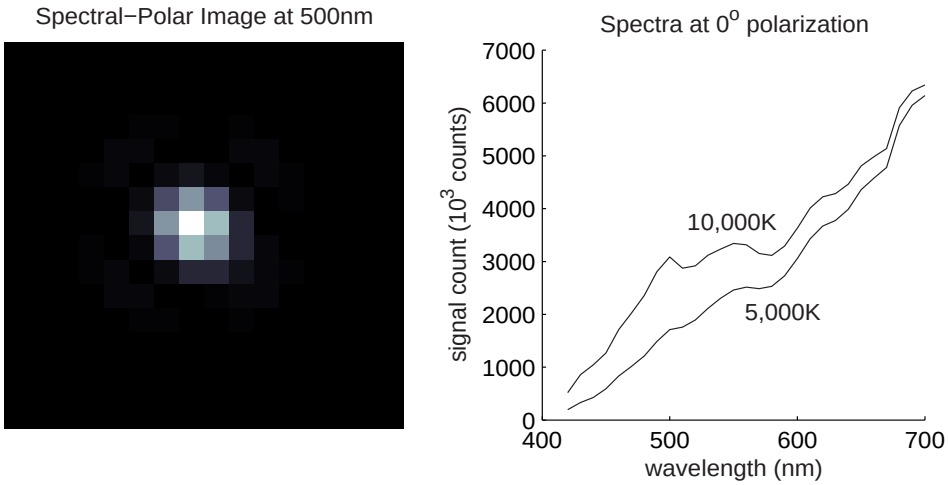

Figure 9.6: Spatial image and spectral-polarimetric output of a 0.25su radius 10000K and a 5su radius 5000K binary star at 25 light years with a preferred linear polarization of 35 degrees in the visible at 0 degree linear polarization of the S channel of ASIS.

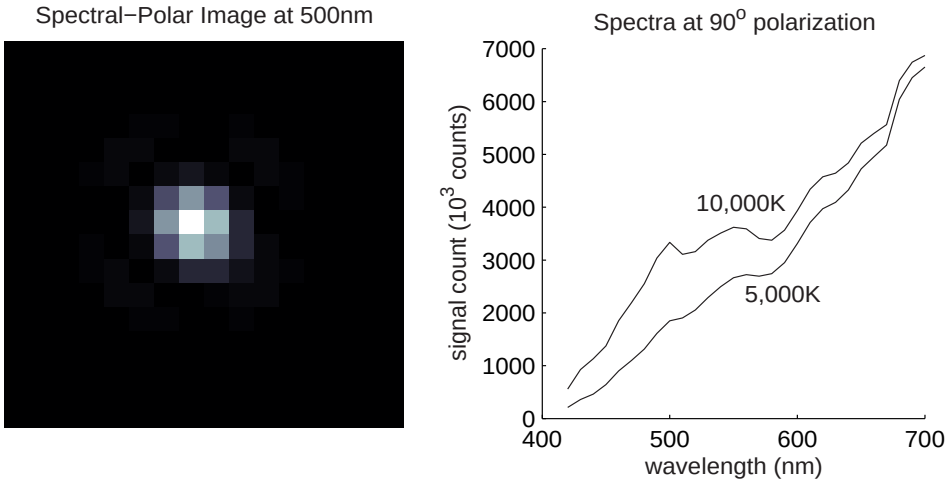

Figure 9.7: Spatial image and spectral-polarimetric output of a 0.25su radius 10000K and a 5su radius 5000K binary star at 25 light years with a preferred linear polarization of 35 degrees in the visible at 90 degree linear polarization of the P channel of ASIS.

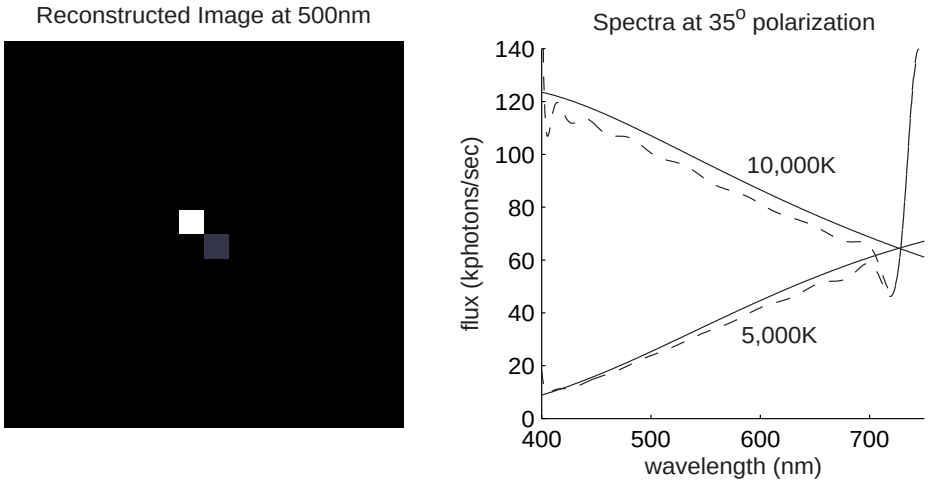

Figure 9.8: Spatial image reconstruction and spectral-polarimetric output of a 0.25su radius 10000K and a 5su radius 5000K binary star at 25 light years in the visible at 35 degree linear polarization. The solid line is the true spectral data and the dashed line a linear interpolation of the reconstruction.

blurred images shown in Figures 9.6 and 9.7. The reconstruction was started with an initial guess of unity for the entire spectral-polarimetric image multi-cube. The results of the MBSPID algorithm are shown in Figures 9.8 and 9.9.

Another way to look at how well the spectral-polarimetric reconstruction worked is to look in the linear polarimetric dimension only. Figure 9.10 shows the true and reconstructed polarimetric spectra of the binary stars at 500nm.

9.6.3 Results. As Figure 9.11 shows, the average percent difference between the reconstruction and the truth data for the visible polarization spectra is 5%. Therefore, the reconstruction is not only able to undo much of the spectral and spatial blurring, but also the induced linear polarimetric blurring assumed for ASIS.

9.7 Summary

In this chapter the MBSIR algorithm was expanded to include an estimation for linear polarization. The MBSPIR algorithm uses the orthogonal sub-channels required when using the LCTFs to collect polarized sources to provide the necessary spectral-polarimetric data for the reconstruction. The MBSPIR algorithm is very

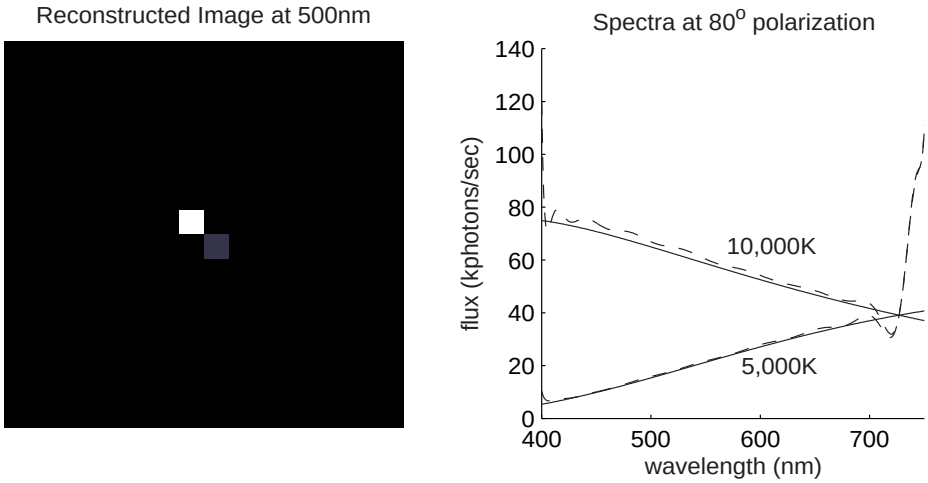

Figure 9.9: Spatial image reconstruction and spectral-polarimetric output of a 0.25su radius 10000K and a 5su radius 5000K binary star at 25 light years in the visible at 80 degree linear polarization. The solid line is the true spectral data and the dashed line a linear interpolation of the reconstruction.

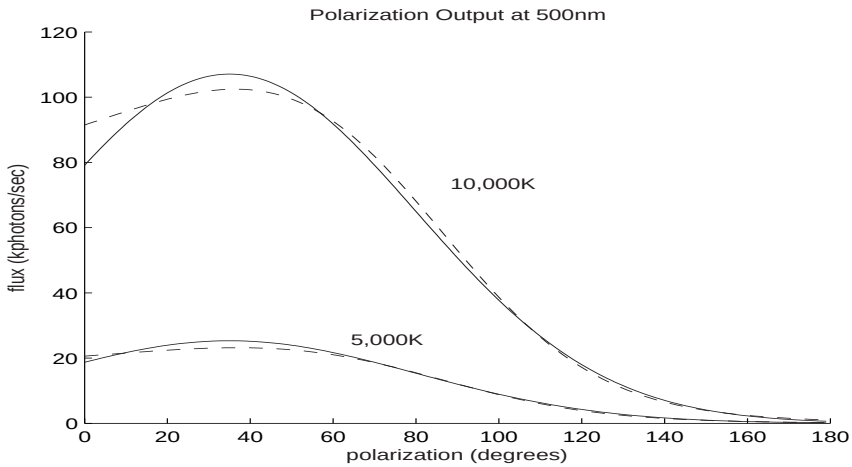

Figure 9.10: Polarimetric output of a 0.25su radius 10000K and a 5su radius 5000K binary star at 25 light years with a preferred linear polarization of 15 degrees in the visible at 500nm. The solid line is the true polarimetric data and the dashed line the reconstruction.

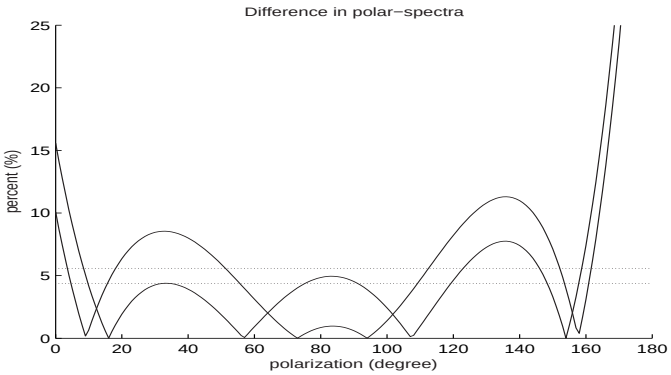

Figure 9.11: Percent difference between the truth and reconstructed linear polarimetric spectra of the binary star. The lines are the average of the difference.

similar to the MBSIR algorithm, except the MBSPIR algorithm includes a LPMF to model the polarimetric blurring within the sensor. Since the LPMF for the complex optics of ASIS has not been measured, an assumed LPMF was used for simulating the reconstruction of a spectral-polarimetric binary star image. The simulation shows that the MBSPIR algorithm can reduce the blurring in the simulated data, including the spatial, spectral and linear polarimetric structure.

X. Summary

This research developed the first spectral image reconstruction algorithm which simultaneously improves the spatial and spectral resolution of spectral images collected with ETFs. The algorithm, known as the Model-based Spectral Image Reconstruction algorithm, is based on statistical estimation and requires no knowledge of the imaged scene. The algorithm uses a model of the imaging sensor to iteratively reduce the spectral and spatial blurring that occurs within the sensor. The quality of the reconstruction depends directly on the accuracy and quality of the model developed for the sensor.

For this research, the algorithm was developed for the AEOS Spectral Imaging Sensor, and new spectral imaging sensor installed at the MSSC. ASIS is used to take atmospherically compensated spectral images of satellites, to enhance the understanding of the satellite's performance and capabilities. The sensor will provide valuable information to advance the knowledge to achieve a more robust Space Situational Awareness.

10.1 Results

The algorithm developed in this research was expected to expand on the deconvolution method developed for gamma-ray spectroscopy. The deconvolution algorithm used for the gamma-ray spectroscopy was able to double the spectral resolution of the collected spectra [35]. As Figures 10.1 and 10.2 show, the MBSIR algorithm is also able to double the spectral resolution. However, the MBSIR algorithm has simultaneously resolved two spatial features. The spectral features in the 20nm filter sampling were resolvable without the MBSIR algorithm. The algorithm was required to resolve the features in the 10nm filter sampling.

The MBSIR algorithm was also used to reconstruct a continuous spectra to show the improvement of the MBSIR algorithm over other spectral reconstruction methods, such as PE. In the PE method, a 20nm filter sampling was used and the PE method reconstructed the continuous spectra of three color samples to a RMS

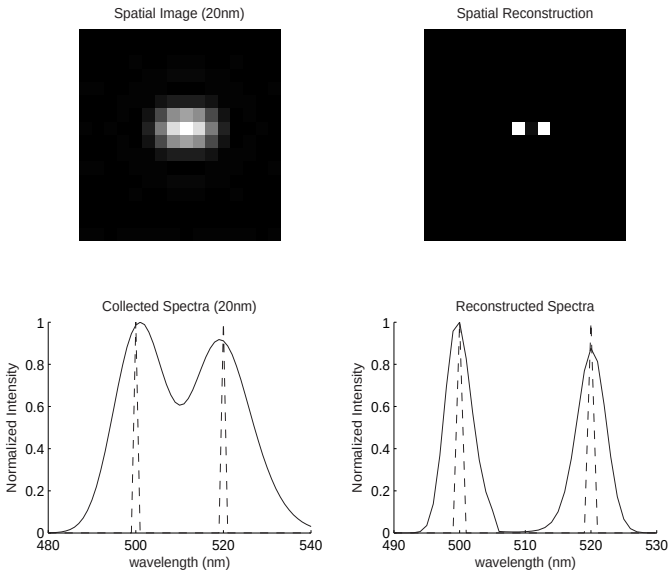

Figure 10.1: The simultaneously improved spatial and spectral resolution for a 20nm filter sampling. The two spatial features are resolved in the reconstruction. The two spectral features are resolved in both the simulated data and in the reconstruction. The solid lines are the simulated spectra and the reconstruction as labeled. The dashed lines are the spectral features.

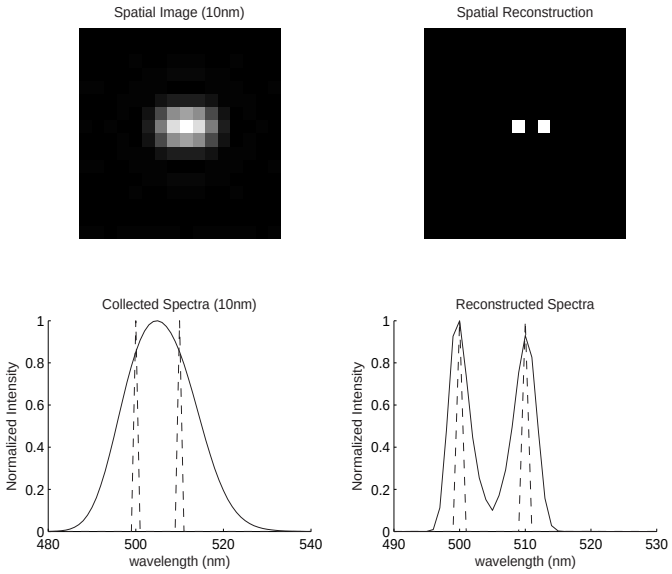

Figure 10.2: The simultaneously improved spatial and spectral resolution for a 10nm filter sampling. The two spatial features are resolved in the reconstruction. The two spectral features are resolvable in the reconstruction only. The solid lines are the simulated spectra and the reconstruction as labeled. The dashed lines are the spectral features.

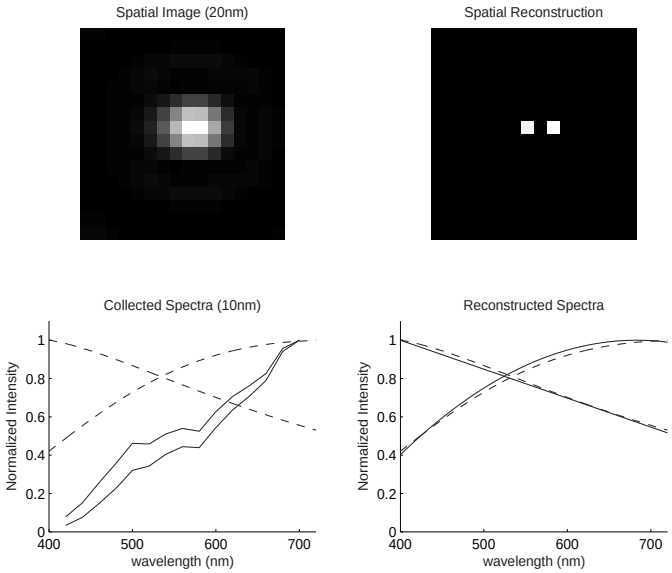

Figure 10.3: The simultaneously improved spatial and spectral resolution for a 20nm filter sampling. The two spatial features are resolved in the reconstruction. The two continuous spectra are reconstructed to a 0.103 RMS error. The solid lines are the simulated spectra and the reconstruction as labeled. The dashed lines are the continuous spectral input.

error of 0.243 [24]. For comparison, the MBSIR algorithm was used to reconstruct the continuous blackbody spectra of a binary star. Figure 10.3 shows the results of the binary star reconstruction. The mean RMS error for the reconstructions is 0.103, which is approximately half the RMS error for a similar reconstruction using the PE method. Additionally, the RMS error is reduced without the need for any *a priori* knowledge of the imaged scene required by the PE method. The MBSIR algorithm also reconstructs the spatial scene which is not included in the PE method.

After the derivation of the MBSIR algorithm, several simulations were shown in Chapter V to demonstrate the expected benefit of the algorithm for the data collected in Chapter VI. In the simulations, the algorithm showed how it can be used to resolve both spatial and spectral features of a spectral source, where the features were not resolvable when the data was collected. The algorithm was also used to simulate the reconstruction of the spectra of a singlet star and the spatial scene and spectra of a

binary star. For both of the singlet and binary star simulations, the algorithm was able to reconstruct the spectra of the stars.

While some data has been collected with ASIS, much of the data is not suitable for MBSIR processing because of the incomplete collection or coarse filter sampling. To demonstrate the use of the algorithm on data a second sensor was constructed. The AFIT Spectral Imaging Reconstruction Test Bench is much less complex that ASIS, but is very similar to ASIS from a modeling perspective. Two data sets were collected with ASIR-TB that show how the algorithm improves the resolution on data from a spectral imaging sensor. Hg(Ar) and Ne spectral calibration sources were collected in the visible and near-IR with a intentional defocus and coarse filer sampling that served to blur the spatial and spectral features in the data so the features were unresolvable. When the MBSIR algorithm was applied to the data, the same features were resolvable. The criteria used to resolve the features was the Rayleigh criteria for the spatial features and a Rayleigh like criteria for the spectral features. Figures 6.3 and 6.8 most clearly show the spatial and spectral resolution enhancement the MBSIR algorithm can provide.

After showing the algorithm can be used successfully on data collected with a spectral imaging sensor, the CRLBs were determined for two important reconstruction parameters. The lower bounds for the spectral resolution and spectral accuracy were calculated for both the ASIR-TB and ASIS sensors. These two lower bounds measure the best possible resolution and accuracy that the processing algorithm can achieve when used to process data from ASIR-TB or ASIS. The spectral resolution lower bound for the algorithm determines the minimum separation between two spectral features that the algorithm can resolve, while the spectral accuracy bound measures the capability of the algorithm to place a spectral feature at the correct wavelength.

The lower bounds can be combined together to give a spectral reconstruction performance metric known as the Spectral Reconstruction Capability Metric. The SRCM can be used to determine the optimal operational parameters for the sensor.

The SRCM can show the most efficient filter sampling, helping balance resolution enhancement and imaging time. For the ASIS visible channel, this was determined to be 2.5nm. Additionally, the SRCM can be used to perform design parameter trade-offs for new imaging systems. By looking at the SRCM, the sensor can be designed to make the optimum use of the resolution enhancement that the MBSIR algorithm can provide.

The filters used for ASIS allow for the collection of a spectral-polarimetric image. Since the orthogonal linear polarizations for every spectral image is collected, it is possible to perform a complete spectral-polarimetric reconstruction. The MBSIR algorithm can be expanded into the polarimetric dimension to have a Model-based Spectral-Polarimetric algorithm. However, in order to perform a spectral-polarimetric reconstruction, the blurring introduced to the polarization with the sensor needs to be understood and modeled. Currently, this is not known for ASIS. However, using an assumed polarimetric function, a simulation is shown to demonstrate the potential improvement achievable using the MBSPIR algorithm.

Finally, while this research has developed a method for improving the resolution of images collected with ASIS, more algorithm enhancements can be examined. Using a priori knowledge could improve the results of the algorithm. Also, the algorithm can be used to show how more unorthodox sensor designs can provide better performance when the images are first post-processed with an reconstruction algorithm.

10.2 Further Research

While this research has laid a good foundation for enhancing the resolution of images collected with the AEOS Spectral Imaging Sensor, many more areas are open to investigation. This chapter will recommend two topics that should be researched further.

10.2.1 Algorithm Enhancement. The use of general a priori knowledge has been successfully used to improve the quality of images reconstructed with maximum

likelihood estimators [13,33]. Examples of the a priori knowledge used to improve the image quality include support, knowing where the images is located within the image plane, and positivity, enforcing that the signal of the image remain positive. These, and similar a priori ideas, can be used with the MBSIR algorithm to potentially improve the quality of the reconstruction.

The research topic would be to determine what a priori knowledge would improve the MBSIR algorithm and quantify the improvement by examining the lower bounds. Simulations could then be used to show the benefit of the a priori knowledge. The revised algorithm could then be applied to currently and newly collected data from ASIS or ASIR-TB.

10.2.2 Realistic CRLBs. As mentioned in the introduction to Chapter VII, the CRLBs calculated in this research are the ultimate lower bounds. For these CRLBs, the lower bound to calculated at on two wavelengths for the spectral resolution and only one wavelength for the spectral accuracy. This leads to a lower bound that shows better performance than will be achievable.

This research topic will re-calculate the lower bounds to determine the realistic CRLBs for the spectral resolution and spectral accuracy. The realistic bounds can be determined by calculating the bound when estimating all wavelengths simultaneously.

10.2.3 Lower bound on Spectral Amplitude. As seen in section 6.2.1.2, the location and amplitude ratios for the reconstructed spectral features were not reconstructed as accurately as desired. While section 7.3 investigated a CRLB for spectral accuracy, there was no CRLB determined for the spectral amplitudes.

This research topic would investigate a CRLB for the spectral amplitude. The initial CRLB for spectral amplitude was actually derived as part of the CRLB for spectral accuracy. Instead of looking at the (1,1) entry of the inverted Fisher information matrix, the (2,2) entry would be examined. However, a more comprehensive CRLB for the spectral amplitude could be developed and investigated.

10.2.4 New Sensor Concepts. Most spectral imaging sensors, including ASIS, was originally designed to need little to no post-processing to interpret the spectral images. With small, non-overlapping bandwidths the data from these sensors need only to be spatially aligned and calibrated. While this makes using the data simple, it provides for no inherent capability to use image post-processing to improve the resolution of the image. To use the MBSIR algorithm to post-process the data, the sensor needs to be used in a way that it would not normally be operated; the images are collected with significantly overlapping bandwidths.

By knowing that the images will be post-processed to increase the image resolution, a sensor can be more optimally designed to take advantage of the processing. The first, and most simple way, this can be done is to increase the bandwidth of the filters. Instead of a 20nm bandwidth in the visible, a 40nm bandwidth could be used. The larger bandwidth should allow for fewer images to be collected, decreasing the overall time required to collect an image, while maintaining a good spectral reconstruction capability. However, the larger bandpasses will not perform as well as the smaller bandpasses. Since the collected images are of such a large bandwidth, they may or may not be useful with applying the MBSIR processing.

An even more unorthodox approach is to have a multiple bandpass filter. Instead of transmitting one 20nm bandwidth region, two, or even three, 10nm bandpass regions would be transmitted. Figure 10.4 shows a notional bandpass for this filter design. The multiple bandpass regions are created by increasing the phase retardance with in the Lyot cell. In this design, fewer images would need to be collected since multiple bands are collected per image, leading to a decreased imaging time. The bandpass of each region would remain a 20nm, so would not suffer the decreased spectral resolution due to the large bandwidths. However, because each image contains photons from multiple bandpasses, the spectral image would be essentially unusable with post-processing with MBSIR. An additional complicating factor is that the location of the second bandpass and the bandwidth are variant; the distance between

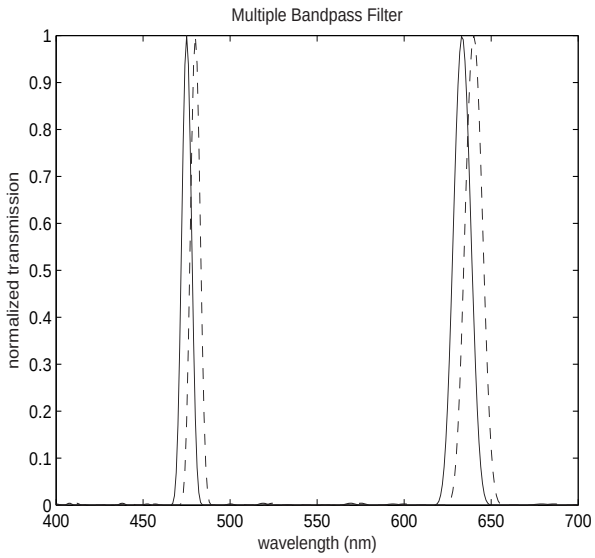

Figure 10.4: An notional filter transmission profile with a multiple bandpass. The second bandpass is created by increasing the phase retardance of the Lyot cell. The solid and dashed lines show two successive filter selections.

the two bandpasses and the bandwidth of the second bandpass changes as the center wavelengths are selected.

This research topic would examine how to best implement the large bandwidth and multiple bandpass filters. To quantify the impact to the improvement of the image, the lower bounds would be calculated. Each of the new sensor designs could be simulated to show the expected performance. While neither sensor design exists, existing data could be used to provide a first-order example of the new algorithm working for the multiple bandpass filter. For the multiple bandpass filter, the sensor sampling also needs to be investigated because of the location and bandwidth invariance.

Bibliography

1. "Report of the Commission to assess United States National Security Space Management and Organization". http://www.defenselink.mil/pubs/space20010111.html, 2001.
2. "Lu-100 Specification Sheet". http://www.lumenera.com/industrial/lu105.php, 2006.
3. *The Newport Resource 2006/2007*. Newport, 2006.
4. AFSPC. "Air Force Space Command Strategic Master Plan FY06 and Beyond". http://www.peterson.af.mil/hqafspc/library/AFSPCPAOffice/Finaligned!v1.1.pdf, 2003.
5. Andersen, Brian K. "Space Surveillance: Cornerstone of the DoD Strategy for Space Control". *2001 AMOS Technical Conference*, 46–53, 2001.
6. Andor. "Andor Specification Sheet for iXon DV887". http://www.andor-tech.com/.
7. Ball, David W. *The Basics of Spectroscopy*. SPIE, Bellingham, WA, 2001.
8. Billings, Paul A., Michael F. Reiley, and Bruce E. Stribling. "Mitigating Turbulence-Induced Image Blur Using Multiframe Blind Deconvolution". *2001 AMOS Technical Conference*, 506–512, 2001.
9. Boeing. "AEOS Adaptive Optics: AEOS Adaptive Optics Performance Report". AFRL/DEBI, 2004.
10. Briscoe, David. "AEOS Radiometer Subsystem (ARS) operations and data products on the AEOS 3.67-meter telescope on Maui". *2001 AMOS Technical Conference*, 147–156, 2001.
11. Brodzik, Andrzej K. and Jonathan M. Mooney. "Convex Projections Algorithm for Restoration of Limited-Angle Chromotomographic Iimages". *J. Opt. Soc. Am. A*, 16(2):246–257, 1999.
12. Cain, Stephen C. "Bayesian-Based Subpixel Brightness Temperature Estimation From Multichannel infrared GOES Radiometer Data". *IEEE Transactions on Geoscience and Remote Sensing*, 42(1):188–201, 2004.
13. Calef, Brandoch. "Quantifying the Benefits of Positivity". *2005 AMOS Technical Conference*, 44–51, 2005.
14. Christou, Julian C., Robert Fugate, Robert Johnson, and Rick Cleis. "Deconvolution of Columbia Images from the Starfire Optical Range". *2003 AMOS Technical Conference*, 2003.

15. Dereniak, E. L. and G. D. Boreman. *Infrared Detectors and Systems*. John Wiley & Sons, Inc., New York, NY, 1996.

16. Descour, Michael and Eustace Dereniak. "Computer-tomography Imaging Spectrometer: Experimental Calibration and Reconstruction Results". *Appl. Opt.*, 34(22):4817–4826, 1995.

17. Dong, Ying, Zheng You, Peng Gao, and Yuncai Hao. "Miniature imaging spectrometer based on an acousto-optic tunable filter (AOTF)". *Proc. SPIE Int. Soc. Opt. Eng.*, 4897(1):138–146, 2003.

18. Gat, Nahum. "Imaging spectroscopy using tunable filters: a review". *Proc. SPIE Int. Soc. Opt. Eng.*, 4056(1):50–64, 2000.

19. Goodman, Joseph W. *Introduction to Fourier Optics*. McGraw-Hill Companies, Inc., Boston, MA, 1968.

20. Goodman, Joseph W. *Statiscal Optics*. John Wiley & Sons, Inc., New York, NY, 1985.

21. Gould, Malcolm and Stephen Cain. "Development of a fast chromotomographic spectrometer". *Opt. Eng.*, 44(11):110503–3, 2005.

22. Hall, Doyle, John Africano, Kris Hamada, Paul Kervin, Karl Kremeyer, John Lambert, Jennifer Okada, Lewis C. Roberts Jr., and Paul Sydney. "AEOS I-Band Photometry of Moving Targets". *2003 AMOS Technical Conference*, 2003.

23. Hamada, Kris, Paul Sydney, John Africano, Vicki SooHoo, Kira Jorgensen amd Gene Stansbery, Daron Nishimoto, and Paul Kervin. "Space Object Identification (SOI) with the Spica spectrometer at the AFRL Maui Optical and Supercomputing (AMOS) site". *2002 AMOS Technical Conference*, 2002.

24. Hardeberg, Jon Y., Francis Schmitt, and Hans Brettel. "Multispectral color image capture using a liquid crystal tunable filter". *Opt. Eng.*, 41(10):2532–2548, 2002.

25. Hecht, Eugene. *Optics*. Addison Wesley, San Fransisco, CA, 2002.

26. Jerkatis, Kenneth J. "AEOS Spectral Imaging Sensor Design Documents".

27. Jorgensen, Kira, John L. Africano, Eugene G. Stansbery, Paul W. Kervin, Kris M. Hamada, and Paul F. Sydney. "Determining the material type of man-made orbiting objects using low-resolution reflectance spectroscopy". *Proc. SPIE Int. Soc. Opt. Eng.*, 4490(1):237–244, 2001.

28. Jorgensen, Kira M. "Using Refelectance Spectroscopy to Determine Material Type of Orbital Debris". Dissertation, University of Colorado, 2000.

29. Kaler, James B. "Stars". 2006. URL `http://www.astro.uiuc.edu/ kaler/sow/sowlist.html`.

30. Lomheim, Terrence S. "Multispectral and Hyperspectral Image Sensors, SPIE Short course SC194 notes". SPIE.

31. Lule, S., T.and Benthien, H. Keller, F. Mutze, P. Rieve, K. Seibel, M. Sommer, and M Bohm. "Sensitivity of CMOS based imagers and scaling perspectives". *IEEE Transactions on Electronic Devices*, 47(11):2110–2122, Nov 2000.

32. Luu, K. Kim, Charles L. Matson, Joshua Snodgrass, S. Maile Griffin, Kris Hamada, and John V. Lambert. "Object characterization from spectral data". *2003 AMOS Technical Conference*, 2003.

33. Matson, Charles L. "Spatial Frequency Effects of Support Constraints on Deconvolved Data". *2004 AMOS Technnical Conference*, 138–144, 2004.

34. Matson, Charles L. and Kathy J. Schultze. "Blind Material Identification from Spectral Traces". *2004 AMOS Technical Conference*, 570–580, 2004.

35. Meng, Ling-Jian and David Ramsden. "An Inter-comparison of Three Spectral-Deconvolution Algorithms for Gamma-Ray Spectroscopy". *IEEE Trans. on Nuc. Sci.*, 47(4):1329–1336, Aug 2000.

36. Miller, Peter J. and Clifford C. Hoyt. "Multispectral imaging with a liquid crystal tunable filter". *Proc. SPIE Int. Soc. Opt. Eng.*, 2345(1):354–365, 1995.

37. Miyazawa, Kanae, Kazuhiko Kurashiki, Markku Hauta-Kasari, and Satoru Toyooka. "Broadband color filters with arbitrary spectral transmittance using a liquid crystal tunable filter (LCTF)". *Proc. SPIE Int. Soc. Opt. Eng.*, 4421(1):753–756, 2002.

38. Mooney, Jonathan M., Virgil E. Vickers, Myoung An, and Andrezj K. Brodzik. "High-Throughput Hyperspectral Infrared Camrea". *J. Opt. Soc. Am. A*, 14(11):2951–2961, 1997.

39. Neyman, Christopher R., Gene C. Hughes Jr., and Lewis C. Roberts Jr. "AEOS Adaptive Optics System: One Year of Operations". *2001 AMOS Technical Conference*, 247–255, 2001.

40. Payne, Tamara E., Stephen A. Gregory, Nina M. Houtkooper, and Todd W. Burdullis. "Classification of geosynchronous satellites using color photometric techniques". *2002 AMOS Technical Conference*, 2002.

41. Payne, Tamara E., Stephen A. Gregory, Darryl J. Sanchez, Todd W. Burdullis, and Susan L. Storm. "Color photometry of geosynchronous satellites using the SILC filters". *Proc. SPIE Int. Soc. Opt. Eng.*, 4490(1):194–199, 2001.

42. Richardson, B. H. "Bayesian-based Iterative Method of Image Restoration". *J. Opt. Soc. Am.*, 62:55–59, 1972.

43. Sansonetti, Jean E. and W. C. Martin. "Handbook of Basic Atomic Spectroscopic Data". http://physics.nist.gov/PhysRefData/Handbook/, August 2005.

44. Schowengerdt, Robert A. *Remote Sensing: Models and Methods for Image Processing*. Acedemic Press, San Deigo, CA, 1997.

45. Schulz, Timothy, Bruce Stribling, and Jason Miller. "Multiframe Blind Deconvolution with Real Data: Imagery of the Hubble Space Telescope". *Opt. Express*, 1:355–362, 1997.

46. Schulz, Timothy J. "Multiframe blind deconvolution of astronomical images". *J. Opt. Soc. Am. A*, 10:1064–1073, 1993.

47. Shepp, Lawrence and Yehuda Vardi. "Maximum Likelihood Reconstruction for Emission Tomography". *IEEE Trans. on Med. Im.*, MI-1(2):113–122, 1982.

48. Sridharan, R. and Antonio F. Pensa. "U. S. Space Surveillance Network Capabilities". *Proc. SPIE Int. Soc. Opt. Eng.*, 3434:88–100, 1998.

49. Trees, Harry L. Van. *Detection, Estimation, and Modulation Theory*, volume 1. John Wiley and Sons, 1968.

Index

The index is conceptual and does not designate every occurrence of a keyword. Page numbers in bold represent concept definition or introduction.

REPORT DOCUMENTATION PAGE

Form Approved
OMB No. 0704–0188

1. REPORT DATE *(DD–MM–YYYY)*	2. REPORT TYPE	3. DATES COVERED *(From — To)*
21–12–2006	Doctoral Dissertation	Sept 2003 — Aug 2006

4. TITLE AND SUBTITLE

Reconstructing Spectral Scenes Using Statistical Estimation to Enhance Space Situational Awareness

5a. CONTRACT NUMBER

5b. GRANT NUMBER

5c. PROGRAM ELEMENT NUMBER

6. AUTHOR(S)

Blake, Travis F., Maj, USAF

5d. PROJECT NUMBER

ENG06-167

5e. TASK NUMBER

5f. WORK UNIT NUMBER

7. PERFORMING ORGANIZATION NAME(S) AND ADDRESS(ES)

Air Force Institute of Technology
Graduate School of Engineering and Management (AFIT/EN)
2950 Hobson Way
WPAFB OH 45433-7765

8. PERFORMING ORGANIZATION REPORT NUMBER

AFIT/DS/ENG/06-05

9. SPONSORING / MONITORING AGENCY NAME(S) AND ADDRESS(ES)

Dr. Victor Gamiz
Air Force Research Laboratory, Directed Energy Directorate
3550 Aberdeen Ave. S.E.
Kirtland Air Force Base, NM 87117
(505) 846-4846
victor.gamiz@kirtland.af.mil

10. SPONSOR/MONITOR'S ACRONYM(S)

11. SPONSOR/MONITOR'S REPORT NUMBER(S)

12. DISTRIBUTION / AVAILABILITY STATEMENT

Approved for public release; distribution unlimited

13. SUPPLEMENTARY NOTES

14. ABSTRACT

A new sensor, the Advanced Electro-Optical System (AEOS) Spectral Imaging Sensor (ASIS) has been developed at the Maui Space Surveillance Complex (MSSC). ASIS is capable of collecting resolved imagery of space objects in 10's-100's of spectral bands while using an adaptive optics system. However, the stringent requirements of collecting ground-based images requires a sensor that induced spectral blurring. Post-processing algorithms to remove this blurring are required to fully exploit these spectral images. This research focuses on developing the reconstruction algorithms, based on proven estimation theories, required to spectrally deblur the images collected from ASIS. Additionally, the research will expand the algorithm to also estimate the linear polarizations of the scene. The Cramér-Rao lower bounds on two key performance parameters, the spectral resolution and accuracy, of the reconstruction algorithm will also be calculated. Through the examination of these lower bounds a performance metric can be determined. This metric can be used to compare the ability of the algorithm to work on different spectral sensors.

15. SUBJECT TERMS

model-based spectral image reconstruction deconvolution, MBSIR, spectral image reconstruction, , ASIS, multi-spectral, hyper-spectral, spectral resolution

16. SECURITY CLASSIFICATION OF:			17. LIMITATION OF ABSTRACT	18. NUMBER OF PAGES	19a. NAME OF RESPONSIBLE PERSON
a. REPORT	b. ABSTRACT	c. THIS PAGE			Matthew E. Goda, Lt Col, USAF (ENG)
U	U	U	UU	176	19b. TELEPHONE NUMBER *(include area code)* (937) 255–3636, ext 4614